Temporal studies of GRB light curves and neutrino flux prediction for multi-collision zone model

Candidate

Angela Zegarelli
ID number 1529762

Thesis Advisor	Co-Advisor
Prof. Antonio Capone	Silvia Celli

Thesis not yet defended

Contents

Chapter 1

Cosmic Rays

1.1 Introduction

In 1911 and 1912 Austrian physicist Victor Hess made a series of ascents in a hydrogen balloon to take measurements of radiation in the atmosphere. He was looking for the source of *ionizing radiation*[1] that registered on an electroscope. Initially the prevailing theory was that the radiation came from the rocks of the Earth.

In 1911 his balloon reached an altitude of around 1100 m, but Hess found no essential change in the amount of radiation compared with ground level. Then, on 7 August 1912, in the last of seven flights that year, Hess made an ascent to 5300 m and found an increase of the ionization rate if compared to the sea level. His result was later confirmed by German physicist Werner Kolhörster; he took balloon measurements up to a height of 9300 m founding again an increase of the ionization up to ten times that at sea level (Figure 1.1). The intensity of the radiation, at a fixed altitude, was relatively constant, with no day-night or weather dependent variations. This was the evidence that the source for these ionizing rays came from above the Earth's atmosphere and it was therefore confirmed unambiguously that an unknown radiation with an extreme penetrating power was causing ionization.

Hess had therefore discovered a natural source of high-energy particles coming from the outer space: *Cosmic Rays* (CRs) [74]. He shared the 1936 Nobel prize in physics for his important discovery, and cosmic rays became a useful tool in physics experiments.

1.2 Energy Spectrum

The Earth's atmosphere is continually crossed by cosmic rays (*primary CRs*), uniformly and isotropically, that interacting with the atmosphere nuclei originate the so-called *secondary CRs*. The energetic particles that arise from this process collide in turn with other nuclei producing a "cascade of particles", which is called *Extensive Air Shower* (EAS) [26], as shown in Figure 1.2. Through several experiments one can study these showers and draw conclusions on CR characteristics. However, one

---

[1]Radiation that carries enough energy to liberate electrons from atoms or molecules, thereby ionizing them.
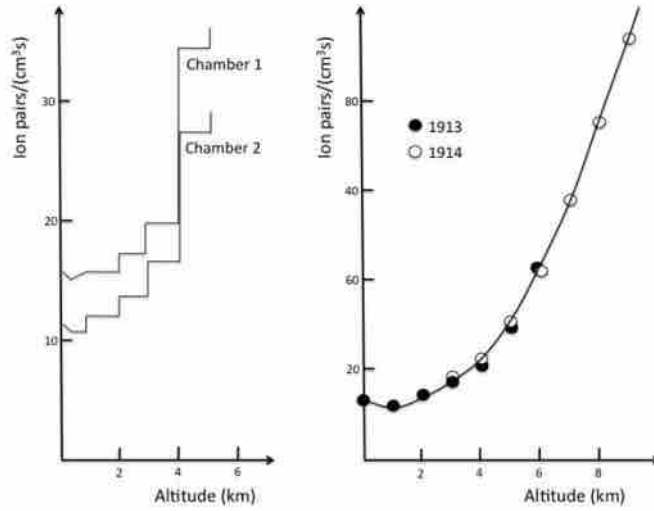
Figure 1.1. Variation of ionization with altitude. Left panel: Final ascent by Hess (1912), carrying two ion chambers [74]. Right panel: Ascents by Kolhörster (1913, 1914) [82].
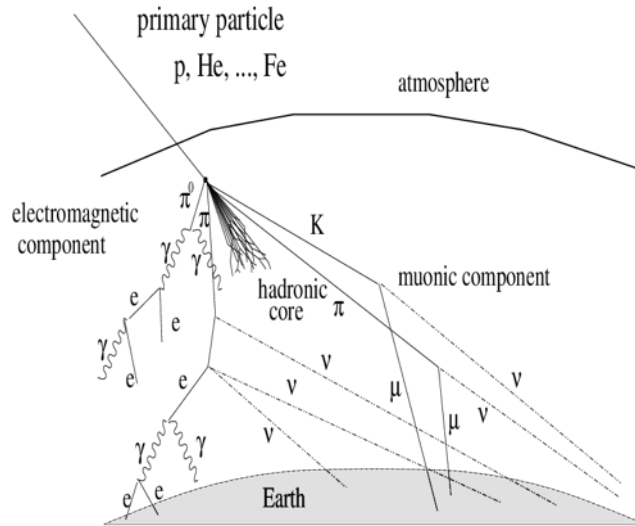
Figure 1.2. Schematic view of an air shower with separated hadronic, muonic and electromagnetic component (from [119]).

have to take into account the rate at which the particles arrive, depending on their energy.

The flux of cosmic particles is steeply falling with increasing energy, in fact the differential cosmic rays spectrum[2] is well described by a power law distribution over a wide energy range, from few hundreds MeV up to about a hundred EeV [58] (Figures 1.3 and 1.4):

$$\frac{dN}{dE} \propto E^{-\gamma}. \tag{1.1}$$

There are four regions in the spectrum, each characterized by a specific value of

---

[2]Number of particles per unit time and unit solid angle incident on a unit area surface orthogonal to the direction of observation.
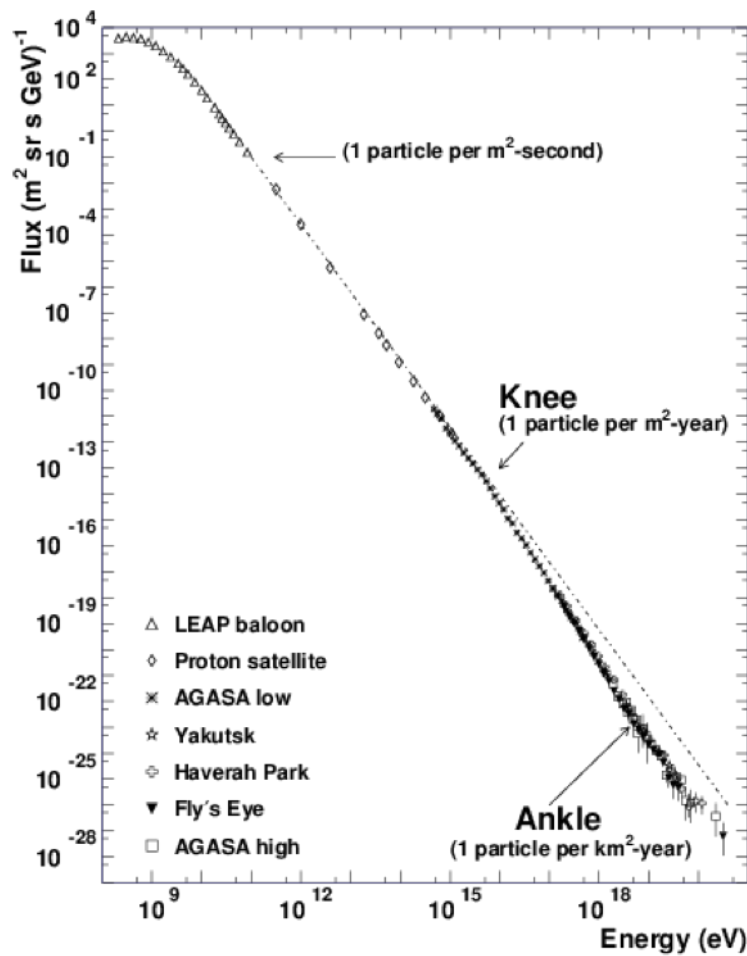
Figure 1.3. All-particle spectrum of cosmic rays, with it's two features, the knee and the ankle.

the *spectral index* γ and connected at three points: the *knee* at $\approx 3 \cdot 10^6$ GeV, the *second knee* at $\approx 3 \cdot 10^8$ GeV and finally the *ankle* at $\approx 5 \cdot 10^8$ GeV. Below the knee $\gamma \approx 2.7$, steepening to $\gamma \approx 3.1$ and then $\gamma \approx 3.3$ until the spectrum flattens at the ankle, above wich $\gamma \approx 2.6$ (Figure 1.4).

The trend of the CRs spectrum can be explained by assuming that the CRs reach these energies through the so called "first order Fermi acceleration mechanism" (see Section 1.4.2), which can explain a flux proportional to E^{-2}; at this point different effects change the spectrum in the observed one.

The lowest energy band is dominated by particles trapped in the *solar wind*[3] [54]. The variability of their rate follows the solar cycle. In fact, during periods of high solar activity the solar wind interacts with the incoming CRs, disturbing their propagation to the Earth and reducing the observed flux. Conversely, the CRs flux reaches its maximum during the periods of low solar activity. This phenomenon is known as solar modulation and has a cycle of about 11 years. In the second band the

---

[3]Charged plasma emitted by the Sun.
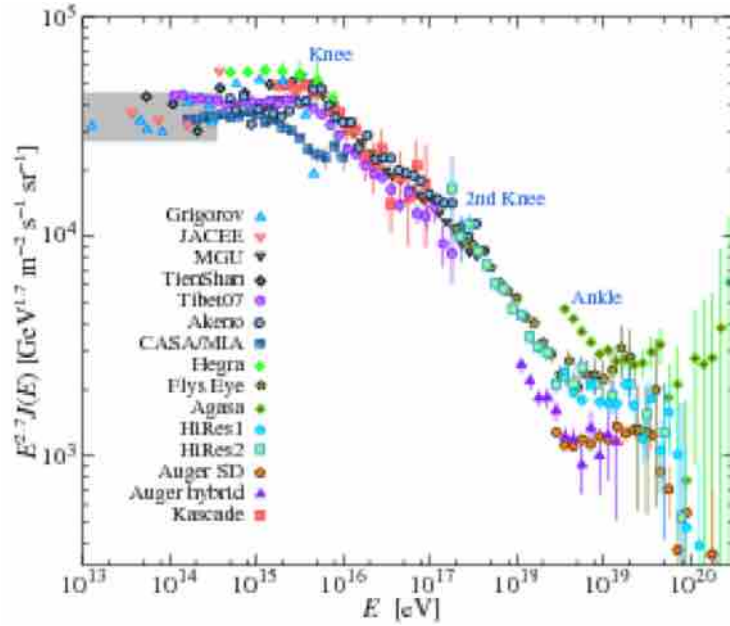
Figure 1.4. All-particle spectrum of cosmic rays, reconstructed from air showers observed
by various experiments (from [23]). The differential energy spectrum has been multiplied
by $E^{2.7}$ in order to display the features of the steep spectrum that are otherwise difficult
to discern (the *second knee* at 10^{17} eV) [23]. The grey box is the region where direct
observations of cosmic rats have been made. AGASA measurements show events with
energy $\geq 10^{20}$ eV [116], in contrast with the GZK cut-off.

confining effect due to the galactic magnetic field works by changing the spectrum.
Beyond the ankle CRs can not be confined in the galaxy volume by the galactic
magnetic field and so this break in the spectrum slope could mark the transition
between galactic and extragalactic cosmic rays.
Above 1 EeV particles are considered to be of extragalactic origin, because the radius
of curvature of their trajectories in the galactic magnetic field exceeds the size of the
Galaxy. The origin of the particles beyond the knee is not yet understood. Several
models have been proposed to explain the acceleration mechanism bringing CRs to
these extreme energies. There are three most developed scenarios:

- A change of the propagation of galactic cosmic rays, corresponding to a more
  rapid particle escape from the Galaxy [106].

- A change of the acceleration mechanism is directly responsible for the knee. It
  is argued that the maximal energy of acceleration in supernova shock fronts
  corresponds to the knee energy (see e.g. [81]).

- Presence of only one or few sources (supernovae) nearby the Earth. The
  consequences of this assumption to the cosmic ray spectrum are developed in
  [51].

The flux is then strongly suppressed at energies above $4 \cdot 10^{19}$ eV. For these reasons
Ultra High Energy Cosmic Rays (UHECRs) are a topic of high importance. Greisen
[68], Zatsepin and Kuzmin [88], after the discovery of 2.7 K black body relict
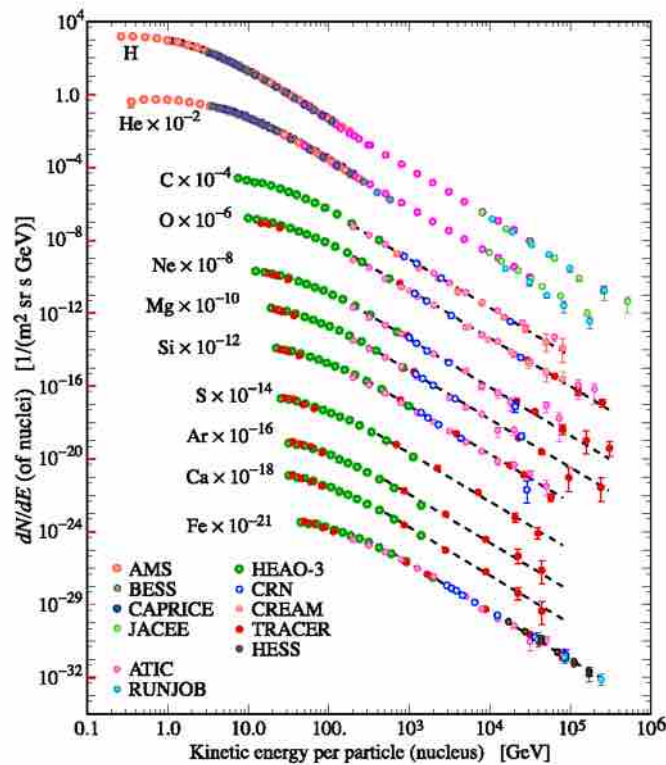
Figure 1.5. Fluxes of nuclei of the primary cosmic rays as a function of the kinetic energy per nucleus [35].

radiation (*Cosmic Microwave Background*, CMB), pointed out that the power law of CRs should not exceed the energy at which they start interacting with the CMB. The involved reaction (with threshold of about $\sim 6 \cdot 10^9$ GeV) is:

$$p + \gamma_{\mathrm{CMB}} \overset{\Delta^+}{\to} \begin{cases} p + \pi^0 \\ n + \pi^+ \end{cases} \tag{1.2}$$

where protons p interact with remnant photons from the Big Bang, γ_{CMB}, via Δ^+ resonance producing a nucleon (either a proton or a neutron) and a pion that is either positively charged (π^+) if a neutron is created or neutral (π^0) if joined by a proton. Below the threshold energy the proton attenuation length is 1000 Mpc, while above the threshold it is reduced only to 20 Mpc. Similar effect appears, at higher nuclei energies, also for heavier nuclei and it is known as GZK cut-off. It would limit propagation of UHECRs to distances of order 20 Mpc and within this distance no suitable astrophysical source is known.

However, measurements by Akeno Giant Air Shower Array (AGASA) experiment observed significant number of events above the GZK cut-off (11 events above 10^{20} eV) [116][109][113] but this is the only measure that does not seem to observe the GZK cut-off so far. Other experiments, like HiRes [34] and the Pierre Auger Observatory [14], made measurements in this energy region by confirming a reduction of the particle flux for energies above the GZK threshold. (Figure 1.4).

Figure 1.5 shows that the energy spectrum for the different nuclei that compose

the CRs is consistent with the overall spectrum up to energies close to the knee. The study of the relative abundances of these elements gives information about the acceleration mechanisms at the source and the propagation mechanisms in the Interstellar Medium (ISM). Indeed, any theory explaining the features in the cosmic ray spectrum will be tied to the composition at the energy of the feature.

1.3 Composition

Through experiments performed at high altitude (with balloons like or satellites) it has been possible to determine the composition of cosmic rays in the energy range between 10^8 eV and 10^{14} eV; for energies beyond 10^{15} eV the flow is so small (as shown in Figure 1.3) which requires the use of large detectors, necessarily on the Earth's surface, that allow to study the particle showers produced by the primaries.
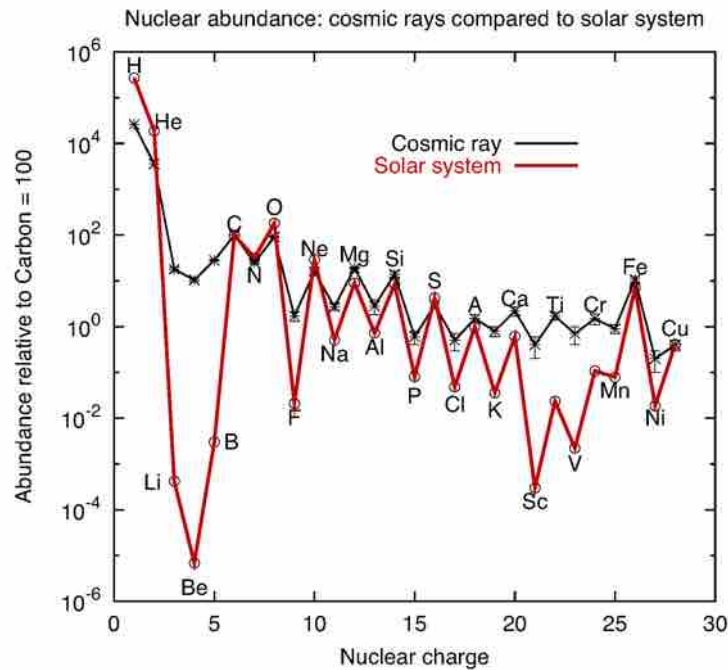
Figure 1.6. Abundances of elements observed in the cosmic rays compared to the Solar System abundances. Abundances normalized to the value of 100 for Carbon.

Experiments showed that CRs are composed by protons (H, 85%), α particles (He, 12%), electrons (2%) and the remaining 1% by photons, heavy nuclei and neutrinos [58]. Comparing this composition with the abundances of metals in the solar system (Figure 1.6) it is immediate to assume that a large fraction of cosmic rays is produced in stellar environments, and their interaction with the interstellar medium (ISM) is responsible for the differences between the two distributions. In fact, in the CRs, elements lighter as Li, Be and B are much more abundant, and Sc, Ti, V, Cr and Mn are among the heaviest ones. These elements are present in CRs since produced by the interaction of oxygen and iron atoms respectively with the ISM by means of spallation reactions.

At lower energies these measurements are easier than at highest ones, mainly because at high energy, when the particle fluxes can be studied only by analysing the extensive air showers induced by the primary CR interactions, the mass reconstruction becomes difficult. For this reason the UHECRs composition is still very much under debate. Some observations favor a transition towards heavier elements just before the cut-off [1], while other are also compatible with a pure proton composition [115].

1.4 Acceleration Mechanisms

The power law behavior of the energy spectrum observed by Earth (see Section 1.2) is most probably indicative of a power law acceleration spectra, while spectral features may be assigned to changes in the origin of particles and/or their propagation.

Energy spectrum produced by Fermi acceleration

Let consider the energy transfer ΔE following a random collision involving particles. It is proportional to the energy of the particle itself:

$$\Delta E = \xi E, \tag{1.3}$$

where ξ is then the amount of increasing energy; after n collisions the energy of a cosmic ray becomes

$$E_n = E_0(1 + \xi)^n \tag{1.4}$$

and the number of cycles needed to reach it is

$$n = \frac{\ln\left(\frac{E}{E_0}\right)}{\ln(1 + \xi)}. \tag{1.5}$$

The probability that the particle is confined until it achieves an energy E_n is given by the ratio between the involved number of particles N and the initial one N_0:

$$P^n = \frac{N}{N_0}. \tag{1.6}$$

From Equation 1.6 and by using Equation 1.5 the following expression can be obtained:

$$\ln\left(\frac{N}{N_0}\right) = \ln\left(\frac{E}{E_0}\right)^s, \tag{1.7}$$

where $s = -\ln P/\ln(1 + \xi)$. Therefore, the differential energy spectrum is naturally described by a power law:

$$\frac{dN}{dE} \propto E^{-(1+s)}. \tag{1.8}$$

Our knowledge about energy spectrum and composition of cosmic rays must find

a valid process responsible for the particle energy gain. The general equation of motion for a charged particle is:

$$\frac{d}{dt}(\gamma m \vec{v}) = q(\vec{E} + \frac{\vec{v} \times \vec{B}}{c}),$$ (1.9)

where $\gamma = 1/\sqrt{1 - \frac{v^2}{c^2}}$ is the Lorentz factor, q, m and $\vec{v}$ are the charge, mass, and velocity of the particle, respectively. Equation 1.9 shows magnetic fields themselves do not work and can not be directly responsible for acceleration. A charged particle can be accelerated (its speed is changed) by increasing its energy and this can only be done by electric field, which are generated by variable magnetic fields.

1.4.1 Fermi acceleration of the II order

In 1949 Enrico Fermi proposed an acceleration mechanism due to collisions between particles and "clouds" with magnetic field irregularities inside them (*magnetic mirrors*), moving isotropically in the interstellar medium [52]. After having crossed several times regions with unevenness of the magnetic field, the energy of the particles increases because head on collisions are on average more frequent. The energy gain at every cloud reflection is equal to:

$$\left\langle \frac{\Delta E}{E} \right\rangle \sim \frac{4\beta^2}{3}.$$ (1.10)

For this reason this mechanism is also known as *Fermi acceleration at second order* in $\beta = v/c$ and it is actually not very efficient because the value in Equation 1.10 is too small.

Starting from this theory, another one was developed, in which interactions of particles with a hydrodynamic shock wave can possibly take place: the *Fermi acceleration of the first order*, explained in the following Section 1.4.2.

1.4.2 Fermi acceleration of the I order

One of the several physicists that independently modified the study previously done by Fermi was Anthony Raymond Bell in 1978 [30]. He improved the efficiency of the acceleration mechanism by hypothesizing a transfer of energy caused by strong shock-wave fronts moving in the interstellar medium with supersonic velocity $U \gg c_s$, where c_s is the sound speed in a material. Consider the *upstream* fluid, not yet reached by the shock, and the *downstream* one, already reached and exceeded by it. The shock front is a transition zone in which the velocity of the fluid quickly change because of the supersonic motion of the supernova ejecta. Particles can pass through the shock in either direction by starting a series of diffusion processes due to the local turbulent (irregular) magnetic field; they are then scattered and their velocity distribution rapidly becomes isotropic in the frame of reference of the moving fluid on either side of the shock. This process can happen several time causing the energy gain of the particles.
The explanation of this topic will be now addressed by following Bell's paper (1978) [30] and the Longair discussion [94]. Let consider the reference frame in which the
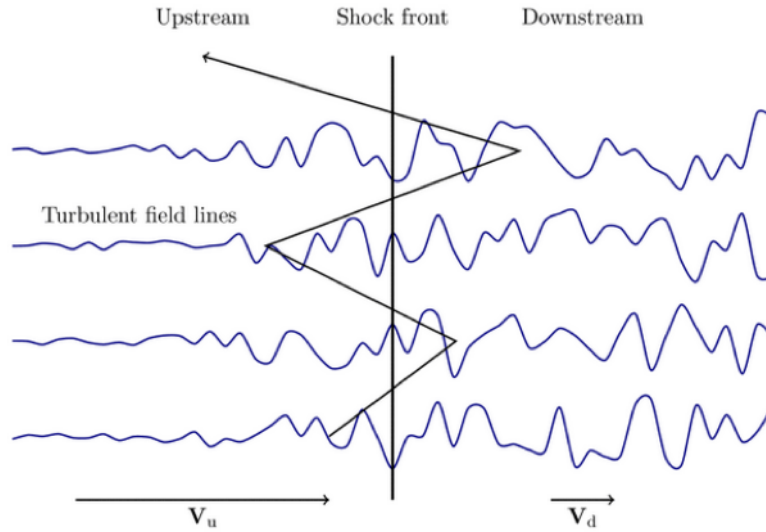
Figure 1.7. Cartoon picture of Fermi acceleration of the Second type. A schematic typical path of a shock-accelerated particle is shown. Each encounter with the shock yields an average gain of energy, due to the converging flow velocities at the shock front. Dr. Mark Pulupa's space physics illustration: http://sprg.ssl.berkeley.edu/~pulupa/ illustrations/.

shock front is at rest: an observer sees the upstream fluid coming towards him with velocity $v_1 = U \gg c_s$ and the flow behind him leaves the shock with a downstream velocity v_2. Let be ρ_1 and ρ_2 the gas densities in the upstream and the downstream fluid respectively, the equation of continuity requires:

$$\rho_1 v_1 = \rho_2 v_2 \Rightarrow \frac{\rho_2}{\rho_1} = \frac{v_1}{v_2}. \tag{1.11}$$

In the case of a supersonic shock,

$$\frac{\rho_1}{\rho_2} = \frac{\frac{c_p}{c_v} + 1}{\frac{c_p}{c_v} - 1}, \tag{1.12}$$

where c_p and c_v are the specific heats at constant pressure and temperature, respectively. Taking $c_p/c_v \sim 5/3$ for a monoatomic of fully ionised gas, from Equation 1.11 follows that $v_2 = v_1/4$.

Consider now the reference frame of the upstream fluid. The shock moves towards this fluid with velocity U but the downstream one advances towards the observer with velocity $V = 3/4U$. Particles in the upstream fluid collide and can cross the shock front to the downstream. The particle's energy when passing through this region is:

$$E' = \gamma_V (E + p_x V), \tag{1.13}$$

where p_x is the projection of the momentum perpendicular to the shock. It is assumed a non-relativistic shock ($\gamma_V \simeq 1$), but the particle's velocity is close to the sound speed, so $E = pc$ and $p_x = p \cos\theta \simeq E \cos\theta/c$. Therefore,

$$\Delta E = E' - E \sim \frac{E}{c} V \cos\theta \Rightarrow \frac{\Delta E}{E} = \frac{3}{4} \beta \cos\theta. \tag{1.14}$$

Now it must be considered that the particles which cross the shock can arrive from different angles from θ to $\theta + d\theta$. Being the probability that a particle arrives within this range proportional to $\sin\theta d\theta$ and the rate at which they approach the shock front proportional to $c\cos\theta$, it can be shown that the average energy gain is:

$$\left\langle \frac{\Delta E}{E} \right\rangle = \frac{V}{c} \int_0^{\pi/2} 2\cos^2\theta\sin\theta d\theta = \frac{2}{3}\frac{V}{c}. \tag{1.15}$$

If the opposite situation (from downstream to upstream) is considered, an analogous result can be reached, obtaining the same amount of energy gain indicated in Equation 1.15. Therefore, in a round trip across the shock and back again, the fractional energy increase is, on average,

$$\left\langle \frac{\Delta E}{E} \right\rangle = \frac{4}{3}\frac{V}{c} \sim \frac{U}{c} \sim \beta. \tag{1.16}$$

At this point the question is: what is the escape probability of particles from acceleration sites? According to classical kinetic theory, the number of particles crossing the shock in either direction is $Nc/4$, with N the number density of particles. The particles move away from the acceleration region because of collisions with a rate $NV = NU/4$. Thus, the fraction of the particles lost per unit time is:

$$\frac{\frac{1}{4}NU}{\frac{1}{4}Nc} = \frac{U}{c}. \tag{1.17}$$

Only a small fraction of the particles is lost per cycle because the shock is assumed to be non-relativistic. This allows particles to undergo several acceleration cycles and achieve energies of the order of $\sim 10^{15}$ eV on the relevant timescale for SNR shock expansion. Therefore, the escape probability is:

$$P = \frac{U}{c}. \tag{1.18}$$

Considering these results, the differential energy spectrum in Equation 1.8 becomes:

$$\frac{dN}{dE} \propto E^{-2}. \tag{1.19}$$

In this way it is demonstrated that the Fermi acceleration at first order is much more efficient than the original mechanism explained by Fermi himself, but it is still not enough; the spectrum in Equation 1.19 is a simple power law with spectral index $\gamma = 2$, hence it does not match the observational properties of CRs. However, a complete description of the flux measured at Earth should consistently include the propagation of CRs from their acceleration site to the Earth. This process is partially responsible for the steepening towards $E^{-2.6}$.

Lagage and Cesarsky [90] described this process for shock wave fronts produced close to supernova explosions; in the hypothesis of shock velocity parallel to magnetic field direction, the finite lifetime of the shock limits the maximum energy per particle that can be achieved at supernova shock to $E_{\text{max}} \sim 10^{14}$ eV × Z) [59]. This value is obviously too low because we observe more energetic particles too (see Figure 1.3), therefore accelerations near supernovae does not explain the whole particle spectrum and there must be other sources for more energetic cosmic rays.

1.5   Galactic or Extragalactic origin

The change in the slope of the energy spectrum and in the composition from protons to iron in the knee region suggests that there are two different kind of cosmic ray sources: **galactic** and **extragalactic**.

An argument favoring an extragalactic origin of cosmic rays for the highest energies is the isotropy of their arrival directions on large scales that could suggest a cosmological distribution of their sources. However, some experiments have shown anisotropies in CRs flux (Pierre Auger Observatory [2], TibetASγ [22], ARGO-YBJ [114], Milagro [12] and IceCube [5]). This deviation from the expected isotropy could be due to a non-uniform distribution of the sources, which are at the level of few parts per hundreds ot even thousands [33] [72] [73].

It is possible to establish the origin of cosmic rays as a function of energy with simple scale considerations. The distance scale that a charged particle may travel inside a magnetic field is of order of its *Larmor radius* or *gyroradius*[4] [40]. For a particle with charge $q = eZ$, velocity $v = \beta c$, immersed in a magnetic field B it is given by:

$$R_L = \frac{E}{Z|e|\vec{B}\beta c}.$$ (1.20)

For a relativistic proton ($Z = 1$ and $\beta \sim 1$) it becomes:

$$R_L[pc] = 1.08 \cdot 10^{-21} \frac{E[\text{eV}]}{B[\text{G}]}.$$ (1.21)

If we consider the energy value $E = 10^{18}$ eV and the magnetic field that fills the Galaxy (average density $B \approx 4\ \mu$G), we obtain $R_L = 300$ pc, comparable to the vertical dimension of the Galactic disk (see Figure 1.8). At low energies, therefore, the origin of CRs is predominantly galactic, instead the high-energy cosmic rays are less bound to the Galaxy.
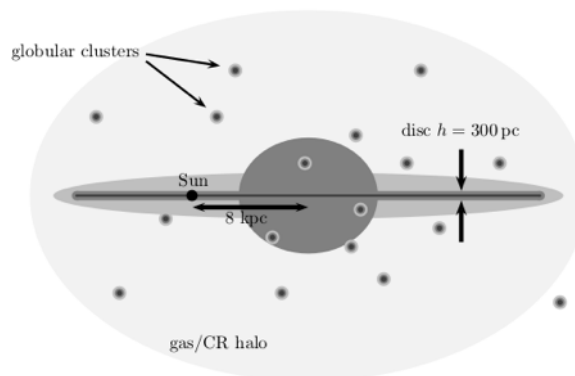
Figure 1.8.   Simplified model of the structure of the Milky Way galaxy with a gas and dust disc, an extended halo of gas and cosmic rays, surrounded by globular clusters. Everything is immersed in a halo of dark matter. [79]

---

[4]Radius of the circular motion of a charged particle in the presence of a uniform magnetic field.

We should keep in mind that at a given energy the gyroradius is larger for smaller charge of the particle. Therefore, if UHECRs are mostly protons, due to their large gyration radius, they would be not deviated significantly by magnetic fields, so they should point back to their sources within an angle that depends on the intensity of the intergalactic magnetic field. This concept is at the base of the so-called proton astronomy, which however constitutes a challenging task due to the very limited particle flux in the UHECR domain. For heavy nuclei, the effect of the magnetic field becomes more important. If heavy elements are found to be in the UHECR flux on Earth, they also have to be present at the acceleration sites.

1.6   Sources of High Energy CRs and Hillas plot

Since the CRs discovery we have learned about many of their features, such as their large energy span, their composition and the behavior as a function of energy, of their flux but the source and origin of the highest-energy cosmic rays still elude us.

The so-called *Hillas criterion* [79] helps to answer these questions. This is in fact the minimal condition that a source must satisfy in order to be able to accelerate particles to ultra-high energies: the Larmor radius 1.20 must be smaller than the size scale R of the system. For known magnetic fields and source sizes, one can constrain thus the maximal achievable energy as:

$$E_{\mathrm{max}} = \Gamma q B R. \tag{1.22}$$

The Lorentz factor Γ introduced in Equation 1.22 accounts for a possible relativistic bulk motion of the source and it is relevant only for gamma-ray bursts (treated in depth in Section 2) and other relativistic sources [79].

Thanks to the Hillas-Plot in Figure 1.9 one can classify some potential astrophysical sources for cosmic rays at different energies based on their physical characteristics: magnetic field B and linear size R. It shows that possible accelerators range from neutron stars (≈ 10 km), namely remnants that can result from the gravitational collapse of a massive star in a supernova explosion, up to galaxy clusters, which can compensate small B values for large dimensions of the confinement zone (order of Mpc).

Even by just applying the Hillas criterion, quite a lot of objects can be ruled out as UHECR sources. In order to reach very high energies, there is a need for both very high magnetic fields and large dimensions of sources. In the first case, however, the contribution of synchrotron radiation becomes important for protons too (the power emitted P_{synch} is proportional to B^2), so the energy loss by particles is too high; in the second one, this kind of objects takes more time to accelerate the particles, which are lost because they can interact with CMB photons by producing pions. For these reasons neutron stars (with very high B) and galaxy clusters (too larger in size) can be excluded as UHECRs sources. A better candidate for the higher energy cosmic radiation is the acceleration in compact sources: Gamma-Ray Bursts (GRBs) and Active Galactic Nuclei (AGN).
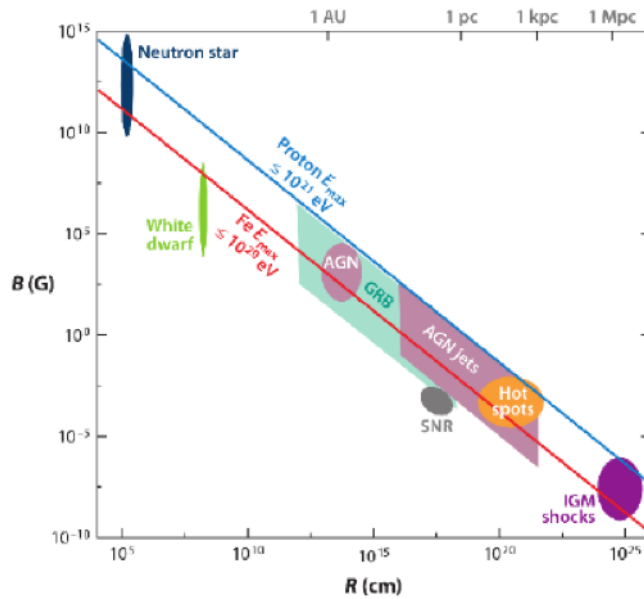
Figure 1.9. Hillas Plot [83]. It relates the magnetic field B in potential cosmic rays sources to their dimension R. The diagonal lines show the regions for which the product BR satisfies the Hillas criterion for different composition of the primary cosmic rays, i.e. protons with $E = 1\ ZeV = 10^{21}$ eV (blue line) or iron nuclei with $E = 100$ EeV$= 10^{20}$ eV (red line). Uncertainties on the parameters are taken into account and increase the covered area.

1.6.1   Supernovae Remnant

Most galactic astrophysical sources are connected with type II (or core-collapse) supernovae (SN) and their remnants (SNRs). A SN II is the end of the fusion process in massive stars, $M \gtrsim (5 \div 8) M_{\odot}$, which produces a shock wave propagating in the interstellar medium and an expanding ejected material.

These stars have an onion-like structure with a degenerate Fe core; after its completely fusion in iron, processes releasing energy are not possible. Instead, photodisintegration detroys the heavy nuclei and removes the thermal energy necessary to provide pressure support ($\gamma +^{56}$ Fe $\rightarrow^4$ He $+ 4n$). When the star collapses the density increases and the free electrons are forced together with protons to form neutrons via inverse beta decay ($e^- + p \rightarrow n + \nu_e$) and a proton-neutron star forms. If the core density reaches nuclear densities the infalling material is "reflected" and a shock wave propagates outwards heated by neutrino emission from the beta-decay. The released gravitational binding energy is:

$$\Delta E = \left[-\frac{GM^2}{R}\right]_{star} - \left[-\frac{GM^2}{R}\right]_{NS} \sim 5\times10^{33}\ \text{erg} \left(\frac{10\ \text{km}}{R}\right) \left(\frac{M_{NS}}{1.4 M_{\odot}}\right), \quad (1.23)$$

and it is emitted mainly via neutrinos (99%) because of beta-decays. Only 1% is transferred into kinetic energy of the exploding star and only 0.01% goes into photons. At the end of this process a neutron star is left over and a black hole remains [79].

There are some recent observations (SNR W44 [44] and IC433 [117], for example) which suggest that bulk of galactic cosmic rays is originated from SNRs. Nonetheless, in the standard model of cosmic ray acceleration by supernova blast waves particles would not be able to achieve to the highest observed energies (see previous explanation in Section 1.4.2).

1.6.2 Pulsars

A pulsar is a rapidly rotating neutron star, expected being at the center of a SNR, that emits a beam of electromagnetic radiation observable only when the beam of emission is pointing toward Earth. Neutron stars are very dense, and have short, regular rotational periods. This produces a very precise interval between pulses that range from milliseconds to seconds for an individual pulsar, according to the evolutionary stage of the pulsar itself.

It is expected that pulsars and their Pulsar Wind Nebulae (PWNe) could be viable sources of CRs [70]. Pulsars have indeed extremely strong magnetic fields that, if fast rotating, may accelerate particles to high energies. The energy is in fact lost as electromagnetic dipole radiation by producing an electromagnetic wave that causes a relativistic wind of e^+e^-. This latter propagates in the surrounding medium and generates a shock wave responsible for the CRs acceleration.
The maximum acceleration energy achievable by a pulsar is:

$$E_{\text{max}} = 8 \times 10^{20} \text{ eV} \frac{ZB}{10^{13} \text{ G}} \left(\frac{\Omega}{3000 \text{ s}^{-1}} \right)^2, \tag{1.24}$$

where Ω is the angular velocity related to the pulsar period $P = \frac{2\pi}{\Omega} \approx 10^6$ s. Thus, a young, fast rotating pulsar appears to be a very good particle accelerator. Finally, pulsars as main sources of UHECRs would predict a strong anisotropy of their intensity, because neutron stars are concentrated in the Galactic plane [79], which however is not observed. Moreover, the fact that pulsar are mainly producing leptons collides with compositional studies of CRs. Hence, pulsars are not believe to be strong contributors to the observed CR flux.

A famous example of a pulsar surrounded by its own nebula is the Crab Nebula (Figure 1.10), the remnant of a SN observed by Chinese astronomers in 1054 which has been emitting γ-radiation of energy $\approx$ TeV for around 1000 years.

1.6.3 Active Galactic Nuclei

Active Galactic Nuclei (AGN) are galaxies with an unusual emission that is not associated with stars and produces a non-thermal component in the Spectral Energy Distribution (SED)[5], in contrast to normal galaxies whose total luminosity is the sum of the thermal emission from each star. This difference from usual galaxies is due to the presence of a super massive black hole (SMBH) in their center, which is actively accreting matter from the surrounding environment. This allows them to

---

[5]Energy emitted by an object as a function of the emitted frequency.
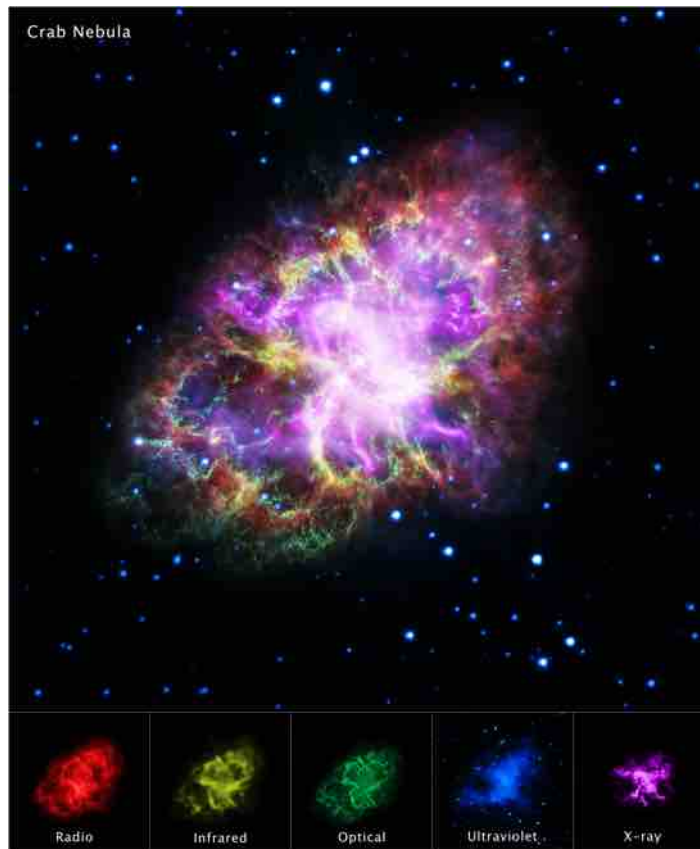
Figure 1.10. Crab Nebula by five observatories: VLA/NRAO/AUI/NSF, Chandra/CXC, Spitzer/JPL-Caltech, XMM-Newton/ESA, and Hubble/STScI. Credit: NASA https://photojournal.jpl.nasa.gov/figures/PIA21474_fig1.jpg

reach extremely high luminosity values ($\approx 10^{48}$ erg/s). Consider the accretion onto a black hole; the maximal energy gain is

$$E_{\max} \sim \frac{GmM}{R_S} \stackrel{R_S = 2GM/c^2}{\rightarrow} E_{\max} = \frac{mc^2}{2} \qquad (1.25)$$

where R_S is the Schwarzschild radius[6], G is the gravitational constant, M is the mass of the central BH, m is the accreting mass and c is the speed of light. A large part of this energy is lost in the black hole, while the remainder heats up via friction an accretion disc (optically thick disk of material) around the black hole. The luminosity from accretion is

$$L = \frac{\epsilon c^2 dm}{2 dt}. \qquad (1.26)$$

By replacing standard values for the black hole activity ($dm/dt = 1$ M$_\odot$/yr) and the accretion efficiency ($\epsilon = 5\% - 42\%$, depending on the spin of the black hole [75]), high luminosities are obtained. There exist different types of AGN, illustrated in

---

[6]Radius of the event horizon surrounding a non-rotating black hole. Any object with a physical radius smaller than its Schwarzschild radius will be a black hole. This quantity was first derived by Karl Schwarzschild in 1916.

(a)   **(b)**
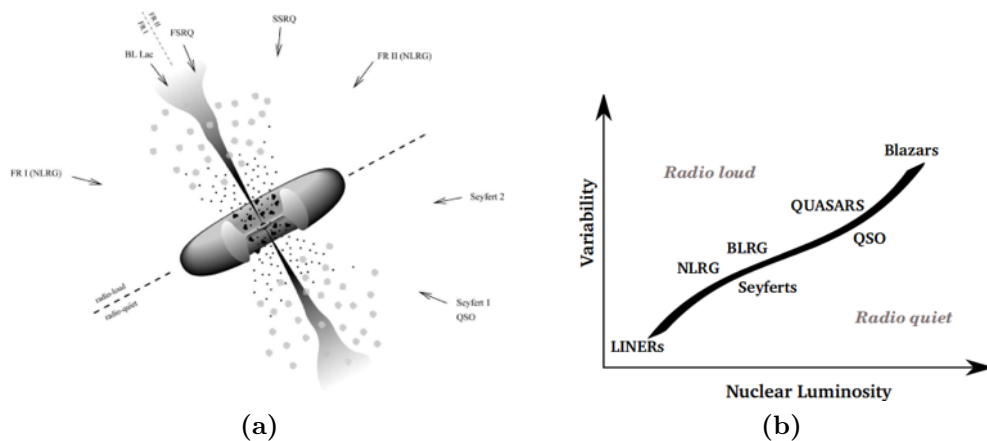
Figure 1.11. Figure (a): The unified scheme of AGN. [79]. Figure (b): AGN classification
scheme. [56].

Figure 1.11, unified by the same phenomenon-accretion. The different characteristics,
for example the fast variability of their spectra, is a consequence of different angles of
view, different stages of activity and evolution in time. The most interesting active
galaxies for us are **Blazars**, AGN with a relativistic jet pointed in the direction
of the Earth, which makes them the most promising sources of ultrahigh energy
cosmic rays. If the jet points directly towards the observer, the relativistic beaming
effects make the source appear very luminous in the radio band and often extremely
variable [56].

AGN have also considered very promising sources of high-energy neutrinos un-
til now and this has been recently confirmed by IceCube, which found a coincidence
in direction and time between an high-energy neutrino event detected on 22 Septem-
ber 2017 and a gamma-ray flare from the blazar TXS 0506+056 [8]. This suggests
that blazars are possible contributors to of the high-energy astrophysical neutrino
flux. This discovery is very important because the detection or not of neutrino
radiation from AGN or other astrophysical objects (e.g. GRBs) can provide unique
information about the processes characterising of their central engine and the pres-
ence of relativistic protons of sufficiently high energy in the relativistic jet (see
Chapter 2 for the explanation of this topic, done in the the context of gamma-ray
bursts but also valid for AGN).

1.6.4   Gamma-Ray Bursts

Gamma-Ray Bursts are the most luminous objects in the Universe and represent
highly beamed sources of gamma-rays and perhaps also of high energy neutrinos
and cosmic rays: in the internal shock scenario, blobs of plasma emitted from a
central engine collide within a relativistic jet and form shocks, producing particle
acceleration and neutrino emission. A distinctive feature is the high Lorentz factor
of shocks in GRBs, which however poses severe challenges to the efficiency of shock
acceleration in these extreme environments.
For a detailed description of these objects, refer to Chapther 2.

Chapter 2

Gamma-Ray Burst

Gamma-Ray Bursts (GRBs) are brief pulses of gamma-ray radiation as a consequence of the most powerful known explosions in the Universe. They were casually discovered by the U. S. Vela satellites[1], built to detect the gamma radiation pulses emitted by nuclear weapons tested in the space.

The first unexpected signal was detected in 1967 and subsequently Klebesadel et al. (1973) [80] showed that Vela spacecraft observed sixteen short burst of photons in the energy range $0.2 - 1.5$ MeV between 1969 July and 1972 July. Bursts duration ranged from less than 0.1 s to ~ 30 s and time-integrated flux (also called fluence) from $\sim 10^{-5}$ erg cm^{-2} to $\sim 2 \times 10^{-4}$ erg cm^{-2}. Several count rate records were composed by a number of clearly resolved peaks, showing significant time structure within bursts, while other did not appear to display any significant structure.
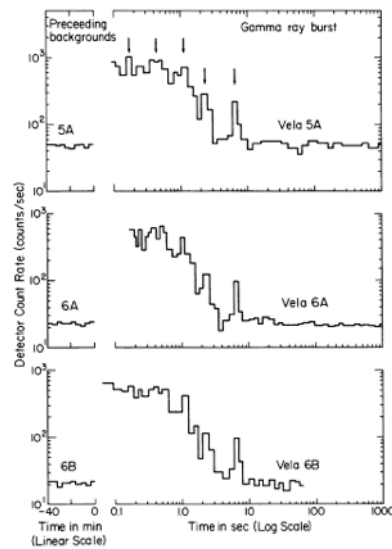
Figure 2.1. Count rate as a function of time for the GRB of 1970 August 22 as recorded by three Vela spacecrafts. Arrows indicate some of the common structures. Background count rates preceding the burst are also shown [80].

---

[1]Satellites launched by the United States starting from 1963 to monitor compliance with the treaty "banning nuclear weapon tests in the atmosphere, in outer space and under water" signed by the governments of the Soviet Union, the United Kingdom and the United States in 1963.

These bursts were not related in time or direction to any nova or supernova and it was demonstrated also that the energy observed was consistent with an extreme explosion as a source. It was also checked that these bursts were not coming from the Sun, Moon, or other planets in our solar system. Interestingly, the first evidence for the source at the origin of GRB is constituted by the simultaneous detection of gravitational waves in space and time correlation with the high-energy gamma-ray emission of a short GRB, namely GRB170817A [11]. For this class of GRB, namely where the duration of the emission is faster than 2 s, binary systems of colliding neutron stars are believed to be the progenitors of the emission. On the other hand, for long GRB (gamma-ray duration longer than 2 s), core-collapse SNe are considered the most plausible progenitor candidates.

2.1 Majors experiments and their results

BATSE: 1991-2000

In 1991 GRB study really began, when the *Compton Gamma-Ray Observatory* (CGRO) was launched from space shuttle Atlantis in a low Earth orbit, at 450 km, to observe the high-energy Universe. It carried four different instruments, that provided a wide energy band coverage of 20 keV - 30 GeV: the *Burst And Transient Source Experiment* (BATSE), the *Oriented Scintillation Spectrometer Experiment* (OSSE), the *Imaging Compton Telescope* (COMPTEL) and the *Energetic Gamma-Ray Experiment Telescope* (EGRET).

BATSE, in particular, was an important starting point for the study of GRBs; one of its primary objectives was the study of those phenomena at that time still mysterious, which are the gamma-ray bursts [55]. It was sensible in an energy range going from 20 keV to 10 MeV. Eight uncollimated detector modules were positioned around the spacecraft to provide an unobstructed view of the sky (see Figure 2.2). The plastic scintillator, a large-area detector, provided a high sensitivity for weak bursts and fine time structure studies for the stronger ones. A spectroscopy scintillation device was included in each detector module: it was optimized to obtain better energy resolution and to cover a wider energy range than the large-area detector.
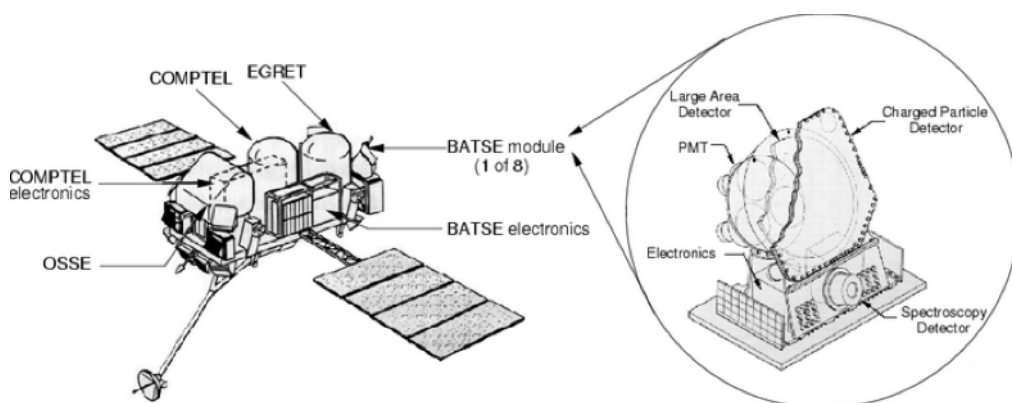
Figure 2.2. The Compton Gamma Ray Observatory and one of the eight BATSE detector modules. Credit: National Space Science and Technology Centre, Huntsville, AL, USA.

BATSE was able to see the whole sky and detected about 1 GRB per day, identifying the extragalactic origin of GRBs as probed by the isotropic angular distribution of these events (see Figure 2.3) [99]. Thanks to an analysis of 153 gamma-ray bursts, a deficit on low luminosity (and thus in energy, too) GRBs was seen, indicating that they are either located in galaxy halos, or are from cosmological origin, in which case the deficit at low energy would be due to the expansion of the Universe.
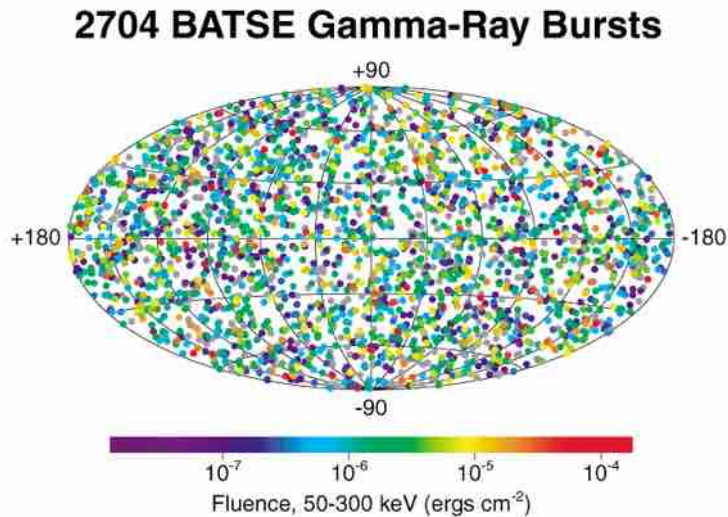
Figure 2.3. Locations of the Gamma ray bursts detected by BATSE projected in galactic coordinates (the Milky Way stretches horizontally across the centre of the figure). The colours indicate the energy and duration of each burst: long duration bright bursts appear in red while short duration weak bursts in purple. The grey points indicate bursts for which the energy and/or duration could not be calculated. Figure from https://gammaray.nsstc.nasa.gov/batse/grb/skymap/.

Furthermore, BATSE clearly saw two distinct populations of burst, **short** and **long** (for more details see Section 2.2.2) but, except for their duration, it did not find other significant differences, due to the lack of additional data.

Beppo-SAX: 1996-2002
Beppo-SAX was an Italian satellite launched on April 30, 1996. It had on board various X-ray detectors (to measure a radiation lower in energy than gamma) in addition to a GRB monitor. Therefore, it was the first X-ray mission with a scientific payload covering an energy range from 0.1 to 300 keV and with the ability to provide an angular position of bursts to within 4 arc-minutes (improved more than a factor 20 if compared to the CGRO) [87]. This allowed to observe for the first time the **afterglow**, a rapidly fading X-ray emission associated with the GRB jet expansion in the ISM. On February 28, 1997, Beppo-SAX saw a burst and, about a day after, an X-ray afterglow [48]. Ground-based spectrometers were able to measure also the optical spectrum of the afterglow.
The extragalactic origin of GRBs (cosmological distances, i.e. $z \sim 1$) was unequivocally established three months later, when GRB 979508 was localized and its redshift was estimated ($z \sim 0.84$) [96].

Thanks to Beppo-SAX, could also be estimated the energy involved in these phenomena. From the measured values of the burst redshift and of the flux, it was obtained that GRBs radiate $10^{48} - 10^{55}$ erg (if isotropic). This means that GRBs are the most energetic and explosive sources in the known Universe [86].

This opened a new era in the study of these objects with important questions:

- Can these distant objects exist with such a great flow?

- What does cause them?

Swift: 2004-now

Swift Gamma Ray Burst Explorer, or simply *Swift*, was launched into a low-Earth orbit on November 20, 2004 and is still operating. It is composed by three instruments working together to provide rapid identification of GRBs and to observe afterglows in the gamma-ray, X-ray, ultraviolet and optical wavebands [61]:

- *Burst Alert Telescope* (BAT): 15-150 keV
  With its large field of view (2 sr) and high sensitivity, it detects about 100 GRBs per year and computes burst positions onboard the satellite with arc-minute positional accuracy.

- *X-ray Telescope* (XRT): 0.3-10 keV
  It takes images and is able to obtain spectra of GRB afterglows during pointed follow-up observations.

- *UV/Optical Telescope* (UVOT): 170-600 nm
  It takes images and can obtain spectra of GRB afterglows during pointed follow-up observations. It provides a position localization of about 0.5 arcsec and allows to track the temporal evolution of the UV/optical emission.

The important discovery made by Swift is represented by the first localization of a short GRB with its afterglow, in that such an observation had never been performed before (GRB 050509B). Gehrels et al. (2005) [62] found that its position on the sky was near a luminous, non-star forming elliptical galaxy at redshift $z = 0.225$, exactly the type of location one would expect if the origin of this GRB is the merger of neutron star or black hole binaries. This, combined with correlations of long GRBs with supernovae, allowed to partially address the origin of these objects, after more than 30 years since their discovery.

Swift satellite has also found GRBs at very high redshift, until $z = 9.4$, when the Universe was just 0.52 billion years old [49]. Therefore, GRBs represent important probes of the end of cosmic dark age, when the first stars and galaxies were forming.

Fermi: 2008-now

The *Fermi* satellite, launched in June 2008 and still in operation, has been providing useful data measuring radiation in an energy window extending from ~ 8 keV to > 300 GeV to help answer some open issues about GRBs: what phenomenon does produce so much energy? What happens to the surrounding environment near these
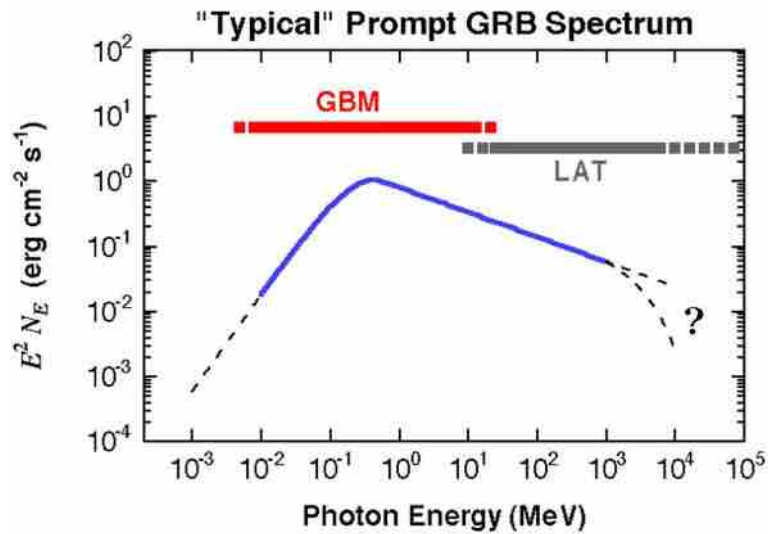
Figure 2.4. Band spectrum. In red and grey gamma-ray burst spectral coverage of the GBM and the LAT, respectively, are indicated.

phenomena? How will the study of these energetic objects improve the understanding of the nature of the Universe and how it behaves?

This satellite is constituted by two instruments:

- *Gamma-Ray Burst Monitor* (GBM): 8 keV-40 MeV
  It is dedicated to the study of GRBs by extending the LAT energy range over the full unocculted (by the Earth) sky. It uses an array of twelve sodium iodide scintillators and two bismuth germanate scintillators to detect gamma rays. GBM generates on-board triggers for ~ 250 GRBs per years with a large field of view ($\sim 8°$) [95].

- *Large Area Telescope* (LAT): 20 MeV-300 GeV
  It is able to detect the direction and energy of gamma rays with unheard-of resolution and sensitivity by using 880000 silicon microstrip detectors. It has a reduced field of view with respect to GBM, around 2 sr, allowing a better resolution in the reconstruction of direction ($\sim$1 arcmin) [25].

The GBM-LAT combination thus provides burst spectra over seven decades in energy and has made several important discoveries regarding GRBs, in particular about their prompt spectra. In most cases they consist of one peak and power law functions with different indices at low and high energies with a smooth transition from one to the other (the so-called *Band spectrum*); in a few cases there is an additional non-thermal component that can be fit as a power law extending to high energies [128]. For more details see Section 2.2.1.

2.2 Observational properties of GRB prompt radiation

The prompt emission lasts typically a few seconds (or less), without repetition and with variable light curve. Furthermore, the spectra vary from burst to burst

and do not show any clear feature that could easily be associated with any simple emission model. Observationally, the prompt emission phase of a GRB is defined as a temporal phase during which sub-MeV emission is observed by GRBs detectors above the background level.

In this Section the basic features of GRB prompt emission will be treated.

2.2.1   Spectral properties

GRBs are characterized by emission in the few hundred keV range with a non-thermal spectrum, which can be fit with a smoothly-joined broken power law known as *Band function*, introduced by Band et al. [29]:

$$N(E) = \begin{cases} A \left(\frac{E}{100 \text{ keV}}\right)^{\alpha} \exp(-\frac{E}{E_0}), & E < (\alpha - \beta)E_0 \\ A \left[\frac{(\alpha - \beta)E_0}{100 \text{ keV}}\right]^{\alpha - \beta} \exp(\beta - \alpha) \left(\frac{E}{100 \text{ keV}}\right)^{\beta}, & E \geq (\alpha - \beta)E_0 \end{cases}, \qquad (2.1)$$

in which A is a normalization constant, $N(E)$ is the number of photons detected, α and β (both negative) are the photon spectral indices below and above the break energy E_0, respectively. The lower energy spectral index has generally a value $\alpha \sim -1$, the high-energy one instead $\beta \sim -2$. In the following, the flux particle F_ν is referred to $EN(E)$ while the SED to $E^2 N(E)$ or νF_ν. For most observed values of α and β the SED peaks at $E_p = (\alpha + 2)E_0$, called *E-peak*, which represents the typical energy of the observed radiation. The E_p distribution is wide and extends from several keV to the MeV range. An example of Band-function spectrum is shown in Figure 2.5.
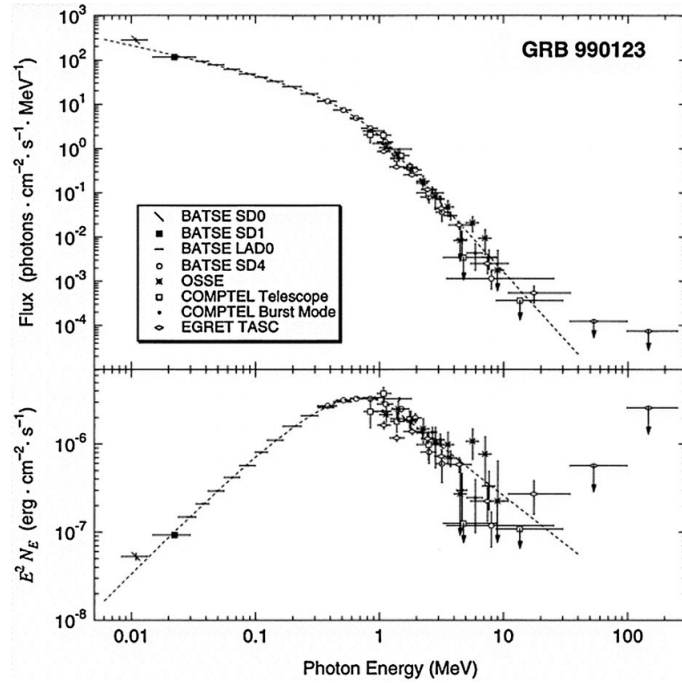
Figure 2.5.   The Band function spectrum of GRB 990123. $E_p = 720 \pm 10$ keV, $\alpha = -0.6 \pm 0.07$, $\beta = -3.11 \pm 0.07$. Figure from [41].

Some spectra can be fitted with a simpler function, a cutoff power law spectrum in the form:

$$N(E) = A \left(\frac{E}{100 \text{ keV}} \right)^{-\alpha} \exp \left(-\frac{E}{E_c} \right),$$ (2.2)

that is essentially the first portion of the Band function 2.1. In this expression E_c characterize the cut-off in the energy spectrum. This function has been used to fit the prompt spectrum of many GRBs (e.g. Fermi-GBM spectra [101]), mainly because of the narrow bandpass of the detectors, so that β could not be well constrained. When the spectrum is observed simultaneously by several instruments it is possible to obtain the global spectrum, and possibly it still comply with a Band function. However, GRB spectra measurements have evolved considerably from Band function in the years. Extra-components have been introduced: e.g. high-energy power law of exponentially attenuated power law [65] and photospheric component [110].

2.2.2 Temporal properties

The duration of a GRB is estimated through the so-called T_{90}, the time interval between the moment in which the 5% and the 95% of the fluence[2] are released. It typically ranges from millisecond to thousands of seconds and allows to define two different GRB types [84]; in fact, the T_{90} distribution of GRBs detected by BATSE on board CGRO, shown in Figure 2.6, includes two components with a separation visible around 2 s:

- Short-GRBs: burst duration peaked at 0.3 s, probably result of mergers of compact objects in binary systems (e.g two neutron stars or a neutron star and a black hole) [92].

- Long-GRBs: burst duration from ~ 2 s to many minutes, peaked at 30 s. These are associated with massive stars collapsing and generating supernova explosions [92].

The GRB separation into two classes is related to the "hardness ratio", that is the ratio between the photon numbers in the detector's low-energy and high-energy bands. Long GRBs in most of the cases have a "softer" spectrum than short ones, because in the first case the hardness ratio is larger than in the second one. However, T_{90} has some limitations, because it is a quantity defined by observations:

- It is energy-band-dependent and sensitivity-dependent; a detector with a lower energy bandpass typically gets a longer T_{90} for the same GRB and a more sensitive detector would detect a longer duration of a same burst along the background level.

- It can overestimate the duration of GRB central engine activity; it is the case of GRBs with clearly separated emission episodes with long quiescent gaps in between.

---

[2]The total (time-integrated) radiant energy per unit area within the detector energy range.
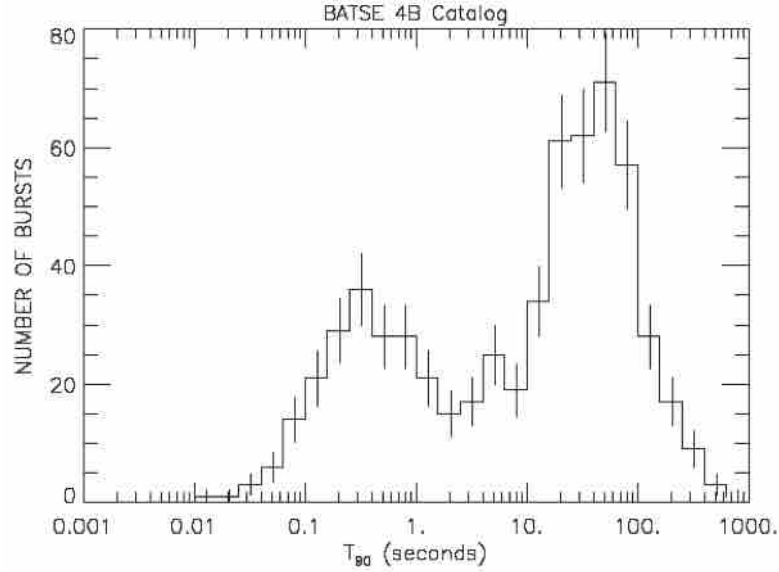
Figure 2.6. T_{90} distribution of the 4B Catalog Gamma-Ray Bursts recorded with BATSE. The result is a bimodal distribution, which reflects the existence of two GRBs population: long and short GRBs span T_{90} durations greater and less than ~ 2 s, respectively. Figure from https://gammaray.nsstc.nasa.gov/batse/grb/duration/.

Time scales - Observations

To date, there is a great variety of GRB light curves. Most of them are variable, while other are smooth with relatively simple temporal structures. One sample of GRB light curves is shown in Figure 2.7. By analyzing a light curve one can define two quantities:

- The variability time scale δt, which is determined by the width of the peaks in a light curve. It can be of the order of milliseconds for extremely variable GRBs.

- The pulse separation Δt. When this quantity is large, the distance between the two neighboring peaks is classified as a *quiescent period*, a relatively long period of several dozen of seconds with no activity.

Both their distributions follow log-normal ones (see e.g. [100]). By studying δt and Δt distributions one can obtain important information about the central engine activity; this topic will be better discussed in Chapter 4.

The considerations made up to now are valid for long GRBs; the variability of short ones is more difficult to analyze. Indeed, the duration of these bursts is closer to the limiting temporal resolution of the detectors.

Time scales - Theory

General kinematic considerations impose constraints on the temporal structure produced when the energy of a relativistic shell is converted to radiation [105].
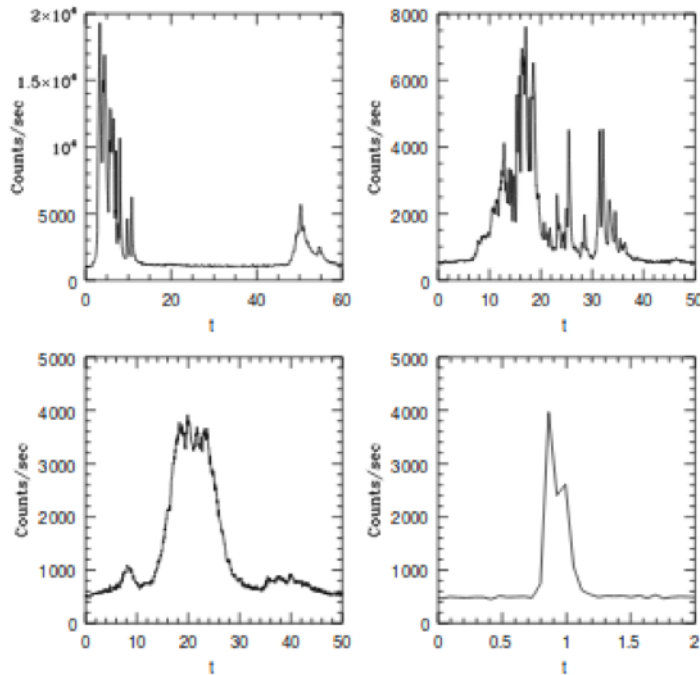
Figure 2.7. Examples of GRB light curves detected by BATSE. Figure from [103].

Consider a spherical relativistic emitting shell with a radius R_e, a width Δ and a Lorentz factor $\gamma \equiv \Gamma$, referring to the Figure 2.8. Photons emitted in point A move directly towards the observer and arrive first after a time $t_{\rm rad}$; if they are emitted moving at an angle Γ^{-1} (point D) they will arrive after $t_{\rm ang} = R_e/2c\Gamma^2$ [3]. This time might possibly coincide with the arrival time of photons emitted in point C, directly towards the observer but at a radius $2R_e$. So, in this case, $t_{\rm ang} \approx t_{\rm rad}$. This suggests that variable GRBs cannot be produced from a single explosion. Other time scales are determined by the flow of relativistic particles. First of all, the intrinsic duration $T_\Delta = \Delta/c$, which is the time in which the source that produces the relativistic flow is active; photons emitted at the front of a such shell will reach the observer at time T_Δ before those emitted from the rear (point B). Secondly there is the intrinsic variability δt , which is the time scale on which the inner source varies and produces a subsequent variability with a lenght scale $\delta = c\delta t$ in the flow. Naturally δt sets a lower limit to the variability time scale observed in any burst.
These timescales divide light curves into two classes:

- $T_\Delta \leq t_{\rm ang} \approx t_{\rm rad}$: the resulting burst is smooth with a width $t_{\rm ang} \approx t_{\rm rad}$. This is the case of external shocks, i.e. when shells interact with the interstellar medium [111], then external shocks can produce only smooth bursts.

- $T_\Delta > t_{\rm ang}$: a variable light curve is produced. This can be easily satisfied in the internal shock model (see Section 2.3.1).

---

[3]This delay is relevant only if the angular width of the emitting region in larger than Γ^{-1}.
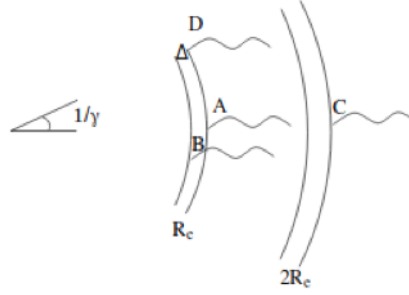
Figure 2.8. Different time scales from a relativistic expanding shell in terms of the arrival times of various photons: the angular time scale $t_{\text{ang}} = t_D - t_A$, the radial time scale $t_{\text{rad}} = t_C - t_A$ and the intrinsic duration of the flow $T_\Delta = t_B - t_A$. Figure from [105].

2.3 GRB fireball model

The so-called *fireball model* is the basic model proposed to explain the first observations of GRBs [66] [102]. It consists into a matter-dominated fireball, made of baryons (primarily protons and neutrons), electron-positron (e^+e^-) pairs, and photons, created after the collapse of massive stars (long GRBs) or after the merging of binary objects (short GRBs).
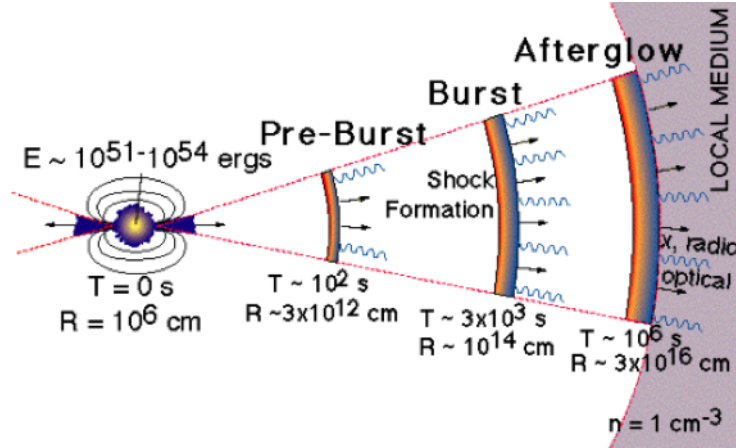
Figure 2.9. Cartoon for the GRB fireball model. Figure from [63].

As shown in Figure 2.9, a high amount of energy is released by the central engine and a relativistic outflow is formed by parts of this energy. This outflow is accelerated and part of its kinetic energy is dissipated through the prompt emission mechanism (generated by internal shocks between slow and fast parts of the ejecta), leading to the observed γ-ray emission.

The sudden release of a large amount of γ-ray photons leads via e^+e^- pair creation to an opaque radiation plasma. The energy in radiation is initially larger than in baryons by a factor of about 10^2, and as the fireball expands adiabatically, baryons get accelerated to a high Lorentz factor, then to relativistic velocities [112]. The kinetic energy of the outflow is converted back to thermal energy and radiated

away as γ-rays photons at some large distances from the place where the fireball is produced (e.g. [107]). When the baryon kinetic energy becomes comparable to the total fireball energy, the acceleration stops. The matter-dominated fireball continue to expand and becomes more and more transparent to radiation, so the jet now is optically thin. In this phase, parts of the kinetic energy are dissipated by the prompt emission and the subsequent radiation is detected as the non-thermal prompt emission. When the created jet reaches the circumburst medium external shocks create the afterglow and the jet is finally decelerated. The remaining kinetic energy powers the observed multiwavelenght afterglow.

However, the exact energy dissipation and emission mechanism is still under debate and is closely connected to the nature of the ejecta itself.

The compactness problem and relativistic motion

Now it is known that the GRB central engine emits ultra-relativistic jets but at the beginning of GRB studies it was not trivial to understand it. The relativistic motion in these objects, in fact, was rising the so-called *compactness problem.*

The optical depth of the process $\gamma + \gamma \rightarrow e^+ e^-$ is given by $\tau_{\gamma\gamma} \propto \mathcal{L}/R$, where $\mathcal{L}$ is the luminosity and R the size of the emitting region. A simple estimate of the size of the source ($R = c\delta t$, as implied by the observed variability, where δt is of the order of milliseconds) shows that the source must be extremely optically thick to $e^+ e^-$ pair creation. Such a source cannot provide the observed non-thermal gamma-ray emission. The solution of this paradox is hidden in the relativistic motion for two reasons:

1. The size of the emitting region becomes now $R = c\Gamma^2\delta t$, where Γ is the average Lorentz factor of the jet.

2. The rest frame energy of the photons is smaller by a factor of Γ; therefore, only a smaller fraction of them can create pairs.

If $\Gamma > 100$, the pair creation optical depth would be reduced below 1 and high-energy photons would be able to escape the fireball.

The potential of relativistic motion to resolve the compactness problem was realized, among other scientists, in the eighties by Goodman [67] and Paczýnski [102].

2.3.1 GRB prompt emission models

Internal Shock Toy Model

A widely used model to describe the activity of the inner engine is the so-called *internal shocks model* (IS). In this scenario, the source produces multiple shells with different Lorentz factors over a time $T_\Delta = \Delta/c$, where Δ is now the overall width of the flow in the observer frame (see Figure 2.10). Faster shells will catch up with slower ones and will collide, converting some of their kinetic energy to internal
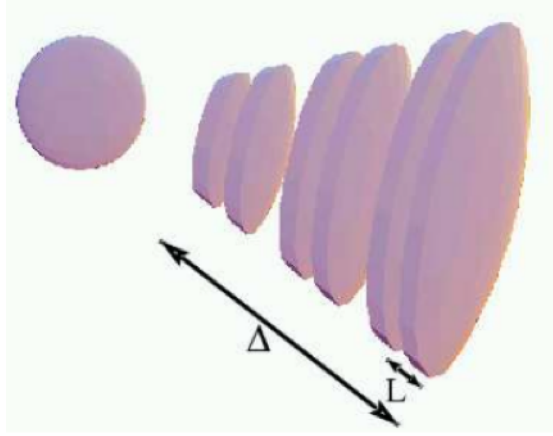
Figure 2.10. The internal shock model. Figure from [105].

energy [103]. The source is variable on a scale L/c, where L is the distance between two adjacent shells, then the observed variability time scale in the light curve, δt, reflects the variability of the source. The characteristic radius where the shell starts to collide is $R_{\text{coll}} \approx L\Gamma^2$ and continue as long as the source is active, within the duration time T_Δ, reflecting the overall duration of the activity of the inner engine.

In the following, the shell collision process is considered. For semplicity, we assume two shells of masses m_1 and m_2 ejected from the central engine with Lorentz factors Γ_1 and Γ_2, respectively. The slower shell is launched from the source δt time before a faster shell. When the latter reaches the first one, they collide forming one single shell distant from the center $R_{\text{coll}} \approx 2c\Gamma_1^2\delta t$, when $\Gamma_2 \gtrsim 2\Gamma_1$. Therefore, the radiation produced in this collision arrives at the observer at time:

$$t_{\text{obs}} \sim t_0 + \frac{R_{\text{coll}}}{2c\Gamma_f^2} \sim t_0 + \delta t\frac{\Gamma_1}{\Gamma_2}, \tag{2.3}$$

where t_0 is the time when the faster shell was ejected from the central engine, Γ_f is the final Lorentz factor of merged shells, given by:

$$\Gamma_f = \frac{m_1\Gamma_1 + m_2\Gamma_2}{(m_1^2 + m_2^2 + 2m_1m_2\Gamma_r)^{1/2}}, \tag{2.4}$$

where Γ_r is the relative Lorentz factor of the two shells before collision. From Equation 2.3 it is clear that the variability time of GRB light curves roughly tracks the engine variability time (assuming that Γ_2/Γ_1 does not change during the engine activity). Therefore, the internal shocks model can explain the observed short time scale variability by linking it to the central engine time scale.

In the internal shock scenario it is expected that particle acceleration happens at the shock created in the collisions between shells. The radiation emitted by accelerated particles forms the prompt non-thermal spectrum, which is generally

explained by the synchrotron emission[4] or by Inverse Compton (IC)[5].
The internal shock model, however, does not dissipate efficiently the shock kinetic energy, because of the intrinsic relativistic nature of the shock itself. In fact, defining the efficiency as the total GRB energy divided by the radiated energy (also including the afterglow) one would expect an high efficiency ($\geq 50\%$) [78]. Only a fraction of the thermal energy produced in collisions is likely deposited in electrons, the rest is taken up by protons and magnetic fields [87] and the synchrotron and the IC power losses for a proton are smaller than for an electron. A high efficiency in γ-rays production requires a large dispersion in the Lorentz factor of the outflows [31], that in turn makes difficult to accomodate some observed spectral relations [78].

Photospheric model

The *photospheric model* (PH) is often address to explain thermal photons observed in GRB spectra. While in the internal shock model all radiation emission is produced in the optically thin regime, the photospheric scenario assumes the emission to be released at the photosphere itself. However, the spectrum that it produces tends to be thermal without non-thermal tails observed in GRBs [78]. It is reasonable to think that in GRBs both models coexist, also because, assuming that the photospheric model is the only valid, one would not be able to observe γ-rays; the radiation, in fact, would be released in a region where the flow is optically thick, hence photons would not escape the fireball.
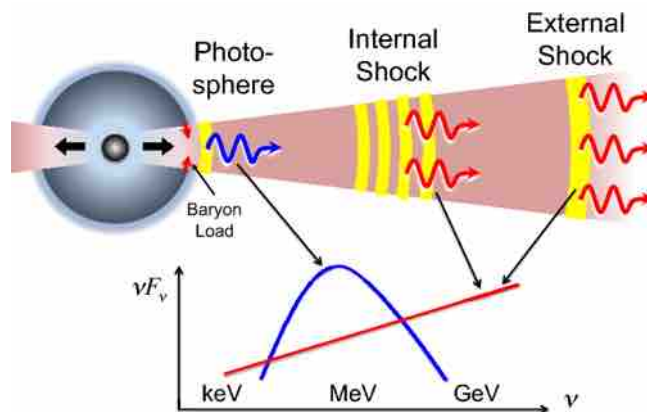
Figure 2.11. Photospheric-internal-external shock model. The photospheric emission produces the Band spectrum, the internal shock contributes to the variable power law spectrum, and the external shock makes the long-lived power law spectrum. Figure from [78].

This scenario can explain sub-dominant thermal features measured for some burst detected by *Fermi* satellite [118].

---

[4]Non-thermal radiation generated by charged particles (usually electrons) spiralling around magnetic field lines at close to the speed of light. Since the electrons are always changing direction, they are in effect accelerating and emitting photons with frequencies determined by the speed of the electron at that instant.

[5] Scattering of low energy photons to high energies by ultrarelativistic electrons so that the photons gain and the electrons lose energy.

In Figure 2.11 the photospheric-internal-external shock model and corresponding energies affected in the radiation spectrum are shown. See the recent review [32] for new developments of this model.

2.4   High energy neutrinos from GRBs

Both the internal shock and the photospheric models assume that shocks take place when faster shells of plasma emitted by the central engine collide with the slower ones, producing gamma rays. This mechanism dissipates a large fraction of the kinetic energy of the flow, provided that the central engine is highly variable. The dissipated energy is partly transferred to accelerated particles, namely electrons and protons, which then assume ultra-relativistic speed. At this point accelerated electrons radiate a fraction of their energy through synchrotron and inverse Compton processes, creating a radiation field that possibly allows the $p\gamma$ resonant Δ^+ production, and the subsequent decay chain:

$$p + \gamma \xrightarrow{\Delta^+} \begin{cases} p + \pi^0 \\ n + \pi^+ \end{cases} \rightarrow \begin{cases} \pi^0 \rightarrow \gamma + \gamma \\ n \rightarrow p + e^- + \bar{\nu}_e \\ \pi^+ \rightarrow \mu^+ + \nu_\mu \\ \mu^+ \rightarrow e^+ + \nu_e + \bar{\nu}_\mu \end{cases} \qquad (2.5)$$
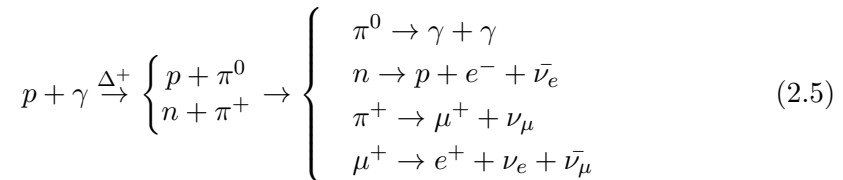
Protons of energy $E_p \sim 10^{15}$ eV interact with keV-MeV photons forming Δ^+ resonance ($m_{\Delta^+} = 1232$ MeV/c^2) which decays into pions, forming neutrinos with $E_\nu \sim 10^{14}$ eV. Therefore, assuming that the proton load (the fraction of protons in the flux of accelerated particles) is not negligible, GRBs are believed to be important high-energy neutrino producers. About 20% of the proton energy goes to π^+ ($E_{\pi^+} \sim 0.2E_p$), whose energy is evenly distributed to 4 leptons ($E_\nu \sim 0.25E_{\pi^+}$); so overall $E_\nu \sim 0.05E_p$ [87]. Due to the high compactness of the ejecta, the $p\gamma$ interaction can have high optical depth, so that π^+ are copiously generated. These latter decay in μ^+, which subsequently decay generating neutrinos (ν_μ and ν_e) and anti-neutrinos ($\bar{\nu}_\mu$).

The mechanism indicated in 2.5 can take place in both the PH and IS models, but the difference lies in the distance from the central engine in which the main collision occurs, as it affects the energies involved in the collision. The standard model invokes internal shocks as the site of both γ-ray photon emission and proton acceleration; alternatively, in the photospheric model photons can be generated at the photosphere and protons can be accelerated in the same site [87]. Therefore, in this latter case the emitted neutrino energy will be lower than that in the internal shock model; the emission of neutrinos, in fact, takes place before the particles undergo further acceleration from the collision between different shock fronts. In fact, the neutrino production efficiency is different in the two cases. The optical depth $\tau_{p\gamma}$ of $p\gamma$ interaction is [121] [126]:

$$\tau_{p\gamma} = 0.8 \left(\frac{R}{10^{14} \text{ cm}}\right)^{-1} \left(\frac{\Gamma}{10^{2.5}}\right)^{-2} \left(\frac{E_\gamma}{1 \text{ MeV}}\right)^{-1} \left(\frac{L_{\text{iso}}}{10^{52} \text{ erg s}^{-1}}\right), \qquad (2.6)$$

where R is the distance between the central engine and the neutrino production site (fireball radius), L_{iso} is the isotropic γ-ray luminosity of the burst and E_γ is the

energy at which the γ-ray spectrum has a break ($\sim$ 100 keV). In the IS scenario R depends on the variability time t_{var}, the Lorentz factor Γ and the redshift z, and it is given by [27]:

$$R_{\mathrm{IS}} \sim 10^{13} \left(\frac{t_{\mathrm{var}}}{0.01 \text{ s}} \right) \left(\frac{\Gamma}{10^{2.5}} \right)^2 \left(\frac{1 + 2.15}{1 + z} \right) \text{ cm,} \qquad (2.7)$$

while in the PH scenario is [127]:

$$R_{\mathrm{PH}} \sim 10^{11} \left(\frac{\Gamma}{10^{2.5}} \right)^{-2} \left(\frac{L_{\mathrm{iso}}}{10^{52} \text{ erg s}^{-1}} \right) \text{ cm.} \qquad (2.8)$$

For characteristic values of GRB parameters $R_{\mathrm{PH}} < R_{\mathrm{IS}}$, then $\tau_{p\gamma}$ in the PH model is enhanced by a factor $R_{\mathrm{IS}}/R_{\mathrm{PH}}$ compared to the IS model. This result suggests that the neutrino production is more efficient in a dissipative photosphere than in standard ISs [20].

In hadronic GRB models, neutrinos are produced from the interaction between the accelerated protons and the jet radiation field. Accelerated protons are expected to be distributed according to a differential energy spectrum in the form indicated by Equation 1.8 with $(1 + s) = 2$. Convolving such a spectrum with the spectrum of the target radiation field, one generally expects for the neutrino energy distribution a power law spectrum with an energy break regulated by the break in the synchrotron spectrum of target photons. The first calculation of the prompt neutrino flux was realized by Waxman & Bahcall (1997) [121], which used average GRB parameters and the GRB rate measured by BATSE to determine an all-sky diffuse neutrino flux contributed by the GRB population. In this work another general formalism that can be applied to any of the above mentioned models for GRB emission is presented. It was calculated by Abbasi et al. (2010) [10], following Guetta et al. (2014) [69], which is in turn based on Waxman & Bahcall (1997) [121]. For an observed "Band" function photon flux spectrum

$$F_\gamma(E_\gamma) = \frac{\mathrm{d}N(E_\gamma)}{\mathrm{d}E_\gamma} = f_\gamma \begin{cases} \left(\frac{\epsilon_\gamma}{\text{MeV}} \right)^\alpha \left(\frac{E_\gamma}{\text{MeV}} \right)^{-\alpha}, E_\gamma < \epsilon_\gamma \\ \left(\frac{\epsilon_\gamma}{\text{MeV}} \right)^\beta \left(\frac{E_\gamma}{\text{MeV}} \right)^{-\beta}, E_\gamma \geq \epsilon_\gamma \end{cases} \qquad (2.9)$$

where ϵ_γ is the break energy, α and β are the spectra index before and after the break energy, respectively, and f_γ is the normalization, the observed neutrino number spectrum can be expressed as:

$$F_\nu(E_\nu) = \frac{\mathrm{d}N(E_\nu)}{\mathrm{d}E_\nu} = f_\nu \begin{cases} \left(\frac{\epsilon_{\nu,1}}{\text{GeV}} \right)^{\alpha_\nu} \left(\frac{E_\nu}{\text{GeV}} \right)^{-\alpha_\nu}, & E_\nu < \epsilon_{\nu,1} \\ \left(\frac{\epsilon_{\nu,1}}{\text{GeV}} \right)^{\beta_\nu} \left(\frac{E_\nu}{\text{GeV}} \right)^{-\beta_\nu}, & \epsilon_{\nu,1} \leq E_\nu < \epsilon_{\nu,2} \\ \left(\frac{\epsilon_{\nu,1}}{\text{GeV}} \right)^{\beta_\nu} \left(\frac{\epsilon_{\nu,2}}{\text{GeV}} \right)^{\gamma_\nu - \beta_\nu} \left(\frac{E_\nu}{\text{GeV}} \right)^{-\gamma_\nu}, & E_\nu \geq \epsilon_{\nu,2} \end{cases}$$

$$(2.10)$$

where $\alpha_\nu = p + 1 - \beta$, $\beta_\nu = p + 1 - \alpha_\nu$ and $\gamma_\nu = \beta_\nu + 2$; $p = 1 + s$ is the photon spectral index defined by $N(E_p)dE_p \propto E_p^{-p}dE_p$. The indices α_ν and β_ν are derived by assuming that the neutrino flux is proportional to the $p\gamma$ optical depth $\tau_{p\gamma}$. This is valid when the fraction of proton energy that goes to pion production is proportional

to $\tau_{p\gamma}$, which is roughly valid when $\tau_{p\gamma} < 3$ [87]. Two breaks, $\epsilon_{\nu,1}$ and $\epsilon_{\nu,2}$, modify the simple power law behavior of neutrino energy distribution: $\epsilon_{\nu,1}$ reflects the break in the photon spectrum due to energy losses of accelerated electrons, $\epsilon_{\nu,2}$ is due to the synchrotron losses from secondary mesons. For more details about equations and parameters used in the calculation of the neutrino spectra see [10].
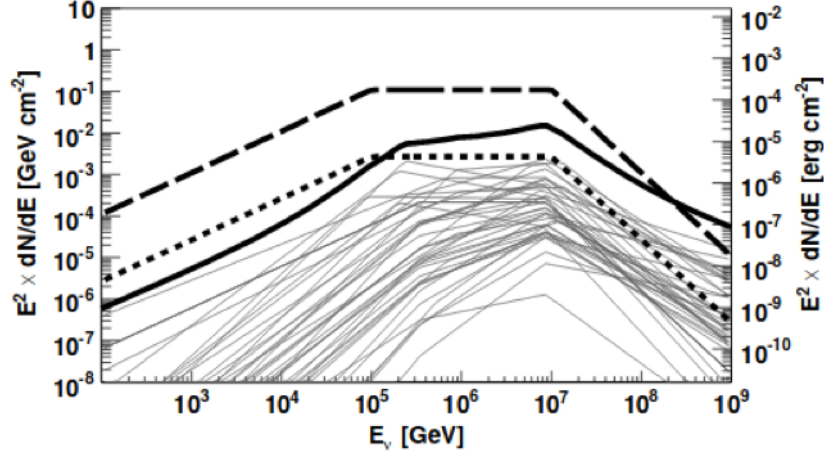
Figure 2.12. Calculated neutrino spectra in [10] for 41 GRBs (thin solid lines) compared to the standard Waxman-Bahcall spectrum [121] (thick dotted line). The sum of all individual spectra (thick solid line) and the sum of Waxman-Bahcall spectra (thick dashed line) are also shown.

Why is the neutrino detection important?

Searching a temporal and spatial coincidence among the GRB prompt emission and high-energy neutrinos, by using neutrino telescopes like ANTARES and IceCube (see Chapter 3), is very relevant because it provides information about the acceleration mechanisms in GRBs. The detection of a single neutrino event would allow to identify these sources as extreme hadronic accelerators, and hence as candidates for UHECRs [39] (see Chapter 1).

Neutrinos are ideal candidates in the search for distant astrophysical objects because they are electrically neutral, stable and weakly interacting particles. Thus, unlike protons or gamma rays, neutrinos are not diverted in their path from their source to the Earth. Among all the possible astrophysical sources, GRBs, being transients and extremely energetic explosions in a short time, offer one of the most promising perspectives for the detection of cosmic neutrinos thanks to the almost background free search. Over the years, the IceCube and ANTARES Collaborations have been searching for neutrino signals coincident with GRBs in time and direction, which however have not observed until now. Progressively deeper non-detection upper limits have been placed and current limits do not yet provide significant constraints on the validity of the internal shock model. However, the model would be severely challenged if the upper limit reduces in the next few years: the jet barionic content would then be severely constrained. Alternative scenarios, like magnetic dissipation

models, that invoke a large emission radius (e.g. the ICMART model [125]) and predict a much lower neutrino flux, and the leptonic model (e.g. [24]), for which non-thermal lepton synchrotron radiation occurs, could be favorites.

Chapter 3

Neutrino Telescopes

The idea of a neutrino telescope, based on the detection of secondary particles produced in neutrino interactions, was first formulated in the 1960s by Markov [98], who proposed *to install detectors deep in a lake or in the sea and to determine the direction of the charged particles with the help of the Cherenkov radiation.* The advantages of neutrinos as cosmic messengers, already explained in the previous Chapter in Section 2.4, have led to the development of several neutrino telescopes with different size and capabilities. The currently operational detectors will be discussed in this chapter.

3.1 Neutrino detection principle

The basic idea for a neutrino telescope is to build a matrix of light detectors inside a transparent medium. This medium, such as deep ice or water, should have the following characteristics:

- offers large volume of free ad natural target for neutrino interactions;

- provides shielding against secondary atmospheric particles produced by cosmic rays;

- allows transmission of Cherenkov photons induced by the path of relativistic particles produced by the neutrino interaction.

Neutrinos are not observed directly, but when they happen to interact with the ice or water they produce electrically charged secondary particles that in turn emit Cherenkov light (see Section 3.2), as a result of traveling through the ice faster than light travels in the medium. A detector must measure with high precision the number and arrival time of these photons on a three-dimensional array of Photo Multiplier Tubes (PMTs), from which some of the properties of the neutrino (flavor, direction, energy) can eventually be inferred.

In the framework of the Standard Model, high energy neutrinos interact with a nucleon N of the nucleus, via either charged current (CC) weak interactions

$$\nu_l + N \rightarrow l + X, \tag{3.1}$$

or neutral current (NC) weak interactions

$$\nu_l + N \rightarrow \nu_l + X, \tag{3.2}$$

where l indicates the leptonic flavor ($l = e,\mu,\tau$) and X the hadronic cascade originated in the interaction. A schematic view of different kind of neutrino interactions is shown in Figure 3.1. In the proposed Cherenkov neutrino telescope no magnetic
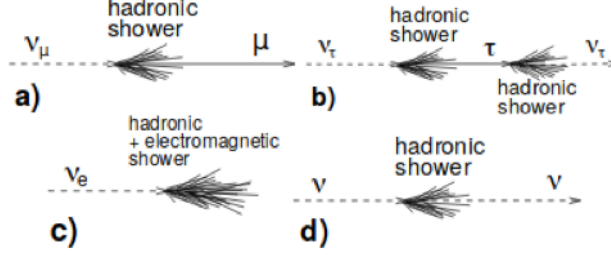
Figure 3.1. Some event signature topologies for different neutrino flavors and interactions: a) CC interaction of a ν_μ produces a muon and a hadronic shower; b) CC interaction of a ν_τ produces a τ that decays into pions and ν_τ, tracing the double bang signature; c) CC interaction of ν_e produces both an electromagnetic (EM) and a hadronic shower; d) a NC interaction produces an undetectable diffuse neutrino and a hadronic shower. Figure from [47].

field can be used to reconstruct the sign of the primary leptons, so no separation between particles and anti-particles can be made. The only channel which might possibly provide indications on the interacting weak neutrino flavor consists into the Glashow resonance, where a $\bar{\nu}_e$ can resonantly produce the W^- boson[1], at $E_\nu = 6.3$ PeV.

At energies of interest for neutrino astronomy ($E_\nu > 100$ GeV) the interaction process proceeds in the deep inelastic scattering regime. The leading order differential cross section for the CC interactions in 3.1 is given by [60]:

$$\frac{d^2\sigma_\nu N}{dxdy} = \frac{2G_F^2 m_N E_\nu}{\pi} \frac{M_W^4}{(Q^2 + M_W^2)^2}[xq(x, Q^2) + x(1 - y)^2 \bar{q}(x, Q^2)], \tag{3.3}$$

where Q^2 is the square of the momentum transferred between the neutrino and the lepton, m_N is the nucleon mass, M_W is the mass of the W boson, and G_F is the Fermi coupling constant. The functions $q(x, Q^2)$ and $\bar{q}(x, Q^2)$ are the parton distribution[2] for quarks and anti-quarks, $x = Q^2/2m_N(E_\nu - E_l)$ and $y = (E_\nu - E_l)/E_\nu$ are the so-called scaling variables or Feynman-Bjorken variables[3]. Figure 3.2 shows the ν_μ and $\bar{\nu}_\mu$ cross sections as a function of the neutrino energy. For 10^{15} eV $\leq E_\nu \leq 10^{21}$ eV a simple power law form is a good representation of the cross sections trend: at lower

---

[1]The W boson is a fundamental particle which, together with the Z boson, mediates the charged and neutral current weak interactions.

[2]Partons were proposed by Feynman as point-like constituents of hadrons, before quarks and gluons were generally accepted [53].

[3]Lorentz invariant kinematic variables proposed by Bjorken (1969) [38] for electron-nucleon deep inelastic scattering.
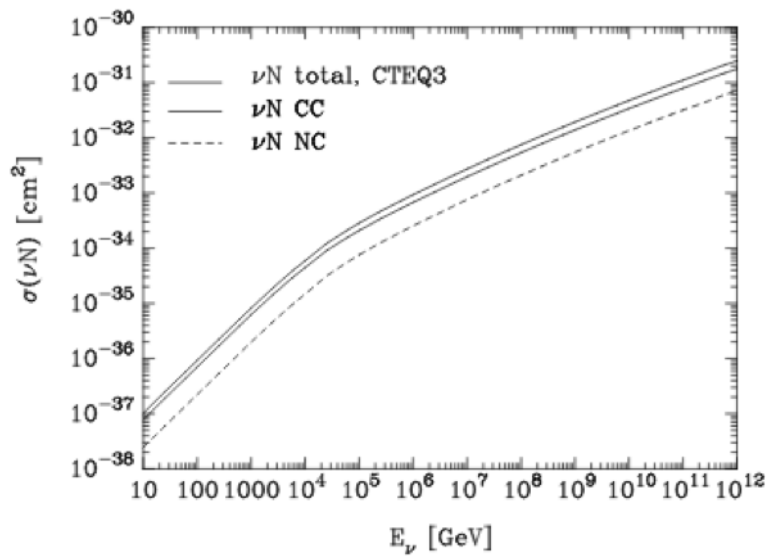
Figure 3.2. Cross sections for CC (thin line) and NC (dotted line) neutrino interactions at
high energies. The total cross section, determined by the CTEQ collaboration [91], is
also indicated (thick line). Figure from [60].

energy the neutrino cross section rises linearly with E_ν up to $\sim 10^4$ GeV, while after
this value it grows more slowly.

In a high energy neutrino detector one can distinguish between two main event
signatures linear-shaped: events (tracks), and spherical-shaped events (showers).
Indeed, if the *path length*[4] of the particle exceeds the spatial resolution of the detector,
the trajectory of the particle can be resolved and a track is sperimentally observed.
Moreover, as Figure 3.1 shows, showers occur in all interactions. However, for CC
ν_μ, often only the muon track is detected, as the path length of a muon in water
exceeds that of a shower by more than 3 orders of magnitude for energies above 2
TeV (at this energy the muon path in water is about 1 km). Therefore, such a very
high energy CC events might very well be detected even if the interaction has taken
place several km outside the instrumented volume, provided that the muon reaches
and traverses the detector. High-energy tracks extend the effective volume of the
detector by far with respect to the merely instrumented volume.

Cosmic neutrino detectors are not background free. Showers induced by interactions
of CRs with the Earth atmosphere produce the so-called *atmospheric muons* and
atmospheric neutrinos. Figure 3.3 shows that below the horizon ($\cos(\theta) < 0$, where
θ is the zenith angle), from which up-going tracks come, the Earth filters all cosmic
ray products except neutrinos. In the sample of tracks coming from above the
horizon ($\cos(\theta) \gtrsim 0$) high energy down-going atmospheric muons constitute the
main background. These muons can penetrate several kilometers of water or ice and
their flux exceeds that induced by atmospheric neutrino interactions by many order
of magnitude, decreasing with increasing detector depth. For this reason neutrino
detectors must be located deeply under a large amount of shielding matter in order

---

[4]Mean lenght of the distance traveled through the medium by a charged particle after decaying
or interacting with it.
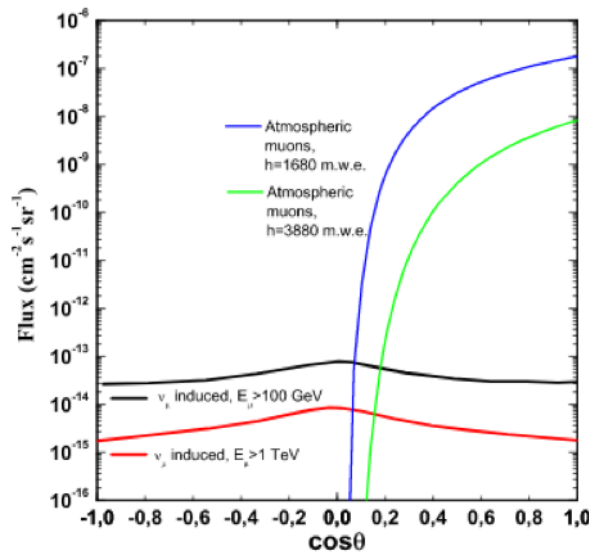
Figure 3.3. Different contributions (flux as a function of the cosine of the zenith angle) of the atmospheric muons (blue line for a depth of 1680 m and green line for a depth of 3880 m), and the atmospheric neutrino induced muons (black line for an energy threshold of 100 GeV and red line for an energy threshold of 1 TeV). Figure from [47].

to reduce this background component. The previous generation ef experiments which had looked also for astrophysical neutrinos (MACRO [21] and SuperKamiokande [13]) was located under mountains, and has reached almost the maximum possible size for underground detectors. Another background component, for the search of neutrino from astrophysical sources, is given by *up-going muons* produced by interactions of up-going atmospheric neutrinos. Collecting only the events classified as "up-going" the atmospheric neutrinos that have traversed the Earth, represent the irreducible background for the study of cosmic neutrinos. The rejection of this background depends upon the pointing capability of the telescope. A further signal to background discrimation is provided by the energy distribution of this two samples. The expected cosmic neutrino energy spectrum is quite "hard", possibly described by a power law like $E^{-\gamma}$ where $2.0 < \gamma < 2.4$, while the high energy part of atmospheric neutrinos has a much steeper energy spectrum ($\gamma \sim 3.7$), as a result of the CR spectrum generating them. This implies that the detector should also allow a quite good energy measurement of the parent neutrino energy.

The transmission probability, through the Earth, of neutrino fluxes $S(E_\nu, \theta)$ must be considered in the up-going neutrino search. It depends on the neutrino direction, as well as from energy and the total CC cross section $\sigma_C C(E_\nu)$, as [89]:

$$S(E_{\nu_{\mu,e}}, \theta) = \exp\left[-N_A \sigma_{CC}(E_{\nu_{\mu,e}}) \int \rho(\theta, \lambda) dl\right], \tag{3.4}$$

where N_A is the Avogadro number, $\rho(\theta, l)$ is the Earth density profile for a given direction θ and l is the distance traveled in the Earth by neutrinos. At energies $E > 10$ PeV the Earth becomes opaque to up-going neutrinos: therefore in this energy window, where the atmospheric background is very small, it is possible to observe only down-going events.

Muon neutrino detection

Muon neutrinos are especially interesting in a search for neutrinos from cosmic sources. They can do CC interaction (3.1) and produce muons that neutrino telescopes detect. If neutrinos have energies larger than ~ 1 TeV, ν_μ interactions can occur outside the detector volume, since in most cases muons are energetic enough to completely traverse the detector. This gives a clean experimental signal which allows an accurate reconstruction of the muon direction, closely correlated with the neutrino. In fact the average angle between the incident neutrino and the outgoing muon $\theta_{\nu\mu}$ decreases with increasing neutrino energy E_ν as:

$$\theta_{\nu\mu} \leq \frac{0.6°}{\sqrt{E_\nu \text{ (TeV)}}}. \tag{3.5}$$

Moreover, a muon traveling through ice or water is subject to multiple scattering, that causes deviations of the muon direction [124]: however, at the energies and distances here involved, this effect can be neglected. Muon direction can be measured with an intrinsic resolution which depends on many factors, and in particular on the propagation medium. From Monte Carlo simulations, the precision is of the order of less than 1° in ice, and $\sim 0.2°$ in water [47], the difference being connected with the larger scattering effects of ice.

3.2   Cherenkov effect

Cherenkov radiation is a result of a polarization effect induced by charged particles crossing an optically transparent medium with speed larger than that of light in that medium [46]. The charged particle polarizes the molecules along the particle trajectory, but only when the particle moves faster than the speed of light in the medium, an overall dipole moment is present. Light is emitted when the electrons of the medium restore themselves to equilibrium after the perturbation has passed, creating a coherent radiation on the surface of a cone with a characteristic angle θ_C given by:

$$\cos \theta_C = \frac{1}{\beta n}, \tag{3.6}$$

where n is the refracting index of the medium and β is the particle speed in units of c. The number of Cherenkov photons, N_γ, emitted per unit wavelength interval, $d\lambda$, and unit distance traveled, dx, by a charged particle of charge e is given by

$$\frac{d^2 N_\gamma}{dx d\lambda} = \frac{2\pi}{137\lambda^2} \left(1 - \frac{1}{n^2 \beta^2} \right), \tag{3.7}$$

where λ is the wavelength of the radiation. Shorter wavelengths contribute more significantly to the Cherenkov radiation. Light absorption by water or ice strongly suppresses some wavelengths (for details see [47]).
In Table 3.1 Cherenkov angle values, given by the Equation 3.6, are shown for water and ice, media of ANTARES and IceCube, respectively.
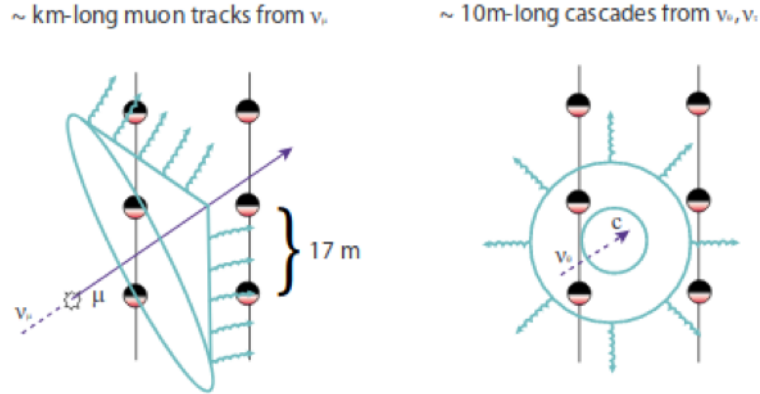
Figure 3.4. Cherenkov effect produced via CC weak interaction by a muonic neutrino ν_μ (left panel), which generates a muon track, and by an electronic neutrino ν_e (right panel), which produces a particle cascade. In the former case the Cherenkov radiation yields a well defined circular ring, in the latter one multiple cones and therefore a diffuse ring is produced. The signal is revealed by a three-dimensional array of Photo Multiplier Tubes (PMTs). Note that the distance between two close PMTs refers to IceCube (see 3.3.1). Figure from [71].

Medium	n	θ_C
Water	1.364	$\sim 43°$
Ice	1.33	$\sim 41°$

Table 3.1. Cherenkov angles for relativistic particles traveling in water and ice.

3.3 Neutrino telescopes

3.3.1 IceCube

Structure and data acquisition system

The IceCube Neutrino Observatory is a cubic-kilometer-scale high-energy neutrino detector built into the South Pole ice. It is the largest neutrino detector built to date and it was completed in 2011. It was designed specifically to detect neutrinos at TeV-PeV energies. It consists of a deep detector (*InIce*) and a surface detector (*IceTop*), as Figure 3.5 shows.

The design of the main InIce part of the detector consists of ~ 80 strings, buried at 1450 to 2450 m under the surface of the ice, each bearing 60 Digital Optical Modules (DOMs) with 17 m spacing (see Figure 3.4.). The strings are placed on a 125 m hexagonal grid, providing a 1 km^3 instrumented volume. The IceTop surface air-shower is an array of ~ 80 stations for the study of extensive air showers. Each IceTop station, located above an IceCube string, consists of two tanks filled with ice. Each of those tanks contains two DOMs of same design as the one used for the InIce part of the detector. The surface array, which covers an area of about 1 km^2, can be operated looking for anti-coincidence with the InIce events to reject down-going muons (see Section 3.1). It can also be used in coincidence, to provide a useful tool for cosmic rays composition study. The holes for the strings have been obtained
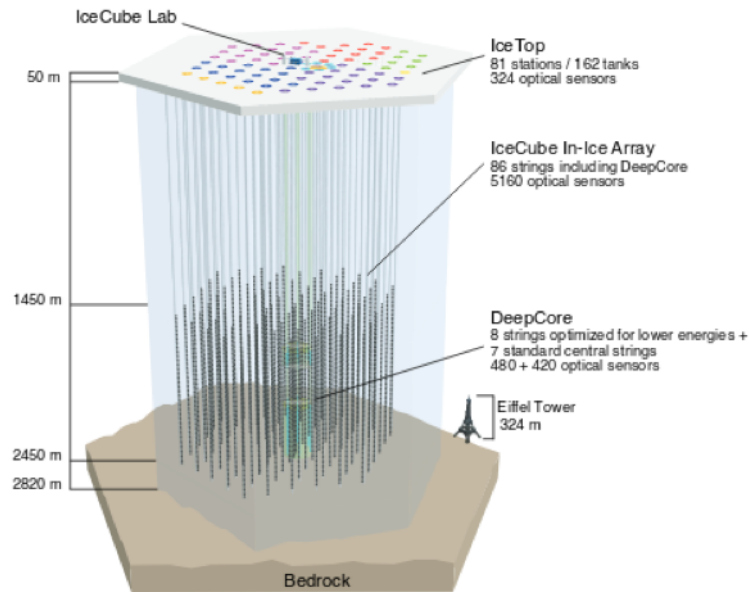
Figure 3.5. Artistic view of the IceCube Neutrino Observatory. Figure from [6].
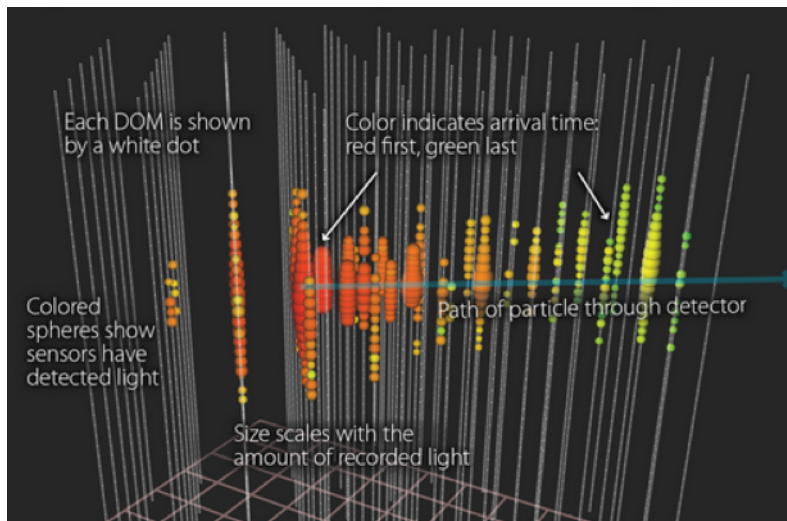
Figure 3.6. Event detected by IceCube on November 12, 2010. Duration: 3.8 μs; energy: 71.4 TeV; declination: $-0.4°$; right ascension: $110°$. Each DOM is shown by a white dot. Colors indicate arrival time: red first, green last. Colored spheres show sensors have detected light. Size scales with the amount of recorder light. The arrow shows the path of particle through detector. Figure from https://icecube.wisc.edu/science/icecube/detector.

with a jet of hot water, a stream of ~ 800 liters per minute of 88°C water. This water is propelled through a 1.8 cm diameter nozzle, melting a hole through the ice. Drilling a 2500 m deep, 60 cm diameter hole takes about 40 hours. Deploying a string of DOMs takes about another 12 hours.

Encapsulated in a glass pressure sphere to withstand the extreme pressure in the deep

ice, the main components of a DOM are a 10" PMT, a DC-DC high-voltage power supply, a light-emitting diode (LED) Flasher Board, and a Main Board containing the analog and digital processing circuitry for PMT pulses.

Photomultipliers transform the Cherenkov light from neutrino interaction into electrical signals using the photoelectric effect[5]. These signals are captured by a dedicated electronics card that digitize the shape of current pulses. The information, the occurrence time of the signal and its total charge, is sent, via cable, to the computers collecting the data. Interesting events (usually highly energetic ones) are sent by satellite to the IceCube data warehouse in Madison, WI. Essentially, IceCube consists of 5160 freely running sensors sending time-stamped, digitized waveforms of the light they detect to the surface. The local clocks in the sensors are kept calibrated with nanosecond precision. This information allows the scientists to reconstruct neutrino events and infer their arrival directions and energies. For a more detailed description of the experiment refer to the review of the observatory [71].

3.3.2   ANTARES

Detector and data tacking

The Astronomy with a Neutrino Telescope and Abyss environmental RESearch project (ANTARES) has been set up in 1996 and has been completed in May 2008, with the connection of its twelfth detector line [18]. This experiment is at present the largest neutrino observatory in the Northern hemisphere; it is located, in fact, in the Mediterranean Sea, anchored at a depth of about 2.475 m, 40 km off the coast of Toulon, France. It is designed to observe the Southern Hemisphere sky, as complement to IceCube. Indeed, this latter detects neutrinos from both hemispheres but the Southern sky is obscured by the large flux of cosmic ray muons [71] (see Figure 3.8). Analogously, ANTARES is prevented from observations of the Northern Sky because of the large atmospheric muon flux.

ANTARES consists of strings of photomultipliers, made of mechanically resistant electro-optical vertical cables anchored at the sea bed at distances of about 70 m one from each other, and tensioned by buoys at the top. In Figure 3.7 the principal component of the detector are indicated. Each string has 25 storeys, each of them contains three optical modules (OMs) and a local control module for the corresponding electronics. The OMs are arranged with the axis of the PMT 45° below the horizontal in order to optimize the view of the Southern sky. In the lower hemisphere there is an overlap in angular acceptance between modules, permitting an event trigger based on coincidences from this overlap.

Since lines are subject to the sea current and can change shape and orientation, on each string, and on the dedicated instrumented line, there are different sensors and instrumentation (LED beacons, hydrophones, compasses and tiltmeters) for timing and position calibration [15]. The first storey is about 100 m above the sea floor and the distance between adjacent storeys is 14.5 m. The instrumented volume corresponds to about 0.05 km^3.

The basic unit of the detector is the optical module, consisting of a photomultiplier

---

[5]Emission of electrons or other free carriers released from or within a material when it absorbs electromagnetic radiation.
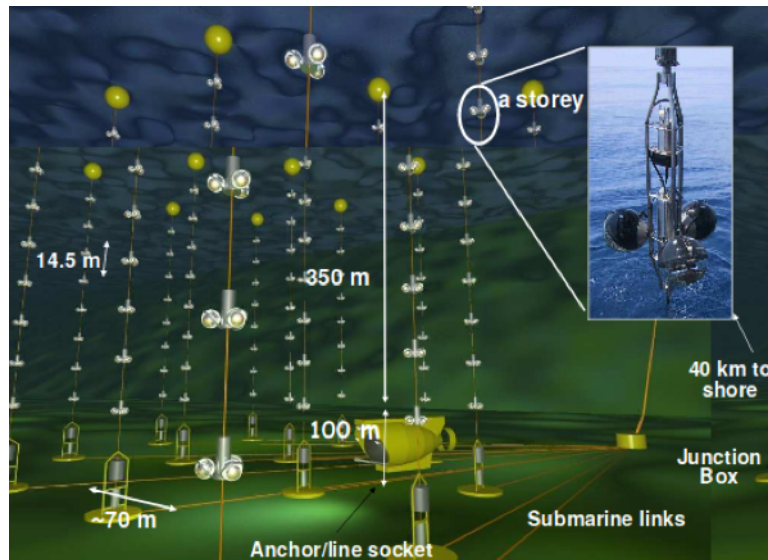
Figure 3.7. Schematic view of the ANTARES detector. Figure from [47].

tube, various sensors and associated electronics, housed in a pressure-resistant glass sphere. Its main component is a 10" hemispherical photomultiplier glued to the glass sphere with optical gel. A μ-metal cage is used to shield the PMT against the Earth magnetic field. Electronic inside the OM are the PMT data acquisition, the DC-DC converter high voltage power supply and a LED system used for internal calibration. The total ANTARES sky coverage is 3.5π sr, with an instantaneous overlap of 0.5π sr with that of the IceCube experiment. The Galactic Centre can be observed 67% of the day time by means of Earth-filtered events.

The arrival time and intensity of the Cherenkov light on the OMs are digitized into 'hits' and transmitted to shore, where events containing muons are separated from the optical background due to natural radioactive decays and bioluminescence, and stored on disk. A detailed description of the detector and of the data acquisition is given in [18] [19].

Background estimation

In the sea water, bioluminescence and radioactive decay of ^{40}K produce a random optical background that can vary between 50 and 300 kHz per PMT, depending for example on the time of the year or the sea current. A multi-level online triggering procedure is applied to select possible particle signatures (see [19] for a more detailed description).

In addition to the cosmic neutrino signal that the ANTARES experiment is searching for, there are other processes that can produce muon tracks in the detector and are considered as background events. As discussed above, by searching only for up-going particles, the atmospheric down-going muon background can be rejected. Nevertheless, muons from above can also produce signals in the detector that appear as up-going events. Using quality cuts on the reconstruction parameters, these falsely reconstructed atmospheric muon tracks can be suppressed to a rate of 0.4 events per day. Atmospheric neutrinos produced by cosmic rays below the horizon can also
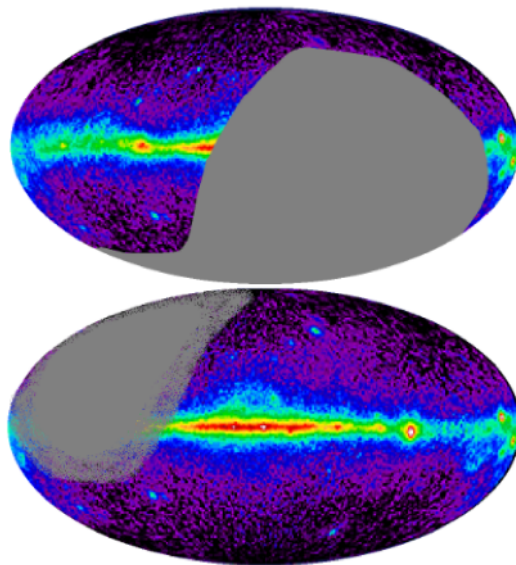
Figure 3.8. Top: Sky observable by IceCube. Bottom: Sky observable by ANTARES, inclusing most of the Galactic Plane (and the Galactic Center too). Figure from [64].

traverse the Earth, and they represent the main background component (~ 3 events per day after quality cuts [16]) to the cosmic neutrinos.

Muon track reconstruction

A particular algorithm, described in [16], is used to reconstruct tracks. It derives the muon track parameters that maximise a likelihood function built from the difference between the expected and the measured arrival times of the hits from the Cherenkov photons emitted along the muon track. This reconstruction returns two quality parameters: the track-fit quality parameter Λ and the estimated angular uncertainty on the muon track direction β. Cuts on these parameters can be used to improve the signal-to-noise ratio. To ensure a good directional reconstruction of the selected neutrino candidates $\beta < 1°$ is generally required. The optimum Λ values range from -5.5 to 5.0 depending on the source and the background characteristics during the flares. These cuts remove most of the remaining atmospheric muons which are mis-reconstructed as up-going tracks.

Detector performances

ANTARES is characterized by an excellent **angular resolution**. The angle between the interacting neutrino and the reconstructed muon, introduced in Equation 3.5, is crucial for establishing the angular uncertainty on the incoming neutrino direction. For $E = 1$ TeV this angle is on average $0.6°$ and decreases with increasing energy. The detector resolution on muon's track is important too. It depends on the alignment between the different components, on PMTs time resolution, on the global time of the read-out system and on the reconstruction quality of the muon tracks. The Figure 3.9 shows the error on angle determination obtained after several quality criteria from muon neutrino interactions as a function of the simulated neutrino
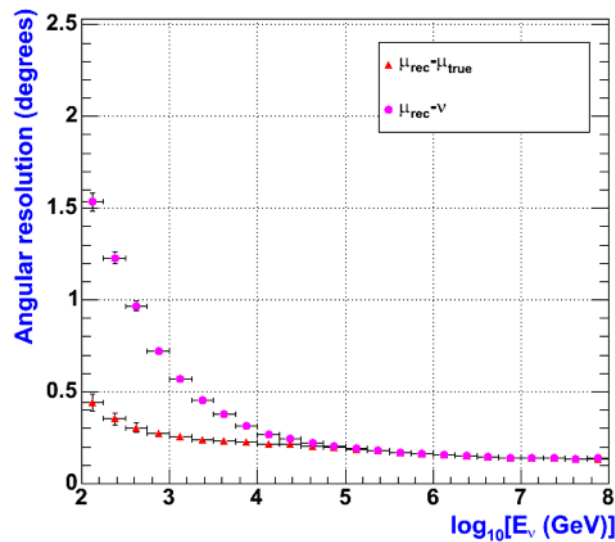
Figure 3.9. ANTARES angular resolution with respect to the neutrino energy. The bottom curve (red points) shows the angle difference between the reconstructed muon and the simulated one. The mismatch is always below 0.5 degree. The top curve (violet points) shows the angular error between the reconstructed muon and the simulated neutrino. Below 1 TeV the error is dominated by the kinematics; above 1 TeV the muon is emitted in the direction of the parent neutrino. Figure from `http://antares.in2p3.fr/Overview/performance.html`.

energy. Above 10 TeV, the ANTARES angular resolution is better than 0.3°. This angular resolution leads to a very good background rejection in cosmic source searches.

The **energy response** is determined by the energy fraction transferred to the muon in the neutrino interaction, the energy lost by the muon outside the detector and the energy resolution of the detector. The muon energy determination requires different techniques in different energy ranges:

- Below 100 GeV, the muons are close to minimum-ionizing, and the energy of contained events, with start and end points measured inside the detector, can be determined accurately from the range. The threshold for this method is about 5-10 GeV for vertical tracks, depending on the vertical distance between groups of optical modules, and about 15 GeV for more isotropic events, depending on the horizontal distance between lines.

- Above 100 GeV, the range cannot be measured because of the limited size of the detector, but the visible range determines a minimum energy that can be used for the analysis of partially-contained events: starting events in which the vertex point is measured inside the detector, and stopping events in which the endpoint is measured.

- Above 1 TeV, stochastic processes (bremsstrahlung, pair production) are dominant, and the muon energy loss becomes proportional to the energy. The

muon range above 1 TeV increases only logarithmically with the muon energy. On the other hand, the detection efficiency increases with energy because of the additional energy loss. Monte Carlo studies have shown that the neutrino energy can be determined within a factor 3 above 1 TeV from the average energy loss.

- Above 1 PeV, the Earth becomes opaque to upward-going vertical neutrinos. Higher energies are accessible closer to the horizon.
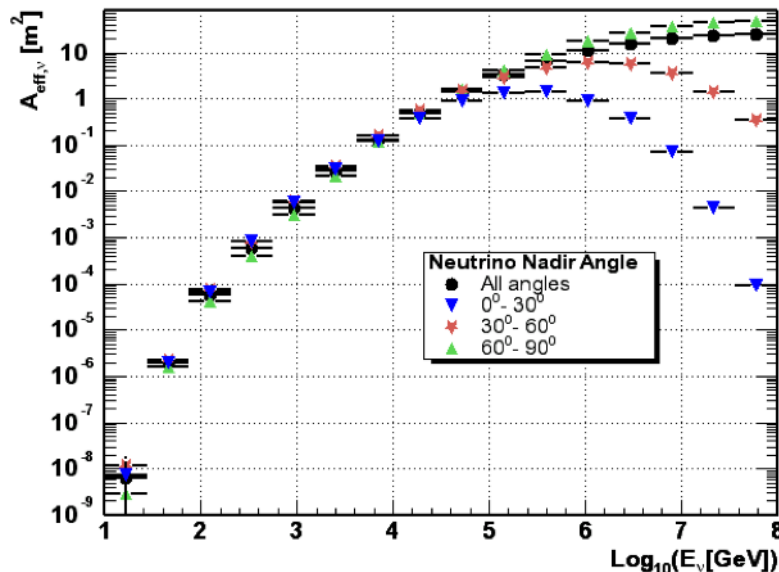
Figure 3.10. ANTARES neutrino effective area with respect to the neutrino energy. Figure from http://antares.in2p3.fr/Overview/performance.html.

In Figure 3.10 the ANTARES **neutrino effective area** A_{eff}[6] is shown as a function of the neutrino energy, for different incoming directions. Around the vertical $(0-30°)$ and above 100 TeV, the Earth starts to become opaque to neutrinos: because of their larger cross section, they interact early and the muon cannot reach the detector. At larger angles the rock thickness is smaller and this effect occurs later in energy. As a consequence the detector remains very efficient at very high energy for nearly horizontal neutrinos.

3.3.3 Major results on high-energy astrophysical sources from neutrino telescopes

Since 2013, a diffuse flux of high-energy cosmic neutrinos has been observed by IceCube, though its origin still nowadays remains unexplained [3]. Recently IceCube has also detected (on 22 September 2017), for the first time, a high-energy neutrino

---

[6]Surface the detector would have perpendicular to the incident particle beam if its detection efficiency was 100%. It is obtained from a full Monte Carlo simulation of neutrino events tacking also into account the selection and reconstruction steps of the analyses. Then, the effective area is the ratio of the rate of detected events (s^{-1}) over the incident flux $(cm^{-2}s^{-1})$.

event coincident in direction and time with a gamma-ray flare from the blazar TXS 0506+056, with a significance level of $3.5\,\sigma$ [8]. This discovery was greeted with great enthusiasm by the entire scientific community as it establish the first cosmological neutrino source ever detected.

Interestingly, to date, no correlation with GRBs has been observed yet. The IceCube Collaboration itself has been searching for high energy neutrino signals coincident in time and direction with these sources. From the absence of a signal, upper limits on the neutrino flux from these objects has been establishing assuming an E^{-2} neutrino spectrum from the source, as foreseen by standard acceleration theory. The latest all-sky search for muon neutrinos produced during the prompt γ-ray emission involved 1172 GRBs distributed over the whole sky. In fact, the short pulse duration allows for a search also from the down-going direction. No correlation between neutrino events and observed GRBs was identified and new constraints for single-zone fireball models of GRB neutrino production was obtained [7]. Assuming an $E^{-2.5}$ ($E^{-2.13}$) neutrino spectrum, IceCube has constrained the contribution of long GRBs to the astrophysical neutrino flux to at most for 5% (30%) [9].
So far, a non detection was registred also within the data of the ANTARES detector regarding spatial and temporal neutrino coincidences with GRBs. Analogously to IceCube, 90% confidence level upper limits on the expected signal fluences have been derived (e.g. [20]). A more detailed description of the neutrino flux expectations and the analysis method i provided in Chapter 6.
Constraints on GRB parameters have been also derived, though they do not yet constrain neutrino emission models. Further investigations will be possible with the incoming generation of neutrino detectors, such as KM3NeT-ARCA [17] and IceCube-GEN2 [4].

Chapter 4

GRB 110918A light curve analysis

In this Chapter an innovative study proposed for GRB light curves is presented. The aim of this thesis is the study of one particular GRB, GRB 110918A. The Chapter is organized as follows: in Section 4.1 the procedure adopted to select GRB 110918A is explained; in the following Section 4.2, the light curve characteristics are shown, among which the non-linearity and non-stationary of its data (4.2.1). Finally the impact of characteristic parameters of GRB light curves on their profile has been analyzed by means of simulations, as described in Section 4.3.2.

4.1   Procedure for GRB selection

GRB data from the *Konus-WIND* satellite have been considered[1]. Konus is GRB monitor launched on the Russian GGS-WIND spacecraft in November 1994. The Konus detector array consists of two unshielded gamma ray sensors located on opposing spin axes of the spacecraft. In interplanetary space far outside the magnetosphere, Konus has two advantages over Earth-orbiting GRB monitors: continuous coverage uninterrupted by Earth occultation and a steady background unaffected by passages through the trapped radiation. Data are given in the energy band 50-20 keV with a time sampling of 64 ms.
GRBs have been selected based on their duration (long GRBs), fluence (fluence larger than 10^{-5} erg cm^{-2}), their light curves profile (presence of pulses and quiescent periods) and their temporal characteristics (non linear and non stationary data). With this selection, GRBs which show high temporal variability, that according to models can be explained by a sequence of phenomena in the sources, have been identified. The attempt will be to try to attribute the visible characteristics of the light curve to the sequence of phenomena (modes) that characterize the source. This study will be performed by the subsequent use of the Empirical Mode Decomposition (EMD) on the selected light curve (see Chapter 5). In Table 4.1 the initially selected GRBs and their characteristic values are shown. All the parameters presented in the table are taken either from the literature corresponding to the selected GRB or

---

[1] https://gcn.gsfc.nasa.gov/konus_grbs.html.

from the Gamma-ray bursts Coordinate Network (GCN) archive[2], except for the isotropic-equivalent luminosity L_{iso}. This last quantity is related to GRB duration and to the total measured fluence in γ-rays via the redshift z and it is calculated through the following relation:

$$L_{\mathrm{iso}} = 4\pi d_L^2(z)\frac{F_\gamma}{T_{90}},\tag{4.1}$$

where $d_L(z)$ is the luminosity distance, which depends on the redshift and on parameters assumed from the cosmological model (ΛCDM)[3].

	F_γ	T_{90}	t_{v}	z	L_{iso}
	(erg cm^{-2})	(s)	(s)		(erg s^{-1})
GRB 080411	6.3×10^{-5}	56	-	1.031	6.46×10^{51}
GRB 081009	3.1×10^{-5}	41	0.16	2.150	3.07×10^{52}
GRB 110918	7.5×10^{-4}	19.64	0.25	0.984	4.40×10^{54}
GRB 120919	1.4×10^{-5}	21	-	0.267	1.49×10^{50}
GRB 160422	8.7×10^{-5}	12	-	1.237	6.56×10^{52}
GRB 161020	5.1×10^{-5}	38	-	1.379	1.60×10^{52}
GRB 130504	2.0×10^{-4}	73	-	0.416	1.72×10^{51}
GRB 130505	3.1×10^{-4}	21	-	2.270	6.12×10^{53}

Table 4.1. Selected GRBs and their parameters. From left to right: GRB name; fluence; GRB prompt duration expressed through the T_{90} variable, defined in 2.2.2; variability time, also defined in 2.2.2; redshift; isotropic-equivalent luminosity. Values of the fluence F_γ refer to the Konus-WIND spectra energy range: $20\ \mathrm{keV} - 10\ \mathrm{MeV}$.

Among these gamma-ray bursts, GRB 110918 (or GRB 110918A) was selected because it is the brightest one, it has peculiar light curve characteristics (described in the next Section 4.2), its data are nonlinear and, importantly, its variability time is known. Indeed, this gives an important help and information for the light curve simulation (see Chapter 4.)

4.2 GRB 110918A

The ultraluminous GRB 110918A is the brightest long GRB detected by Konus-WIND (KW) during its observation years and the most luminous one observed until now. Unfortunately, both Swift and Fermi satellites were Earth-occulted at the time of the burst [85], but Swift could still observe the afterglow emission after ~ 30 hours. A comprehensive analysis of this GRB observations was presented by [57], from which all the necessary information for the purpose of this work has been obtained. It was detected by the satellite at $T_0 = 77222.856\ \mathrm{s}$ UT $(21:27:02.856)$ on 2011 September 18th by a Konus detector which observes the Southern ecliptic hemisphere, with an incident angle of $53°.1$. The propagation delay from the Earth to WIND was 3.928 s for this GRB: correcting for this factor the KW trigger time corresponds to the Earth-crossing time $T_0 = 77218.928\ \mathrm{s}$ UT $(21:26:58.928)$.

---

[2]https://gcn.gsfc.nasa.gov/gcn3_archive.html.
[3]Standard cosmological model values: $H_0 = 71\ \mathrm{km\ s^{-1}\ Mpc^{-1}}$, $\Omega_M = 0.27$, $\Omega_\Lambda = 0.73$.

Time interval	α	β	E_p	F_γ
(s)			(keV)	$(10^{-4} \text{ erg cm}^{-2})$
0.000-28.416	$-1.64^{+0.06}_{-0.05}$	$-2.25^{+0.09}_{-0.09}$	340^{+70}_{-60}	$7.78^{+0.46}_{-0.45}$
0.000-2.304	$-0.95^{+0.05}_{-0.05}$	$-2.41^{+0.10}_{-0.12}$	990^{+100}_{-90}	$4.03^{+0.11}_{-0.11}$
0.000-13.312	$-1.12^{+0.08}_{-0.08}$	$-2.28^{+0.08}_{-0.10}$	630^{+160}_{-100}	$6.09^{+0.34}_{-0.38}$
13.312-28.416	$-1.2^{+0.2}_{-0.1}$	$-3.3^{+0.2}_{-0.2}$	78^{+3}_{-3}	$1.57^{+0.}_{-0.27}$

Table 4.2. Konus-WIND time-averaged spectral fits with the Band function. For the parameter explanation see Section 2.2.1. Values of the fluence F_γ refer to the 20 keV $-$ 10 MeV energy band.
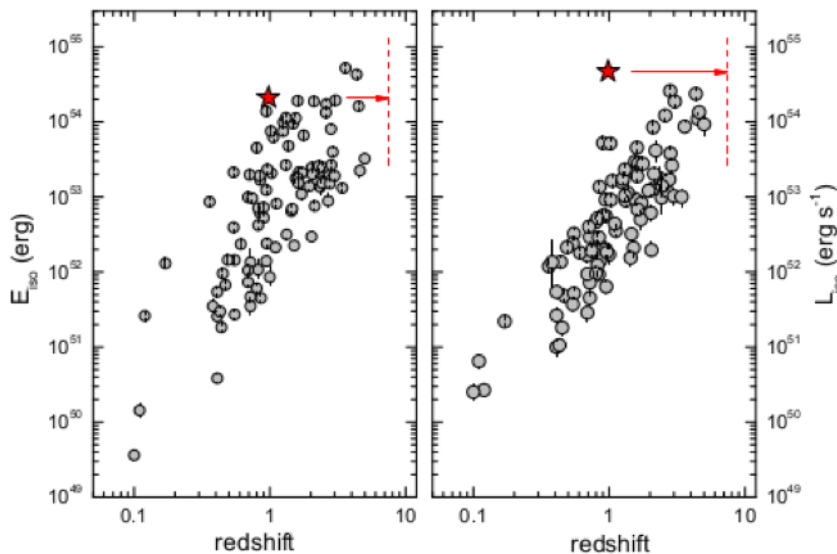
Figure 4.1. E_{iso} (left) and L_{iso} (right) of Konus-WIND GRBs with known redshift. The GRB 110918A is indicated by the red star. The grey circles show data for the KW bursts. The dashed line indicates the KW detection horizon for a similar ultraluminous GRB ($z \sim 7.5$). Figure from [57].

Considering the standard Band function for the description of the GRB energy spectrum as observed in γ rays (see Equation 2.1), the averaged total spectrum is characterized by values indicated in Table 4.2. These values are from [57], where furthermore the values for the average spectrum of the initial pulse are given from T_0 to $T_0 + 2.304$ s, for the first part of the light curve, from T_0 to $T_0 + 13.312$ s, and for the second one, from $T_0 + 13.312$ s to $T_0 + 28.416$ s. It is evident that the initial pulse, the brightest one, is very hard too, while the remaining part of the GRB 110918A light curve is softer.

From optical afterglow observations made with the Gran Teloscopio Canarias at Roque de los Muchachos Observatory, the GRB was estimated at $z = 0.984 \pm 0.001$ [50]. At this redshift, the high energy fluence measured by Konus-WIND, $7.5 \times 10^{-4} \text{ erg cm}^{-2}$, implies a huge isotropic equivalent energy released in the source frame, $E_{\text{iso}} = (2.1 \pm 0.1) \times 10^{54}$ erg, and an isotropic-equivalent peak luminosity
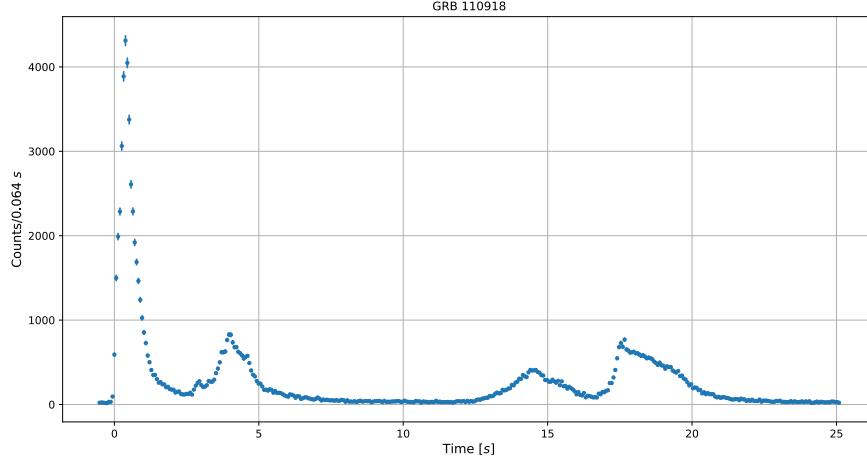
Figure 4.2. GRB 110918A light curve detected by Konus-WIND satellite at $T_0 = 77222.856$ s UT $(21:27:02.856)$ on 2011 September 18. This light curve is reproduced by using available on-line data from `https://gcn.gsfc.nasa.gov/konus_grbs.html`. The available data go from $T_0 - 0.512$ s to $T_0 + 98.7521$ s. In this plot the data from 25 s to ~ 100 s have been removed to focus on prompt emission. The error on counts is calculated as Poisson noise, $\sqrt{\text{counts}}$.

$L_{\text{iso}} \sim 4.4 \times 10^{54}$ erg s^{-1} (see Figure 4.1).

The GRB light curve, shown in Figure 4.2, starts with an extremely bright and short pulse (more than half of its energy, $\sim 55\%$, is released in the initial pulse) followed by three weaker and partly overlapping pulses in the next ~ 25 s, showing a long quiescent period (~ 10 s) between the second and the third peak. The total duration of the burst is $T_{100} = 95.154$ s and the corresponding T_{90} value is 19.6 ± 0.1 s. T_{100} and T_{90} are in this case not similar measures of duration, which is not a characteristic condition of the less bright GRBs [120]. Furthermore, assuming that the shortest timescale in GRB prompt emission (variability time t_{v}) is the shortest pulse width δT, the value $t_{\text{v}} \simeq \delta T = 0.25$ s was estimated.

4.2.1 Non-linearity and non-stationary study

The time series of a GRB is generally a non-stationary time series and all of its statistical properties vary with time. Considering long GRB as a manifestation of a stochastic process, time-dependent and time-averaged probability density functions (PDFs) have been studied, following the method proposed by N. Bhatt & S. Bhattacharyya [36]. The PDFs, in fact, characterize the underlying stochastic process and allow to define the linearity or non linearity of the considered data. The method is characterized by the following steps:

1. The GRB light curves are divided into different time segments, each characterizing distinct pulses of the GRBs, to study the time evolution of the PDF;

2. Each time segment is then divided in smaller time intervals from the starting

time t to $t + \tau$, where the length of τ is chosen by visually inspecting the GRB time structure and by finding the correct and stable-results binning for each of them;

3. For each of these intervals the PDF is calculated as:

$$\mathrm{PDF}_{t,t+\tau}(x) = \frac{\Delta N_x}{N} \pm \frac{\sqrt{\Delta N_x}}{N}, \qquad (4.2)$$

where x represents the count rate, ΔN_x is the number of points (along the y-axis in light curves, i.e. count rates) in the interval Δx from x to $x + dx$, and N is the total number of points in the considered time segment.

4. The curve obtained with PDF points in each time segment is fitted with a single or multiple Gaussian distributions given by:

$$F(x) = \sum_{i=1}^{M} A_i \exp\left[-\frac{1}{2}\left(\frac{x - \mu_i}{\sigma_i}\right)^2\right], \qquad (4.3)$$

with $M \geq 1$. The amplitude A_i, the mean μ_i and the standard deviation σ_i of each Gaussian distribution are output values by the fit.

If PDFs are non-fittable with a Gaussian function the physical underlying stochastic process can be considered nonlinear, which is a preliminary condition for the EMD study.

GRB 110918A, which from the beginning was one of the best candidates for its characteristics, as already explained in Section 4.2, also respects the non-linearity and non-stationary request. As shown in Figure 4.3, the probability density function of GRB 110918A, calculated as indicated in Equation 4.2, does not remain independent on the time and consequently its time series is non-stationary.
Regarding the linearity study, four different time segments have been chosen, [-0.5, 2.7] s, [2.7, 10.0] s, [10.0, 16.7] s, [16.7, 25.1] s, which are indicated with different colors in Figure 4.3a. From the extrema of each time-segment, the best number of bins has been calculated and used for calculating the probability density function through the Equation 4.2. Since in each case the best one was $N_{\mathrm{bins}} \sim 50$, this value has been used in all four time intervals, calculating the corresponding Δx (Figure 4.3). In Table 4.3 fit results for $N_{\mathrm{bins}} = 50$ are shown. The cases $N_{\mathrm{bins}} = 40$ and $N_{\mathrm{bins}} = 60$ have been studied too, for checking if the results were stable or not (see Appendix A for additional figures). It is clear that almost all the intervals are not fittable with a Gaussian function. Using this same study separately for quiescent periods and peaks, it is evident that the non-linearity comes from the instantaneous bursts produced by the GRB central engine. Since the total probability density function is sum of non-Gaussian distributions evolving with time, the GRB 110918A light curve can certainly be regarded as non-stationary and non-linear. The reason for which this result makes the GRB suitable for the analysis of this work will be better understood in Chapter 5.

(a)

(b)

(c)

(d)

(e)
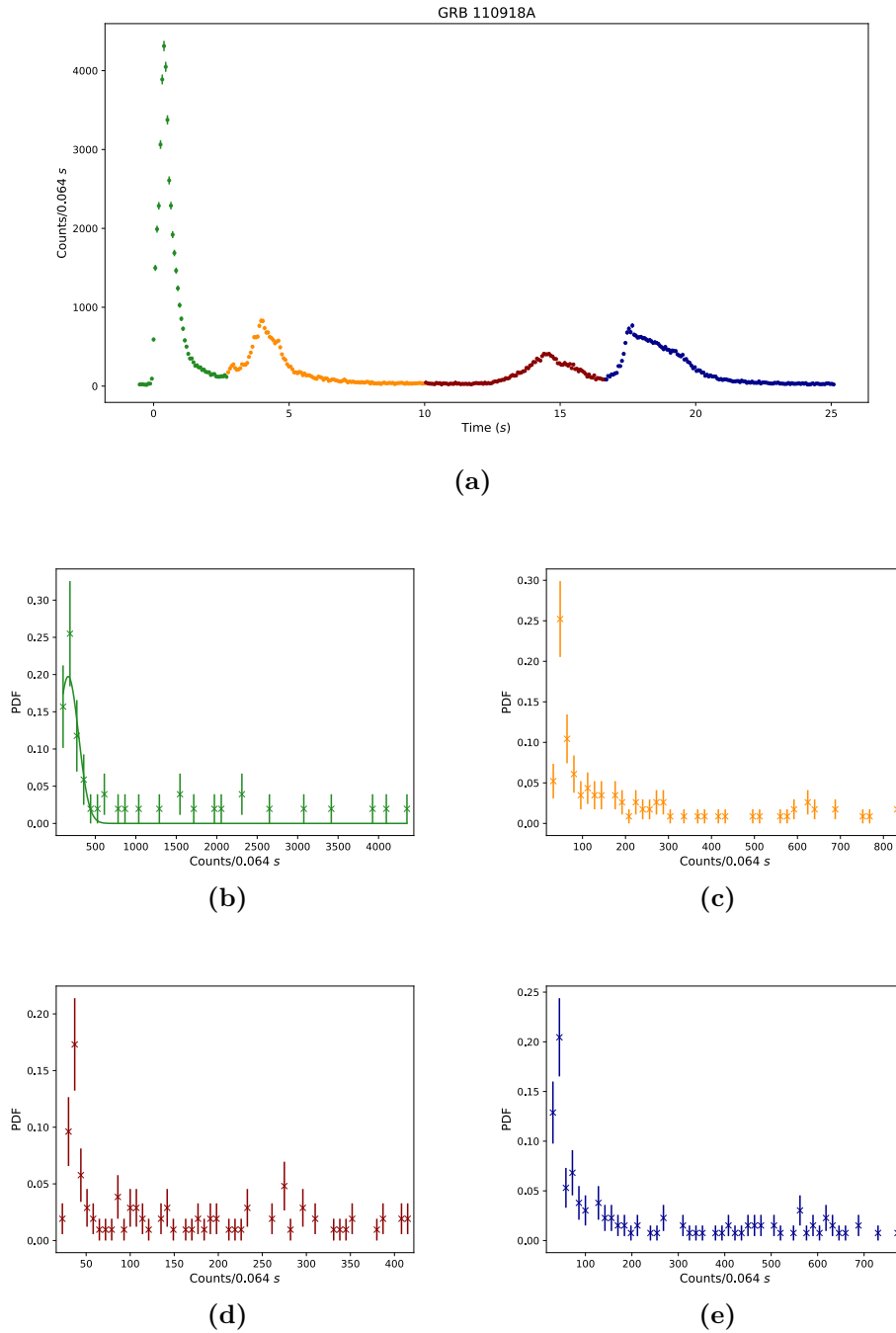
Figure 4.3. Light curve of GRB 110918A, in which each color corresponds to a different portion of the light curve (Figure (a)), and time-dependent PDF for each of these time intervals: Figure (b): [-0.5,2.7] s, $\Delta x = 85$ s^{-1}, $N_{\text{bins}} = 50$; Figure (c): [2.7, 10.0] s, $\Delta x = 16$ s^{-1}, $N_{\text{bins}} = 50$; Figure (d): [10.0, 16.7] s, $\Delta x = 7$ s^{-1}, $N_{\text{bins}} = 50$; Figure (e): [16.7, 25.1] s, $\Delta x = 14$ s^{-1}, $N_{\text{bins}} = 50$.

| Time | M | A_i | μ_i | σ_i | χ^2/ν |
(s)			(s^{-1})	(s^{-1})	
-0.5 - 2.7	1	0.197	164.26	127.50	1.088
2.7 - 10.0	-	-	-	-	-
10.0 - 16.7	-	-	-	-	-
16.7 - 25.1	-	-	-	-	-

Table 4.3. Fitted parameters in GRB 110918A in the case of $N_{\text{bins}} = 50$. From left to right: time segment; peaks number; gaussian parameters, the goodness-of-fit parameters. Only the first peak gives a Gaussian function.

4.3 Numerical simulations within a multi-collision approach

One of the objectives of this work is to draw conclusions on GRB 110918A-like light curves comparing the real light curve with a simulation that closely resembles it.
In order to obtain a simulated light curve similar to the observed GRB 110918A one, the *NeuCosmA code*, described by Hümmer et al. (2010) [77], has been used.
NeuCosmA is a Python code for the simulation of hadronic interactions in GRBs environments, including not only the Δ^+ resonance 2.5 but also higher mass resonances

$$p + \gamma \to K^+ + \text{neutral hyperon} \tag{4.4}$$

and the following kaon decay

$$K^+ \to \mu^+ + \nu_\mu. \tag{4.5}$$

It simulates collisions in a GRB jet, following the internal shock model (Section 2.10), constructs synthetic GRB light curves and estimates an expected neutrino flux for GRBs through, after some recent proposals (e.g. [27], [43]), the so-called *multi-collision approach.*

Multi-collision vs. one-collision approach
In the multi-collision approach great improvements to the light curve simulation and to the neutrino flux estimate are obtained with respect to the classical *one-zone collision approach*, in which all collisions are supposed to be identical. Indeed, in this latter case average shell properties (that can be derived from observations) are assumed, and neutrino emission is computed for a single representative collision which is then rescaled by the number of collisions to yield the total flux of the burst. In the multi-zone approach, instead, a system of plasma shells with a distribution of Lorentz factors, masses and widths is evolved, leading to collisions at different radii. Thus, this model is clearly more realistic than the other one. A different amount of energy and particles is released in each collision, because physical conditions vary. All pulses are superposed to obtain the GRB light curve and particle fluxes. It suggests a GRB multi-zone production for either neutrinos, γ rays and cosmic rays, which significantly lowers the neutrino expected flux with respect to the previous
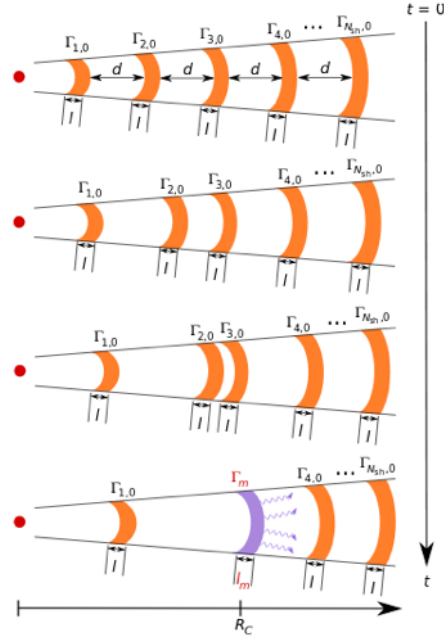
Figure 4.4. Illustration of the multi-collision model used in the NeuCosmA code. The central engine emits a set of shells (N_{shell}) with same width l and separation between each other d but with different Lorentz factors $\Gamma_{\text{k},0}$. A faster shell catches up with a slower one, initiating a collision, during which particles are accelerated and emitted. The result of this process is that a merged shell is formed. The new shell continues its propagation within the fireball and eventually collides with another shell. Figure from [43].

predictions. Figure 4.4 illustrates how the NeuCosmA code simulates the coasting phase of the GRB. For more details see [43].

4.3.1 Simulated light curve

To obtain the simulated light curve with the NeuCosmA code, general features have been considered [43]:

- The overall duration of the burst scales with the initial size of the fireball (i.e. the separation between the first and last shell). This is because the fireball travels at almost the light speed and the observed time of a single collision is unrelated to the absolute collision radius but instead relates to the relative position within the fireball;

- The observed variability timescale scales with the number of collisions which in turn is directly related to the initial number of shells;

- The width of single pulses (created by the emission from one single collision) depends on the shell sizes as larger shells produce wider peaks. It is relevant to recall here that during collisions, shells are compressed, thus those ones produced at later times are expected to have a negligible impact on the total light curve.

- Bright collisions are those between shells which have a very large difference in Lorentz factors;

- The order in which the shells collide depends only on the distance between neighboring shells and their relative Lorentz factors;

- To achieve a broader structure in the light curve, it is convenient to put an underlying broad structure in the initial fireball, i.e. regions with both very fast and very slow shells;

- The variability in the light curve is created by fluctuations of the Lorentz factors of neighboring shells;

- The light curve does not trivially relate to the initial shell configuration since

  1. a strong variability in a region of the fireball leads to a slowdown (the variability causes collisions which emit high amounts of energy and therefore reduce the speed of the produced merged shell),

  2. strong light curve pulses are only created by fast regions running into slow ones.

Starting from these considerations, a simulation reproducing the inner jet dynamics was performed. Several input parameters were required to start the simulation, as the initial radii distribution and the Lorentz factor distribution. The former, in Table 4.4, was fixed as explained below.

- $R_{\min}$ and $R_{\max}$, the distance from the innermost shell to central emitter and the deceleration radius (where the circumburst medium starts), respectively, have been decided starting from limit values calculated following the standard formulae:

$$R_{\min} = 2\Gamma^2 \frac{ct_{\mathrm{v}}}{1+z}, \tag{4.6}$$

$$R_{\max} = 2\Gamma^2 \frac{cT_{90}}{1+z}. \tag{4.7}$$

  The variability time t_{v}, the burst duration T_{90}, the sound speed c, and the redshift z are known, while Γ is an average value over the jet, which is assumed to coincide with the inferred lower limit of the bulk Lorentz factor of the GRB ejecta $\Gamma > 360$ [57].

- The initial number of shells N_{shell} is the minimum value reproducing the observed light curve profile and output values for variability time t_{v}, burst duration T_{90} and collisions number N_{coll} close to the known ones from the literature.

- The initial common shells width l and the common separation between consecutive shells d influence the produced light curve by the simulation, as discussed in Appendix C. The selected value is reported below.

- The initial mass of individual shells $m_{\mathrm{k},0}$ is a standard value, already present in the code. The assumption under which the simulation has been done is that $m_{\mathrm{k},0}$ is equal for all k (equal-mass assumption).

Input parameters	Units	Values
N_{shell}	-	110
$R_{\min}$	km	1.4×10^{10}
$R_{\max}$	km	6.0×10^{11}
l	km	7.5×10^4
d	km	6.0×10^3
$m_{\text{k},0}$	GeV	2.0×10^{49}
z	-	0.984

Table 4.4. Input parameters for the burst simulation in Figure 4.8. From top to bottom: initial number of shells; distance from the innermost shell to central emitter; deceleration radius (where the circumburst medium starts); initial shell width; initial separation between consecutive shells; initial mass of the k-th shell; redshift of the emitter.

Radius generation and Lorentz factor distribution

Before deepening some of these choices, let's focus on the used radius generation and the Lorentz factor distribution. The obtained light curve has been produced assuming an intermittent engine (because of the GRB structure) to reproduce the long quiescent period (inactivity period of the central engine) between the two central peaks. The initial values of shells Lorentz factors $\Gamma_{\text{k},0}$, are randomly sampled from a log-normal distribution defined by the characteristic value Γ_0 and the amplitude of fluctuations A_Γ:

$$\ln\left(\frac{\Gamma_{\text{k},0} - 1}{\Gamma_0 - 1}\right) = A_\Gamma \cdot x, \tag{4.8}$$

where the random variable x follows a Gaussian distribution $P(x)dx = (2\pi)^{-1}e^{-x^2/2}dx$. The characteristic distribution values used for reproducing the simulated light curve are reported in Table 4.5.

Since x is randomly extracted, 500 simulations have been done and the averaged light curve has been computed. A very small value of the amplitude of fluctuations A_Γ has been chosen because, for a larger one, it has been verified that, in each simulation, the light curve profile changes enough to alter the final averaged result. However, it was decided to perform 500 simulations in order to have a fairly high statistics of output values to be compared with the known ones.

Comparison with known values of GRB 110918A

The NeuCosmA code returns in output the variability time t_{v}, the burst duration T_{90} and the collisions number N_{coll}, which is related to previous quantities as

$$N_{\text{coll}} = \frac{T_{90}}{t_{\text{v}}}. \tag{4.9}$$

In Figure 4.5 t_{v}, T_{90} and N_{coll} distributions after 500 simulations performed with the values in Tables 4.4 and 4.5 are shown. After performing a Gaussian fit, the values indicated in Table 4.6 were obtained. These are consistent with the known quantities for the GRB 110918A, thus the following results can be safely extracted based on the assumptions reported so far.

N_{shell}	Γ_0
1	100
2	950
3	450
4	820
5	450
6-7	1080
8	1900
9-110	100

Table 4.5. Characteristic values Γ_0 of log-normal distribution in Equation 4.8 for each shell or group of shells considered in the simulation. The amplitude of the fluctuations A_Γ is always considered to be 0.01.
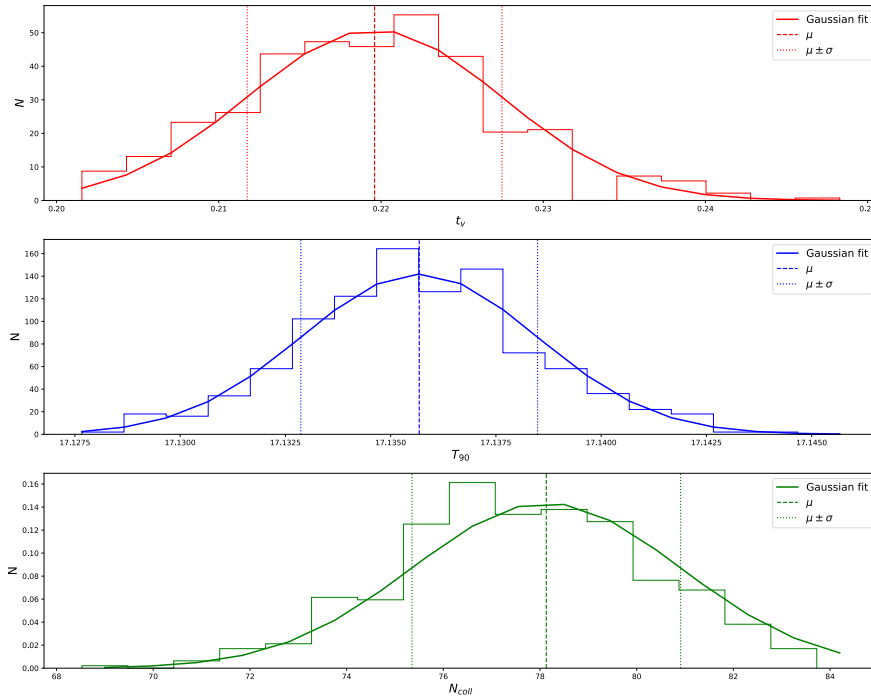
Figure 4.5. Distributions of output parameters after 500 simulations performed with the values in Tables 4.4 and 4.5. First panel (red): variability time t_{v}; second panel (blue): burst duration T_{90}; third panel (green): collisions number N_{coll}. The thick line shows the Gaussian fit, the dashed line shows the central value of the distribution, μ, and the dotted lines indicate $\mu \pm \sigma$, where σ is the standard deviation of the Gaussian distribution. Fit results are also indicated at the top of each panel.

	Simulation	GRB 110918A
t_{v} (s)	0.220 ± 0.008	0.25
T_{90} (s)	17.136 ± 0.003	19.6 ± 0.1
N_{coll}	78 ± 3	$T_{90}/t_{\mathrm{v}} \cong 79$

Table 4.6. Comparison between variability time t_{v}, burst duration T_{90} and collisions number N_{coll} for GRB 110918A (second column) and for the averaged simulated light curve (first column).

Equal-mass assumption

In the code two different schemes can be selected in order to assign initial masses to the shells: either the equal-mass assumption or the equal-energy one. To fix this choice a result by Nakar & Piran (2002) [100] has been used as they studied the relation between the observed γ-ray light curve and the inner engine's activity. Defining the pulses width, δt, and the intervals between pulses, Δt, the authors found, thanks to simulations, that in the equal-mass model δt distribution is shorter than the Δt one, while in the equal-energy model δt and Δt reflect the same distribution (Figure 4.6). In the equal-energy shells model the similarity between the Δt and δt distributions is due to the fact that both parameters reflect the separation between the shells during their injection, while in the equal-mass shells model only Δt reflects the initial shells separation, and therefore such a similarity is not expected [100].
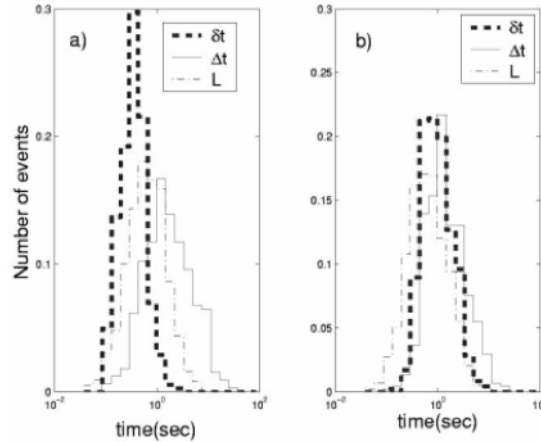
Figure 4.6. Distributions of pulses width δt, intervals between pulses Δt and separation between shells L. Figure (a): Equal-mass shells simulation. Figure (b) Equal-energy shells simulation. Figure from [100].

Here, the Konus-WIND GRB 110918A light curve has been analyzed adopting the Li & Fenimore (1996) peak finding algorithm (PFA) [93], as it allows to extract δt and Δt values directly from the GRB light curve (Table 4.7). It is visible that the obtained δt distribution is shorter than the Δt one (Figure 4.7). For this reason, simulations with equal-mass assumption were selected. For a further insight into the Li & Fenimore algorithm and more details about its application on GRB 110918A light curve see Appendix B.
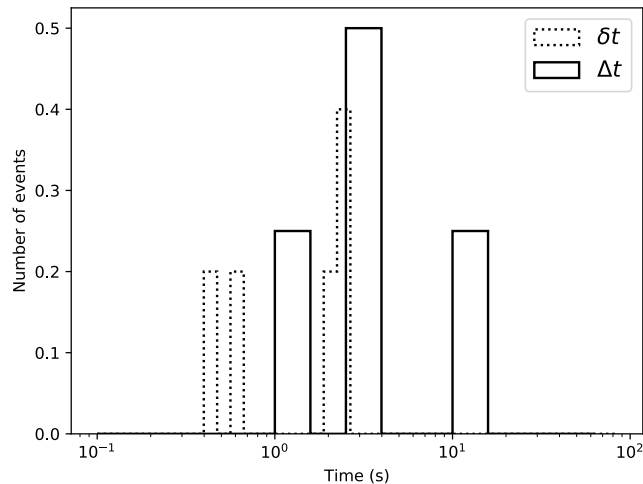
Figure 4.7. Distributions of pulses width δt (dashed line) and intervals between pulses Δt (solid line) for GRB 110918A light curve. The number of events is normalized to the total counts number.

δt	Δt
(s)	(s)
0.816 ± 0.080	2.560
0.446 ± 0.023	1.024
2.019 ± 0.155	10.432
2.471 ± 0.058	3.264
2.597 ± 0.111	-

Table 4.7. Pulses width δt and intervals between pulses Δt obtained for GRB 110918A light curve. Δt values have not errors, because directly calculated from real data; δt values, instead, have errors too because they have been obtained propagating parameters errors returned by Gaussian fits considering the Equation B.3. For more details about the δt calculation see Appendix B.

Using the parameters and assumptions just explained, the resulting light curve that has been obtained after 500 simulations is shown in Figure 4.8. The simulated and observed light curve profiles and their characteristic parameters seem to show that the model assumptions reproduce the observed GRB 110918A light curve well. However, the chi-squared test does not return a good value; comparing the observed data c_{obs} to the simulated and averaged ones c_{sim} for each point,

$$\chi^2/\nu = \frac{1}{\nu} \sum_{i=1}^{N} \frac{(c_{\mathrm{obs}} - c_{\mathrm{sim}})^2}{\sqrt{(c_{\mathrm{obs}} + c_{\mathrm{sim}})}} \simeq 819 \qquad (4.10)$$

is obtained, where ν is the degree of freedom (i.e. number of points in the light curve) and the error on counts is calculated as Poisson noise. Indeed, while in the first part the averaged light curve reproduces the observed GRB 110918A one quite

well, after the long quiescent period the two light curves are a bit different, even if they reproduce the times at which the peaks are observed and the distance between the two, which is the important thing for the purposes of this work.
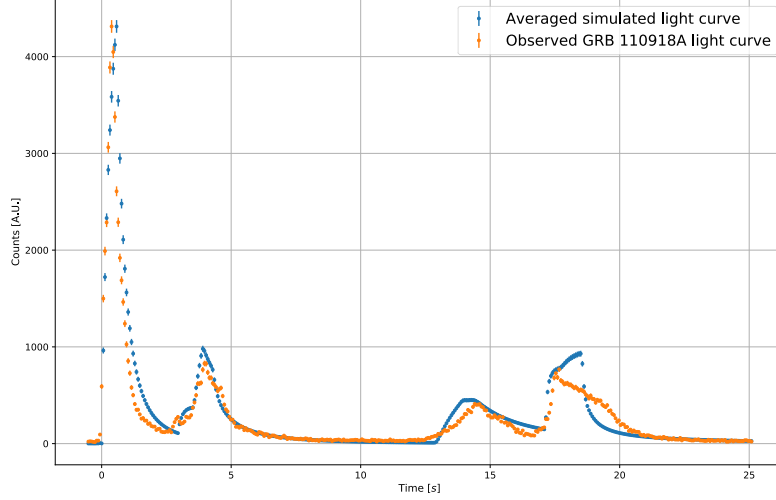
Figure 4.8. Comparison between the Konus-WIND GRB 110918A light curve (in orange) and the averaged simulated light curve reproduced with the NeuCosmA code (in blue). The error on counts is calculated as Poisson noise, $\sqrt{\text{counts}}$.

An interesting and immediate consideration that can be derived is that the number of observed pulses (5) is much smaller than the number of ejected shells ($N_{\text{shell}} = 110$): the inner engine is far more variable than the observed light curve, in agreement with other previous studies (e.g. [100]).

4.3.2   Light curve characterization study

The influence of input parameters on the synthetic light curve produced in the simulation is here investigated. In particular, several test were run, in which alternatively one among the parameters reported in Table 4.4 was modified, maintaining fixed all the others. This has been applied to t_{v}, T_{90}, N_{coll}, δt, Δt and amplitude of peaks A. Every time 500 simulations were performed, in order to consider the average light curve. The PFA algorithm has been applied on each of them to derive δt, Δt and the amplitude of peaks, while t_{v}, T_{90} and N_{coll} have been extracted from their distribution in the same way described in Section 4.3.1. In this Section only the most important plots are reported (which regard the quantities that change); see Appendix C for the other ones obtained for this study and related to the considerations that are below.

The PFA algorithm identifies four peaks without a precise dependence (no strong correlation) between their heights and the initial number of shells; furthermore, δt and Δt do not change significantly with N_{shell}, not altering the light curve profile.

Indeed, also the burst duration T_{90} does not change for different initial number of shells. The only quantities that vary with N_{shell} are the variability time t_{v} (in an exponential way) and, obviously, the collisions number N_{coll} (linear dependence), related to each other by the Equation 4.9 (Figure 4.9).
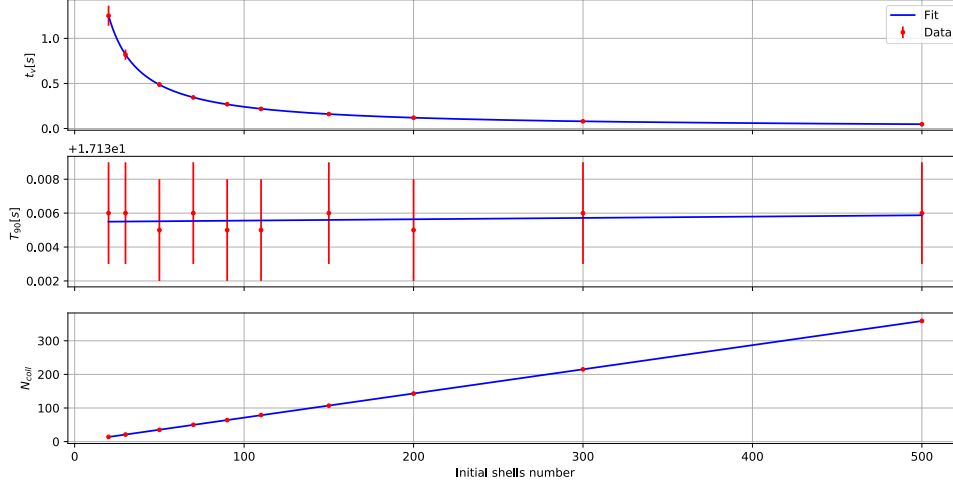
Figure 4.9. Variability time t_{v}, burst duration T_{90} and number of collisions N_{coll} (from top to bottom, respectively) as a function of the initial number of shells.

However, as N_{shell} increases (decreases), collisions increase (decreases) too. Most of them are inactive collisions, which do not change the GRB light curve and characteristics of its peaks. Therefore, the light curve reflects the emission time only of a small amount of shells.

Particularly important is how the Lorentz factors of the shells influence the light curve. Since the first peak, determined by the first shells emitted by the central engine, is the most important one because it dominates the entire light curve, it has been studied how the light curve changes with the variation of the Lorentz factor of these shells ($\Gamma_{0,1}$ and $\Gamma_{0,2}$ were modified). Increasing $\Gamma_{0,1}$ and $\Gamma_{0,2}$ the first burst is more and less intense and occurs before and after, respectively. A different behavior happen also for the other peaks (Figure 4.10). As regard δt and Δt, it is observed that, with the increase of $\Gamma_{0,2}$, the first peak becomes exponentially narrower, while the third and the fourth ones tighten linearly. Furthermore, the second peak moves away from the first, while the others approach. As a consequence the burst duration decreases while the number of collisions remains almost constant (~ 79) (Figure 4.15). If, instead, it is $\Gamma_{0,1}$ to increase, Δt follows the same behavior now described, but δt has exactly the opposite one: the first peak becomes exponentially wider and the others tighten (Figures 4.13 and 4.14). In this case, in fact, T_{90} increases and N_{coll} decreases (Figure 4.15). Therefore, if $\Delta\Gamma_{1,2} = \Gamma_{0,1} - \Gamma_{0,2}$ decreases, the collisions number decreases too. The initial common width l and common separation d of shells also influence t_{v}, T_{90} and N_{coll}; in both cases either t_{v} or T_{90} increase linearly with greater l and d, instead N_{coll} decreases (Figure 4.11).
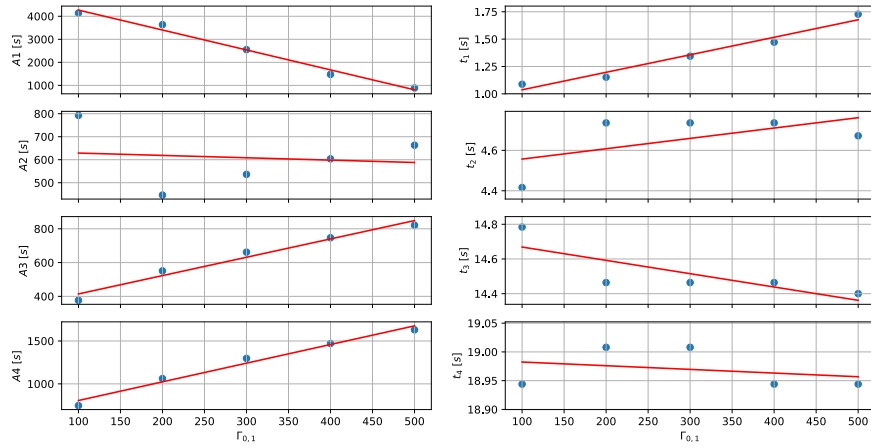
(a)
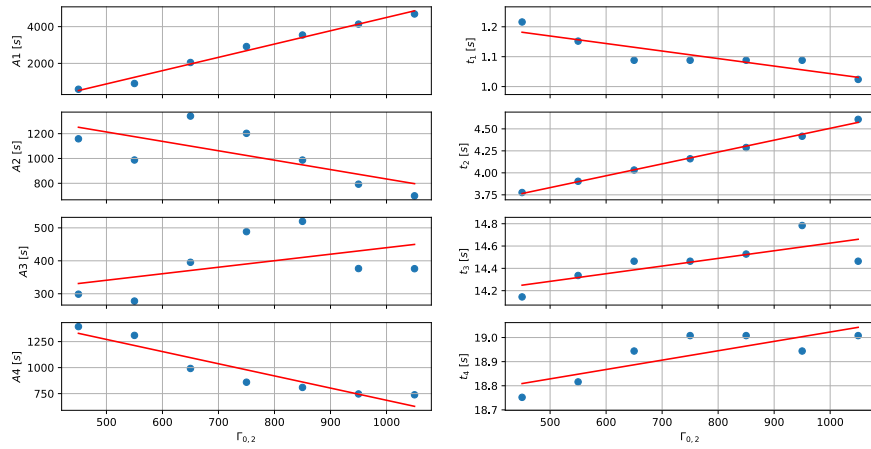
(b)

Figure 4.10. Height of peaks A_k (left) and time at which they occur t_k (right), with $1 \leq k \leq 4$, as a function of the first shell Lorentz factor $\Gamma_{0,1}$ variation and the second shell Lorentz factor $\Gamma_{0,2}$ variation, in Figure (a) and Figure (b), respectively.
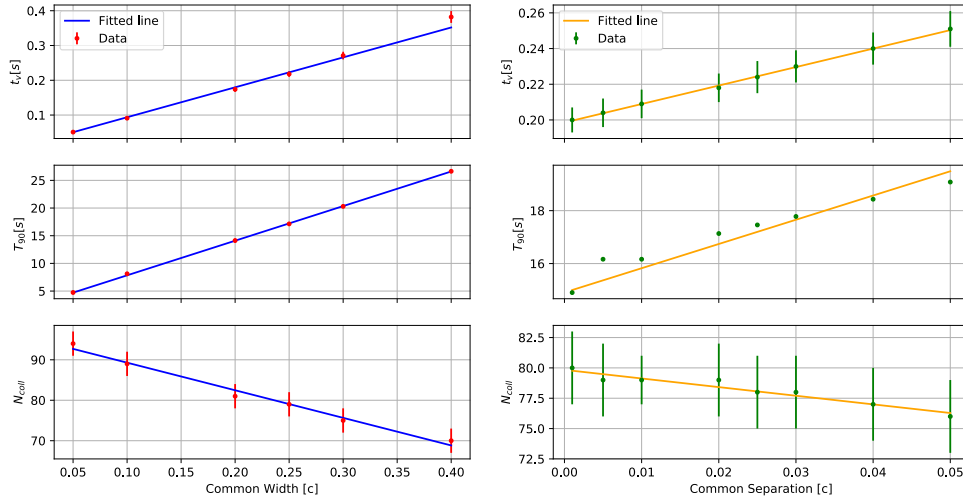
Figure 4.11. Variability time t_v, burst duration T_{90} and number of collisions N_{coll} (from top to bottom, respectively) as a function of the initial shells common width (left) and of the initial shells common separation (right).
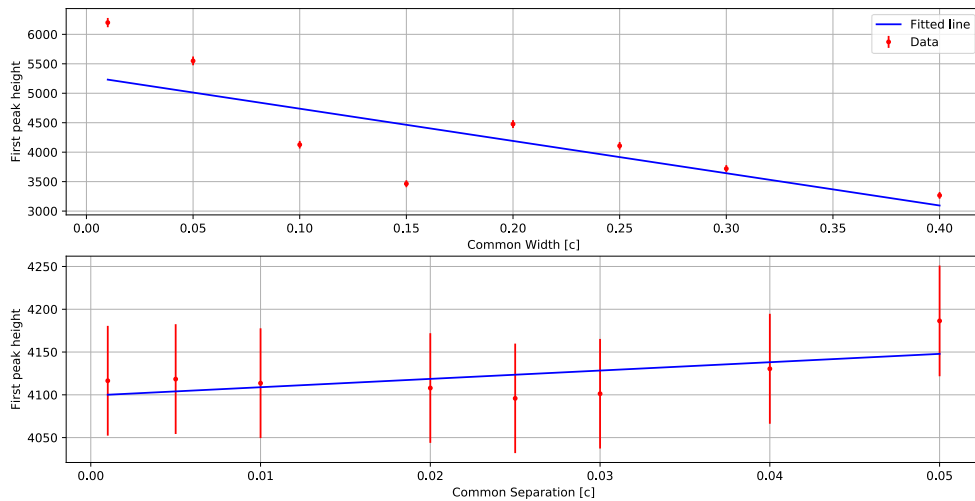
Figure 4.12. Height of the first peak A_1 as a function of the initial shells common width (top) and of the initial shells common separation (bottom).
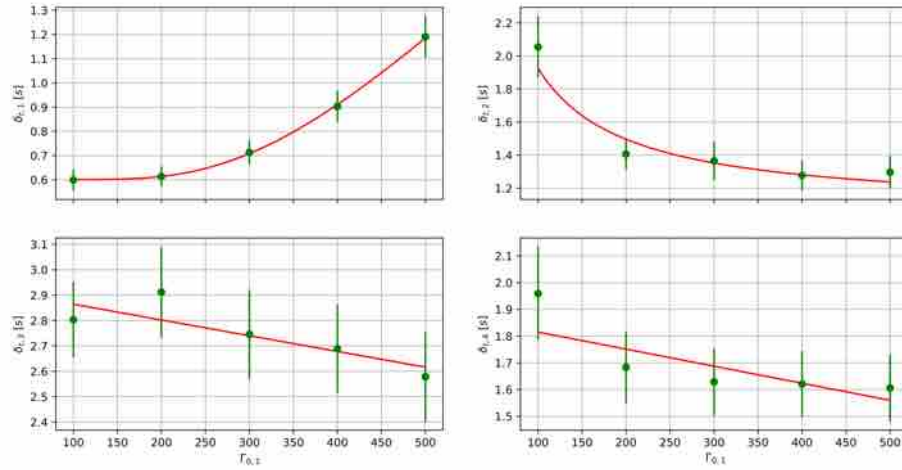
(a)
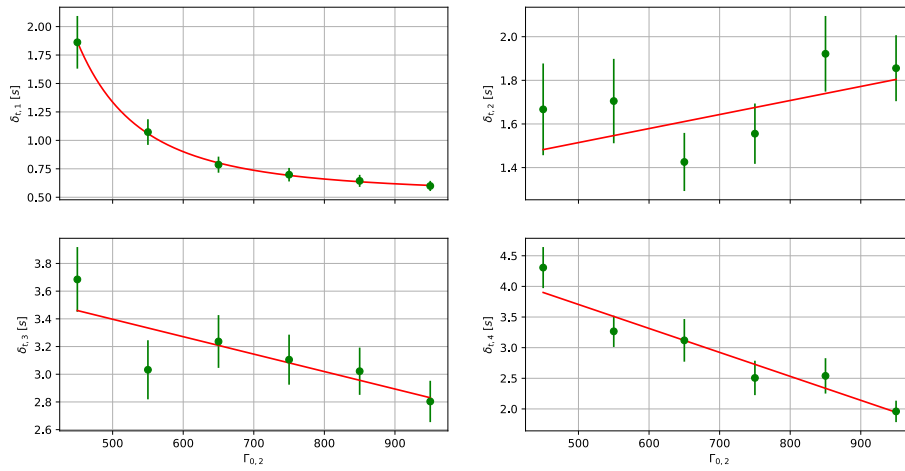
(b)

Figure 4.13. Pulses width δt_k, with $1 \leq k \leq 4$, as a function of the first shell Lorentz factor $\Gamma_{0,1}$ and the second shell Lorentz factor $\Gamma_{0,2}$ variation, in Figure(a) and Figure(b), respectively.
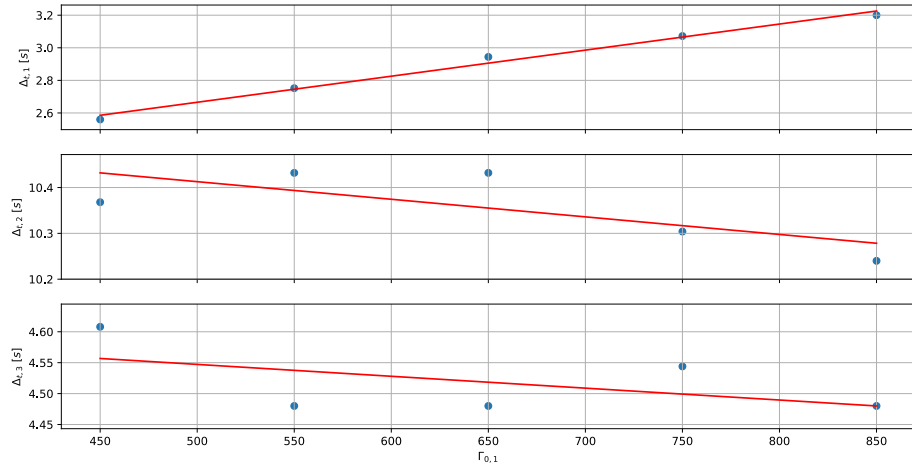
(a)
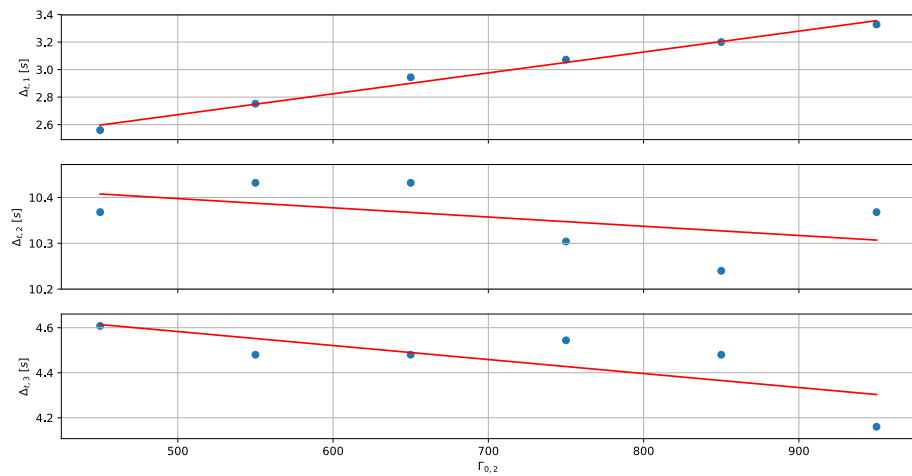
(b)

Figure 4.14. Pulses width Δt_k, with $1 \leq k \leq 4$, as a function of the first shell Lorentz factor $\Gamma_{0,1}$ and the second shell Lorentz factor $\Gamma_{0,2}$ variation, in Figure(a) and Figure(b), respectively.
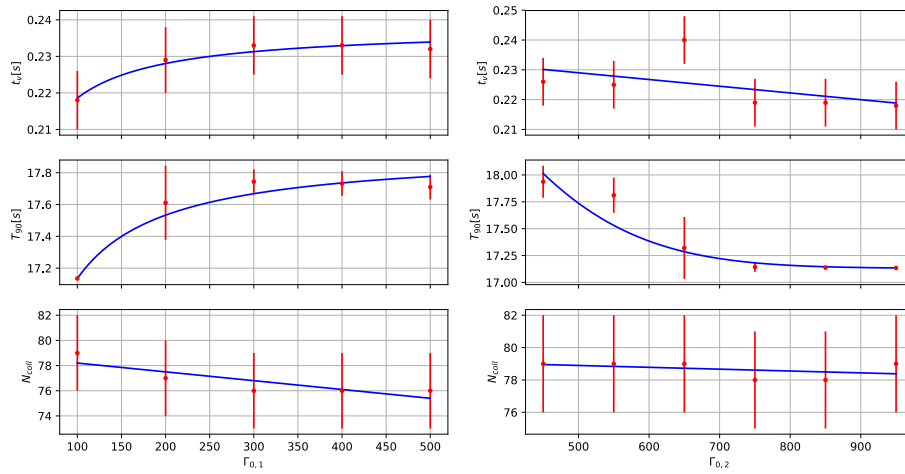
Figure 4.15. Variability time t_v, burst duration T_{90} and number of collisions N_{coll} (from top to bottom, respectively) as a function of the first shell Lorentz factor $\Gamma_{0,1}$ (left) and of the second shell Lorentz factor $\Gamma_{0,2}$ variation.

These results could provide help to adjust the input parameters in the NeuCosmA code, or also in other simulations, if a certain simulated light curve is to be reproduced. They also help understanding how these characteristic parameters of GRBs influence the light curves that are observed in various experiments and, therefore, how the central engine of these astrophysical objects could work.

Chapter 5

Hilbert-Huang transformation: a novel approach for GRB light curves

An innovative method, recently proposed, to study GRB light curves consists into the introduction of the Hilbert-Huang transformation (HHT) on observed data, as it results particularly suitable for non-linear and non-stationary time series. This is the reason for which one of the main requests in the GRB selection procedure was that this was characterized by non-linear and non-stationary data (Section 4.1).

Such a method was proposed for the first time twenty years ago by Huang et al. [76] and it has been using in different and multidisciplinary contexts. However, only recently it was applied to GRB light curves study, in that timing studies are considered a powerful tool to understand the emission mechanism regulating of the prompt emission of the GRB and its variability, given the lack of direct observations of the inner engine.

The *Fourier spectral analysis* has been a generally adopted technique for examining the energy-frequency distributions for many years, however its application are restricted to those cases when the time series is stationary and linear, which is not the case for GRBs [36]; thus, the Hilbert-Huang transformation is a powerful alternative in the context of GRBs.

The HHT consists of two parts:

1. The signal decomposition in its individual oscillatory modes, also called Empirical Mode Decomposition (EMD);

2. The spectral analysis through a method that applies the Hilbert transform, also called the Hilbert Spectral Analysis (HSA).

5.1 Empirical Mode Decomposition

The EMD, in contrast to most of the earlier methods, works in temporal space directly rather than in the corresponding frequency space. It consists in the signal decomposition within the individual modes embedded in the data, as it is assumed that any data consists of different simple intrinsic modes of oscillation. Each

component is defined as an Intrinsic Mode Function (IMF), which are required to satisfy the following conditions:

- In the whole data set, the number of extrema and the number of zero crossings must either be equal or differ at most by one;

- At any data point, the mean value of the envelope defined by the local maxima and the one defined by the local minima is zero.

With this definition it is thus possible to decompose any function through a *sifting process*, generating a certain number of IMFs, starting from the highest frequency component embedded in the original signal up to the lowest frequency one. The sifting process is defined by the following steps:

1. Compute a mean envelope $m_1(t)$ of the signal $s(t)$;

2. Consider the residue $h_1(t) = s(t) - m_1(t)$;

3. If $h_1(t)$ respects the IMF characteristics, it is an IMF; else, treat $h_1(t)$ (with its extrema) as a new signal to obtain $h_{1,1}(t)$ in the same way just described;

4. Continue the process as long as $h_{1,k}(t) = h_{1,k-1}(t) - m_{1,k}(t)$ is found to be an IMF. When the first IMF is found, denote it by $c_1(t)$.

5. Set $r_1(t) = s(t) - c_1(t)$ and repeat the sifting procedure on $r_1(t)$.

An illustration of this process is shown in Figure 5.1. However, the sifting process should be applied with care. To guarantee that the IMF components retain enough physical sense, the stop criterion for the sifting process and boundary conditions play a very important role [76] [123]. This topic will be better discussed in the following Sections.

5.2 Hilbert Spectral Analysis

After applying the EMD, the Hilbert transform is applied to each IMF to construct the energy-frequency-time distribution, the so-called *Hilbert spectrum*, where the time localities of events are preserved. In other words, instantaneous frequency and energy are provided rather than the global frequency and energy as defined by the Fourier spectral analysis. Indeed, IMFs represent a generalized Fourier expansion with variable amplitude and frequency.
Consider an analytic signal and its decomposition into a real and an imaginary components:

$$x_a(t) = x(t) + i\hat{x}(t), \tag{5.1}$$

where $x(t)$ is the real part, while the imaginary part $\hat{x}(t)$ is the Hilbert transform, which can be also expressed as:

$$x_a(t) = a(t)e^{i\theta(t)}, \tag{5.2}$$

in which the *instantaneous amplitude*

$$a(t) = \sqrt{x^2(t) + \hat{x}^2(t)}, \tag{5.3}$$
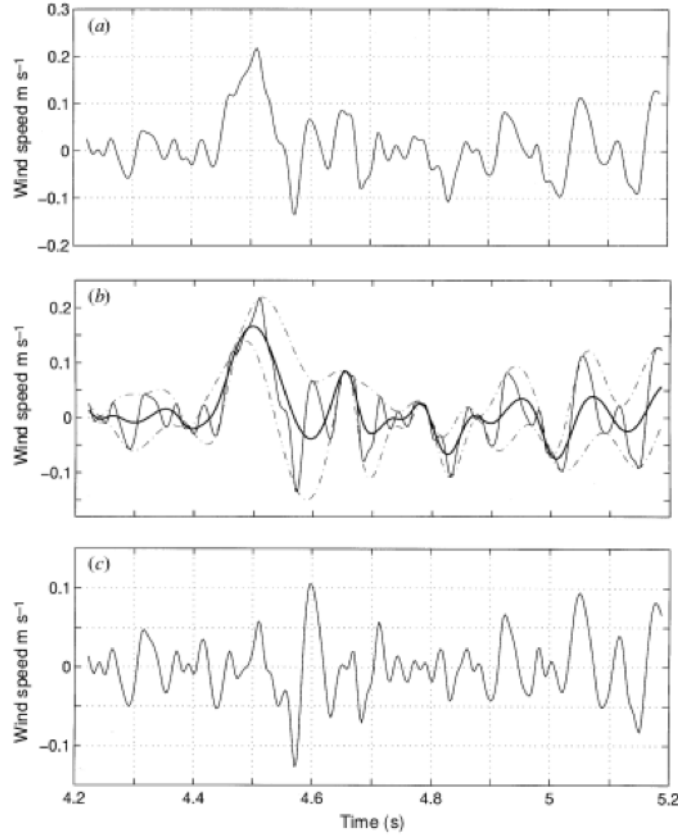
Figure 5.1. Illustration of the sifting process. First panel (a): original data; second panel
(b): the data in thin solid line, with the upper and lower envelopes in dot-dashed lines
and the mean in thick solid line; third panel (c): the difference between the data and m_1.
This is still not an IMF, because there are negative local maxima and positive minima
suggesting riding waves. Figure from [76].

and the *instantaneous phase*

$$\theta(t) = \arctan\left(\frac{\hat{x}(t)}{x(t)}\right), \tag{5.4}$$

appear. From these quantities it is possible to calculate the *instantaneous frequency*
in the following way:

$$\nu_{\text{inst}} = \frac{1}{2\pi}\frac{\mathrm{d}}{\mathrm{d}t}\theta(t). \tag{5.5}$$

The amplitude in Equation 5.3 and the instantaneous frequency in Equation 5.5
can be represented as a function of time in a three dimensional plot in which the
amplitude can be contoured on the frequency-time plane, obtaining the Hilbert
spectrum.

The combination of the EMD method and the associated Hilbert spectral anal-
ysis could offer a powerful method for non linear and non stationary data analysis;
thus, the idea of this work is to apply the method to GRB 110918A as well as to

the simulated GRB light curve in order to characterize the observed GRBs based on the results of this analysis.

5.3 HHT application

The application of the Hilbert-Huang transform has been possible through the Python module PyHHT[1], which implements the steps explained before to decompose the signal in several IMFs.

As anticipated in Section 5.1, the choice of stopping criteria and boundary conditions is particularly relevant in the context of the application of EMD, in that:

- Sifting too many steps may lead to loss of amplitude variation and physical meaning of the IMF;

- The influence of the ends might propagate into the data range of the low frequency component (which is the most interesting one because it is expected that the prompt emission is mainly described by the low frequency IMFs [37]).

Stopping criterion

The stopping criteria used in PyHHT is derived from the so-called *Amplitude ratio stop criteria* [108], instead of condition introduced by Huang [76], in which a standard deviation (SD) from two consecutive results in the sifting process is evaluated and the sifting process is stopped when SD is smaller than a predetermined value (usually 0.2-0.3). On the other hand, the Amplitude ratio stop criteria represents an improved implementation of the EMD [123] compared to the use of the SD. Its application involves the following steps:

1. Find the upper envelope $U(t)$ and lower envelope $L(t)$ of the signal;

2. Introduce the mode amplitude $a(t) = [U(t) - L(t)]/2$;

3. Calculate the evaluation function $\sigma(t) = |m(t)/a(t)|$, where $m(t)$ is the mean envelope;

4. The sifting is stopped when $\sigma(t) < \theta_1$ for some prescribed fraction $(1 - \alpha)$ of the total duration and $\sigma(t) < \theta_2$ for the remaining fraction. Therefore, if the amplitude of the mean envelope is relatively small compared with the amplitude of the corresponding IMF at all data points, then the sifting process is stopped.

In the PyHHT module the typical values for this stopping criterion used are: $\alpha = 0.05$, $\theta_1 = 0.05$ and $\theta_2 = 10\theta_1$ [123]. Furthermore, the idea of the amplitude ratio stop criteria are implemented through the B-spline algorithm, which evaluates the mean envelope without evaluating $U(t)$ and $L(t)$, producing similar results to those obtained calculating them [45].

---

[1]Tutorial avalaible in `https://pyhht.readthedocs.io/en/latest/tutorials.html`.

Boundary conditions

The boundary conditions are particularly important too; if a wrong prediction is made at the first IMF, the whole signal will be decomposed incorrectly and the EMD will be not correct as well. So it is essential to choose a proper boundary extension of the signal at every step. Due to the finite length of the signal, before using B-splines to find the mean envelope, the extrema have to be extended. The general method, used in the PyHHT package, consists into the addition of the extrema by mirror symmetry with respect to the end points or with respect to the extrema which are closest to the end points.

5.3.1 EMD stability

In order to draw consistent conclusions on the signal mode content with the HHT, in particular with the stopping criterion and boundary conditions as previously introduced and implemented through in the PyHHT code, its stability with respect to different transformations has been investigated, namely:

- **Translation**: the light curve is shifted along the temporal axis. As a consequence, it results that the IMFs are only shifted (Figure 5.3);

- **Addition of a constant factor**: the light curve is shifted up by a constant factor. The results are stable, , since the transformation only appears, as expected, in the residue (Figure 5.4);

- **Addition of random fluctuations**: random fluctuations are added to the signal, resulting into major variations of the EMD obtained.

The latter transformation is the only one producing relevant modifications to the EMD. It was obtained considering for each temporal interval that constitutes the signal random fluctuations overlaid to the real signal c_{obs}, according to:

$$c_{\text{random}} = c_{\text{obs}} + \sqrt{c_{\text{obs}}} \cdot x, \tag{5.6}$$

where x is a random number from a normal distribution $G(\mu, \sigma)$ with mean μ and standard deviation σ, extracted for each temporal bin. Two cases have been analyzed: $\sigma = 1$ and $\sigma = 0.1$, with $\mu = 0$ anyhow. As a consequence of this procedure, the initial signal is polluted by random fluctuations which are allowed to vary within one standard deviation. Formally, the whole signal is allowed either to over-fluctuate or under-fluctuate by at most one statistical deviance. The EMD technique is later applied to the realization consisting of the original signal and the random fluctuation. The procedure is then repeated several times in order to investigate different amplitude of the fluctuations. An example for the results obtained in the case of $G(0, 1)$ is shown in Figure 5.5: it is clear that only the first IMFs are similar to each other, while the most relevant ones appear to be the most unstable. Even if smaller fluctuations are considered, extracting x in Equation 5.6 by $G(0, 0.1)$, instabilities are present (see Figure 5.6). In addition, to this first problem, it can be noted that the number of extracted IMFs in the two cases is different and that the residue (the last IMF) is not only a trend (a monotonic function from which no more IMF can be extracted), as expected [76], but it still shows an oscillatory behavior.

Clearly, the application of the Empirical Mode Decomposition as implemented in the PyHHT package presents some issues, which require further investigation. For instance, in the following, a different strategy is implemented in the boundary condition setting.

Ratio Boundary Extension

Given the strong influence of boundary conditions on the EMD results, the PyHHT code has been changed to implement new boundary conditions following the so-called *Ratio Boundary Extension* [123]:

1. Find the locations of the last three maximum points of the signal, τ_{-3}, τ_{-2} and τ_{-1}.

2. Calculate the ratio of the distance between the last three maximum points, $r_{\max} = (\tau_{-1} - \tau_{-2})/(\tau_{-2} - \tau_{-3})$.

3. Find the locations of the last three minimum points of the signal, η_{-3}, η_{-2} and η_{-1}.

4. Calculate the ratio of the distance between the last three minimum points, $r_{\min} = (\eta_{-1} - \eta_{-2})/(\eta_{-2} - \eta_{-3})$.

5. Calculate the mean ratio $r = (r_{\max} + r_{\min})/2$.

6. Find the location of the first extended maximum τ_1, such that $r = (\tau_1 - \tau_{-1})/(\tau_{-1} - \tau_{-2})$, and the location of the first extended minimum η_1, such that $r = (\eta_1 - \eta_{-1})/(\eta_{-1} - \eta_{-2})$

7. Quadratic interpolation on the last three maxima and on the last three minima of the given signal.

8. Calculate the first extended maximum and minimum using the quadratic function.

The same idea is then applied to estimate the location and values of the second extended maximum points and two extended minimum points.

The difference between the mirror symmetry extension and the ratio extension is shown in Figure 5.2: by using a symmetric extension the data do not give the proper prediction of he original signal, unlike the ratio extension, which should be advantageous. In Figures 5.7a and 5.7b the results of the EMD on GRB 110918A obtained with the original B-spline method and with the modified one are shown, respectively. The latter produces a residue which is no more oscillating as in the former case. The Hilbert spectrum of each IMF obtained after the EMD application with the ratio boundary extension is also shown (Figure 5.8). However, repeating the procedure described above with the new boundary conditions, the issue concerning the method instability towards transformations that include random fluctuations is still present. Indeed, Figure 5.9 shows an example with random fluctuations extracted from a normal distribution with standard deviation $\sigma = 1$ and the corresponding EMD, where the Ratio Boundary Extension was applied. The differences between the IMFs appear especially in the initial part, in correspondence of the dominant

peak in the light curve. One can therefore suppose that the EMD can only be applied to signals where the peak heights are not that different but further studies would be needed to draw more precise conclusions.

(a)

(b)

(c)

(d)
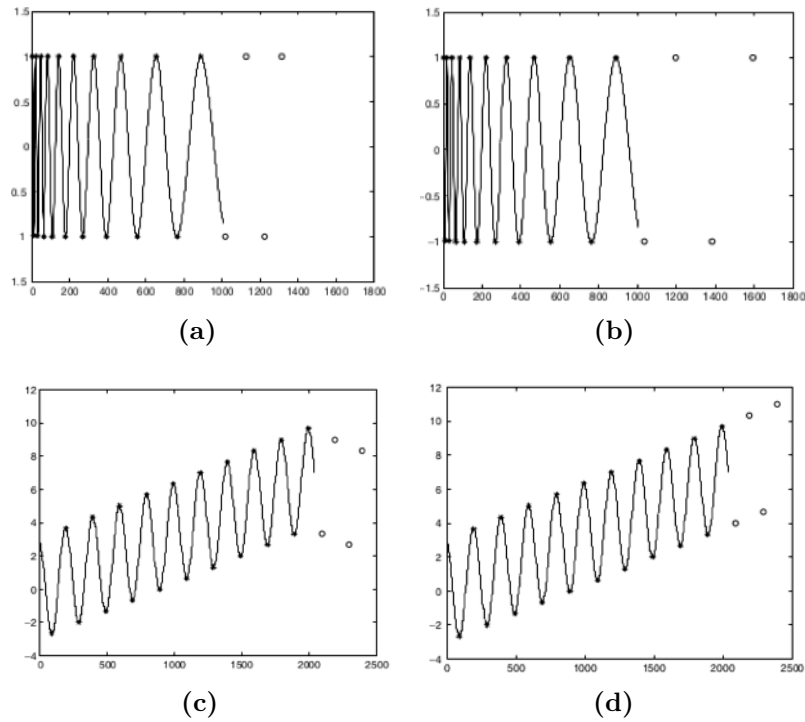
Figure 5.2. Figures (a) and (b): Frequency modulated signal. The circles denote the extended extrema with in (a) the mirror simmetry extension and in (b) the ratio extension. Figures (c) and (d): Signal with one sinusoid and one straight line residue. The circles denote the extended extrema with in (c) the mirror simmetry extension and in (d) the ratio extension. Figures from [123].
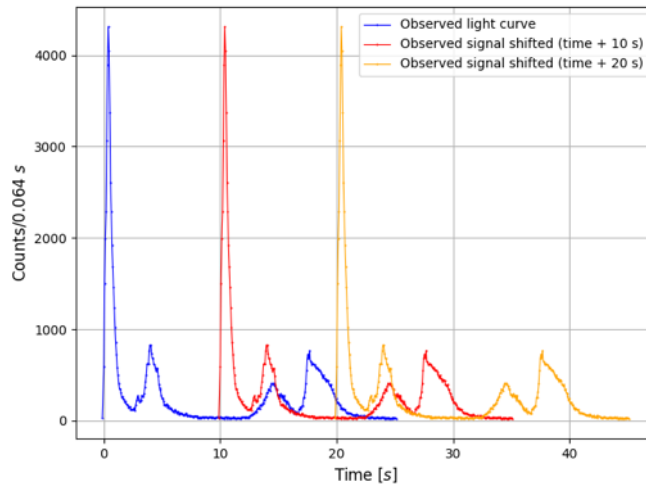
(a)
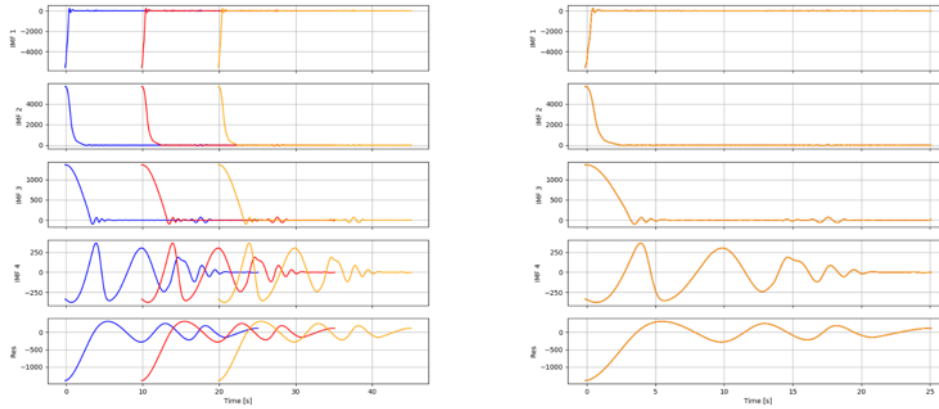
(b)   (c)

Figure 5.3. Figure (a): Observed Konus-WIND light curve of GRB 110918A (in blue) and original light curve shifted by 10 s (in red) and 20 s (in orange). Figure (b): Empirical Mode Decomposition results. Figure (c): same as Figure (b), with all the IMF shifted to the left in order for them to start all from t=0 s.
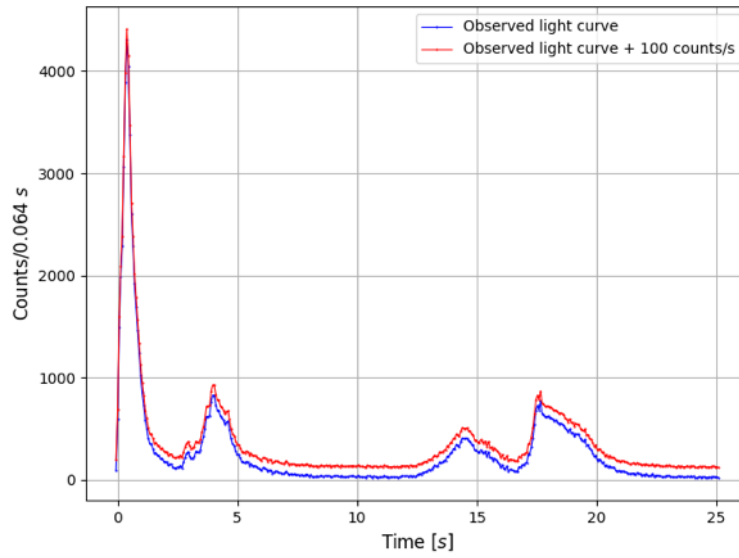
(a)
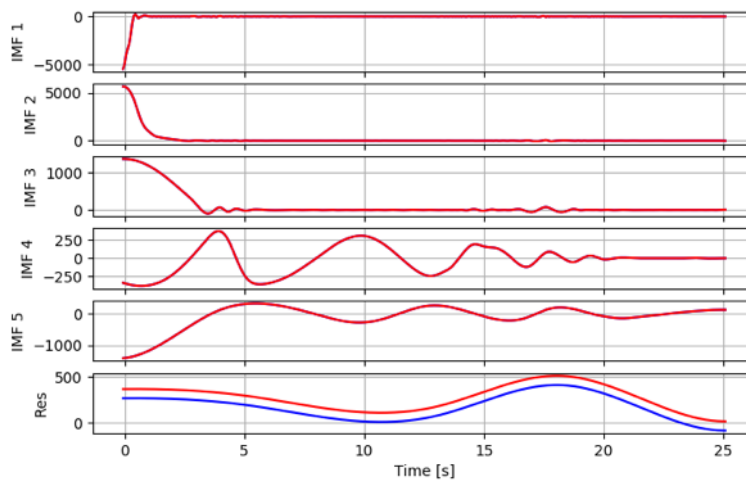
(b)

Figure 5.4. Figure (a): Konus-WIND light curve of GRB 110918A (in blue) and original light curve with the addition of 100 counts/s (red). Figure (b): Empirical Mode Decomposition results.

(a)

(b)

(c)
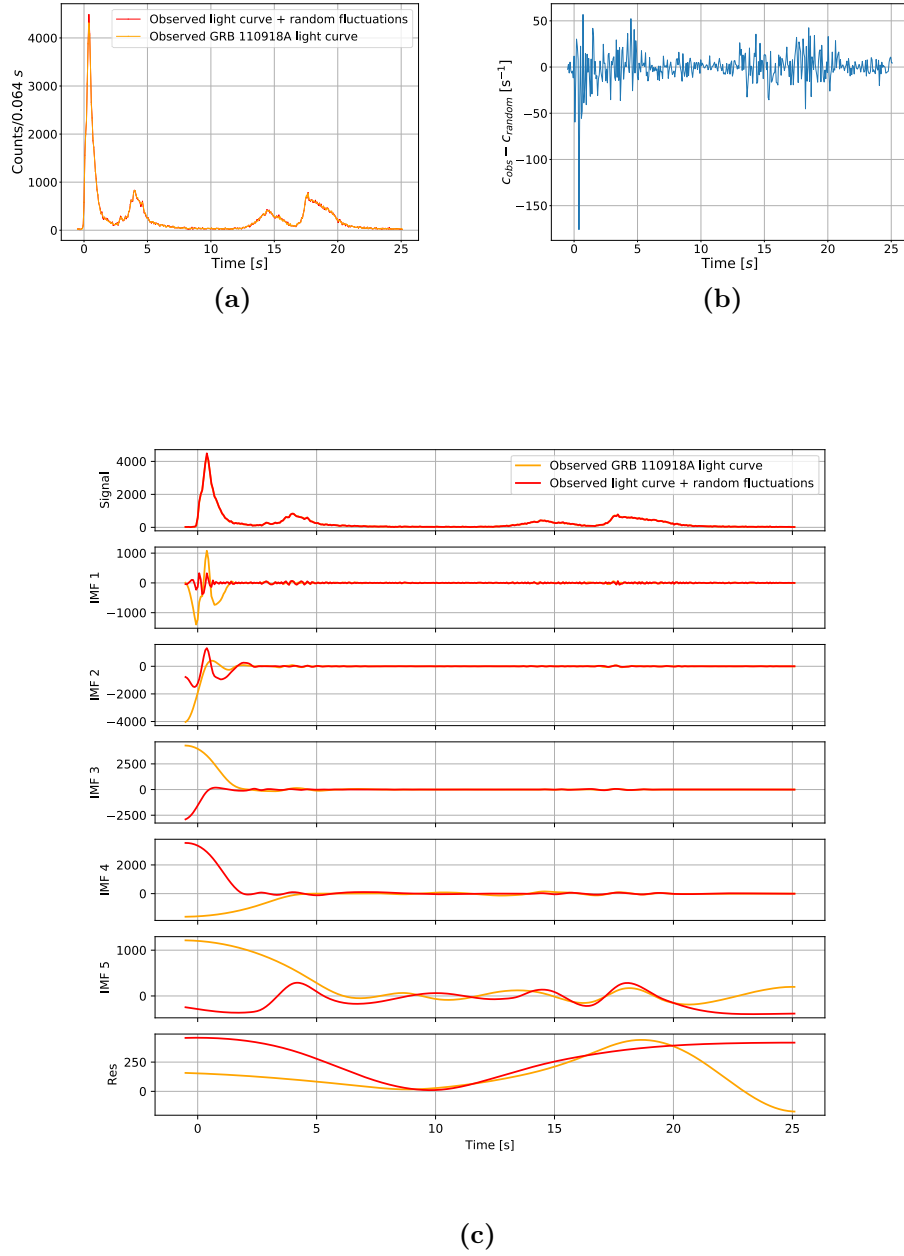
Figure 5.5. Figure (a): Observed Konus-WIND light curve signal c_{obs} of GRB 110918A (in red) and signal with random fluctuations c_{random} (in orange), calculated as in Equation 5.6 by $G(0,1)$. Figure (b): Difference between c_{obs} and c_{random}. Figure (c): Empirical Model Decomposition applied on c_{obs} (in red) and on c_{random} (in orange).

(a)

(b)
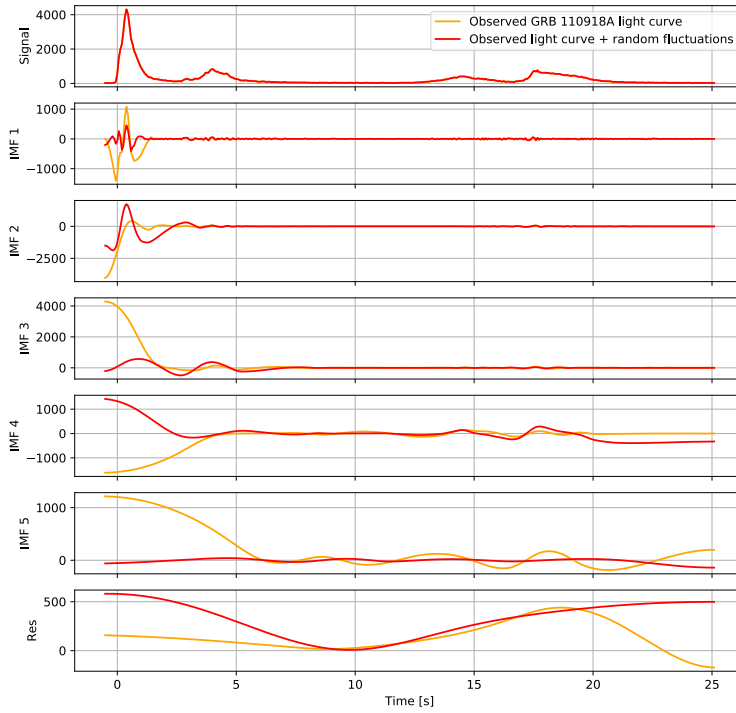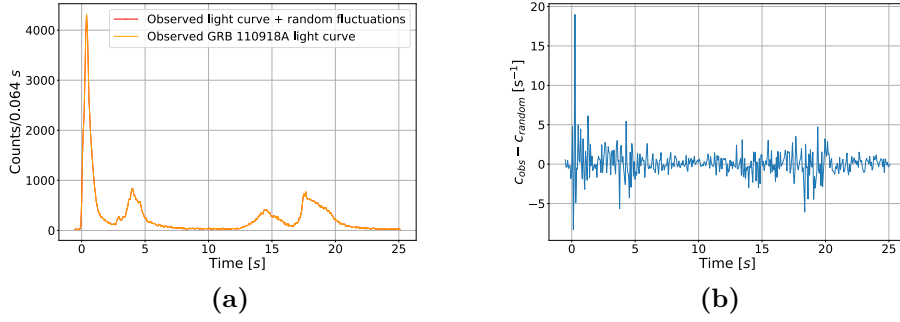
(c)

Figure 5.6. Figure (a): Observed Konus-WIND light curve signal c_{obs} of GRB 110918A (in red) and signal with random fluctuations c_{random} (in orange), calculated as in Equation 5.6 by $G(0, 0.1)$. Figure (b): Difference between c_{obs} and c_{random}. Figure (c): Empirical Model Decomposition applied on c_{obs} (in red) and on c_{random} (in orange).
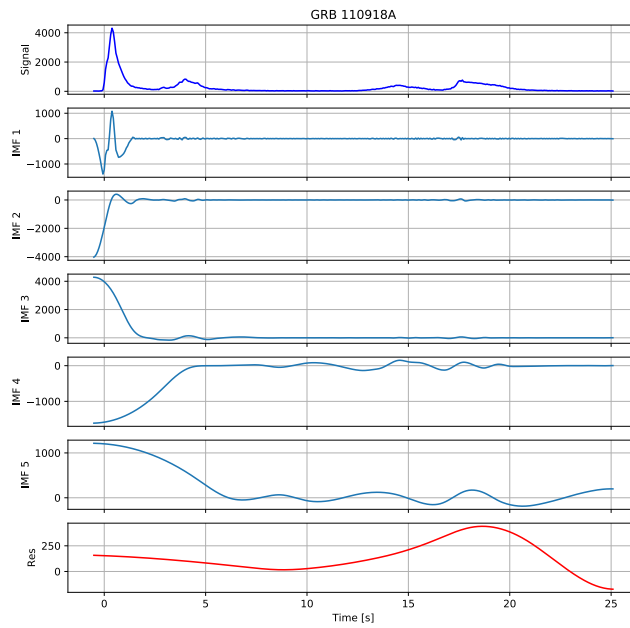
(a)
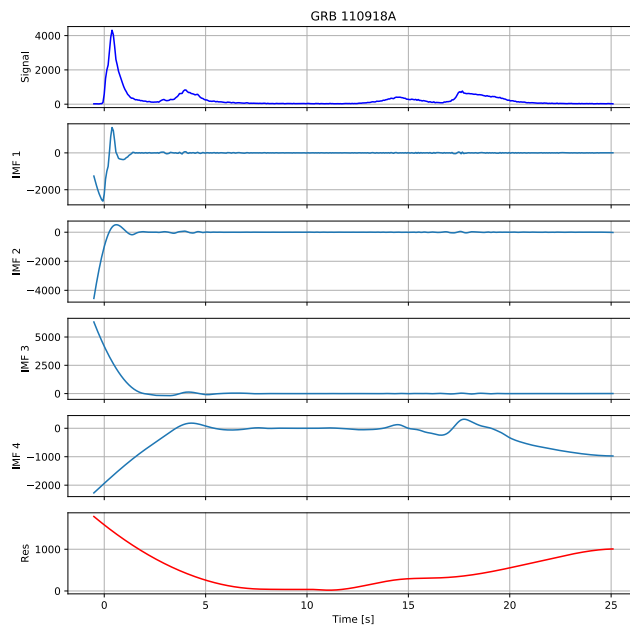
(b)

Figure 5.7. Figure (a): Empirical Mode Decomposition on Konus-WIND light curve of GRB 110918A with the original B-spline method. Figure (b): Empirical Mode Decomposition on Konus-WIND light curve of GRB 110918A with the modified B-spline method with ratio boundary extension.
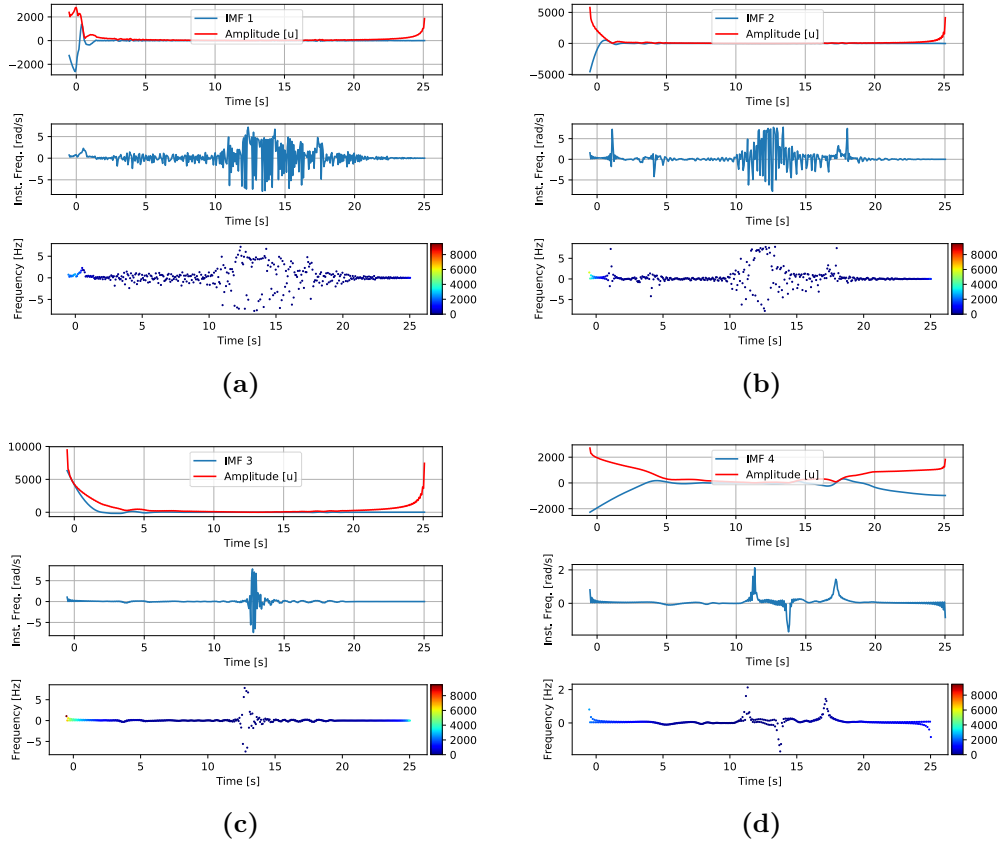
Figure 5.8. Hilbert-Huang transform application on the Konus-WIND light curve of GRB 110918A, by using the ratio boundary extension in the EMD. From Figure (a) to Figure (d): first, second, third and fourth IMF. In each Figure, first panel: the signal of the IMF (in blue) and its amplitude (in red) from Equation 5.3; second panel: the instantaneous frequency from Equation 5.5 as a function of time; third panel: Hilbert spectrum (instantaneous frequency as a function of time with the amplitude expressed as a 3D-dimension). The values used for the coloured bar go from the minimum amplitude to the maximum one between the values obtained for all the IMFs.

(a)

(b)

(c)
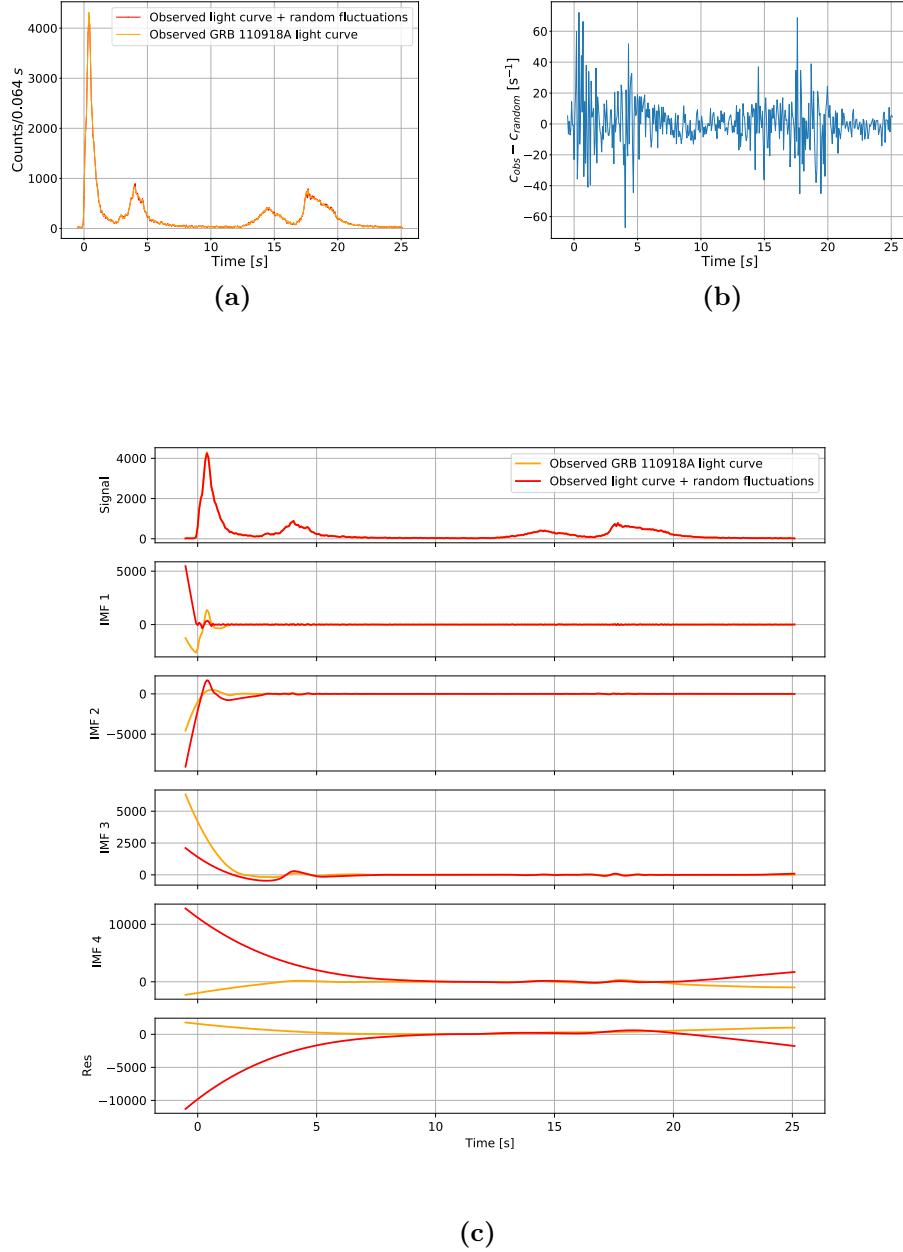
Figure 5.9. Figure (a): Observed Konus-WIND light curve signal c_{obs} of GRB 110918A (in red) and signal with random fluctuations c_{random} (in orange), calculated as in Equation 5.6 by $G(0,1)$. Figure (b): Difference between c_{obs} and c_{random}. Figure (c): Empirical Model Decomposition (with the Ratio Boundary Extension) applied on c_{obs} (in red) and on c_{random} (in orange).

5.3.2 EMD on simulated light curve

As previously anticipated, the initial idea was to compare results of the EMD applied on the observed GRB light curve and on the simulated one through the NeuCosmA code. Then, after applying such decomposition on GRB 110918A, the same procedure has been used for the simulated light curve. See Section 4 for its characteristics and for the procedure with which it has been obtained.

(a) **(b)**
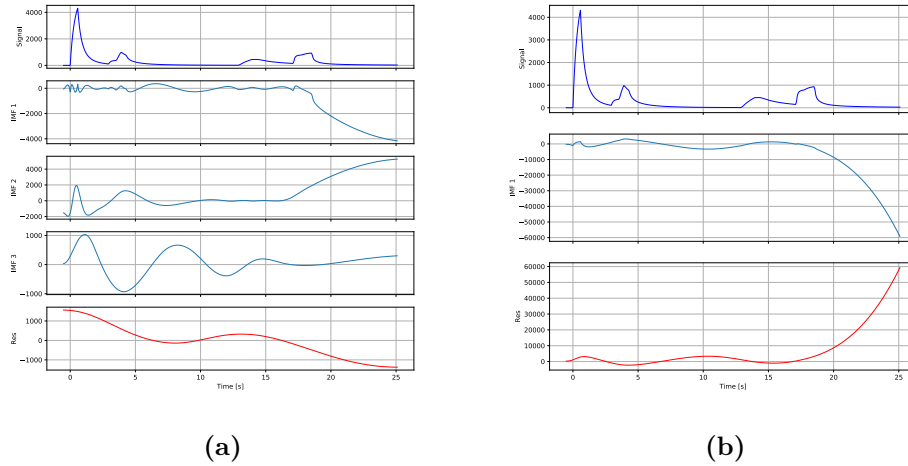
Figure 5.10. Figure (a): Empirical Mode Decomposition on the simulated GRB light curve with the original B-spline method. Figure (b): Empirical Mode Decomposition on the simulated GRB light curve with the modified B-spline method with ratio boundary extension.

Figure 5.10 shows that both by using the mirror symmetry extension and the ratio extension, it has been not possible to reproduce the same number of IMFs in Figure 5.7 for comparing simulated and observed light curve. Even applying of the EMD with the ratio boundary extension, only one IMF has been extracted and this seems to be an artificial result.

Chapter 6

High-energy neutrino flux prediction for GRB 110918A in a multi-collision zone model

In this Chapter the neutrino flux obtained from the simulated GRB light curve with the NeuCosmA code is presented, in order to provide an estimate of the energy released into neutrinos from GRB 110918A in the context of a multi-collision model (see Section 4.4 for the difference with the one-zone approach) and of the number of events potentially observable by the ANTARES neutrino telescope (presented in Chapter 3).

6.1   Previous results in the one-collision zone model

GRB 110918A has already been targeted for neutrino studies by the ANTARES Collaboration [20]. This source, in fact, was considered a very promising candidate for a neutrino search with the ANTARES detector given its proximity in redshift and its position at the trigger time (for more details see Section 4.2), namely its location at $\theta_z \simeq 92°$ implied that neutrinos had to travel up to the detector crossing the Earth quite horizontally, so that a negligible effect is expected to be connected with to the Earth-absorption (see Section 3.3.2). A search for muon neutrinos in spatial and temporal coincidence with the prompt emission of GRB 110918A was hence performed using the data of ANTARES neutrino telescope [20]. Two different analyses were considered, one optimized for the neutrino energies involved in the IS scenario and the other for those of the PH scenario (see Section 2.3.1). In both cases, no neutrino events have been observed in coincidence with the GRB. Therefore, a 90% confidence level (C.L.) upper limit on the expected muon energy neutrino flux $E_{\nu_\mu}^2 \phi_{\nu_\mu}$ was derived. The expected muon neutrino spectrum was evaluated by means of the standard one-zone collision NeuCosmA code using the set of measured gamma-ray parameters, namely the γ-ray fluence F_γ, the low- and high-energy spectral index α and β, the peak energy of a Band spectrum E_γ, the redshift z and the variability time t_v (see Chapter 4). For the remaining GRB parameters, which mainly concern the mechanism through which the jet kinetic energy is converted into internal energy and that cannot be directly inferred from
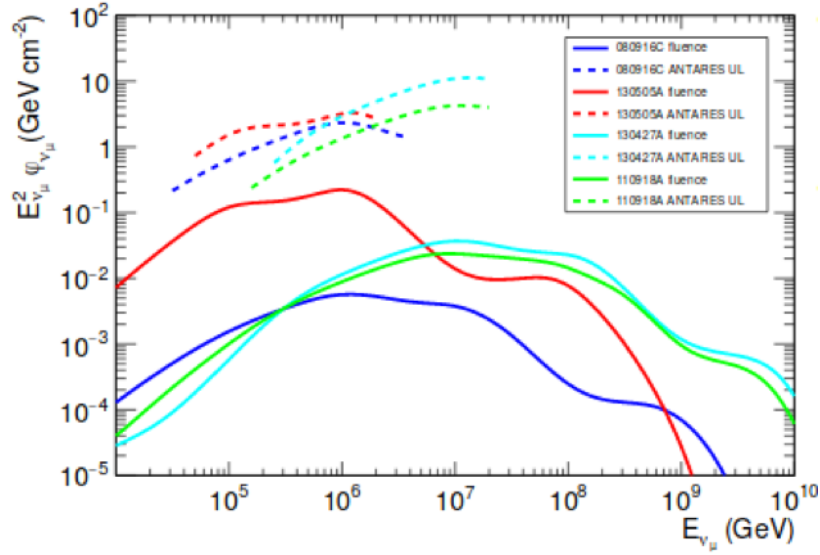
Figure 6.1. Expected $\nu_\mu + \bar{\nu}_\mu$ fluences (solid lines) for four bright GRBs (GRB 080916C, GRB 130505A, GRB 130427A, GRB 110918A) in the IS model prediction (NeuCosmA code) and ANTARES 90% C.L. upper limits on the GRBs, in the energy band where the 90% of the signal is expected to be detected by ANTARES. Results relative to the GRB 110918A, object of this analysis, are indicated in green. Figure from [20].

measurements, "standard values" widely accepted have been assumed. The expected neutrino flux for GRB 110918A and the 90% C.L. upper limit calculated by the ANTARES Collaboration are indicated in Figure 6.1 as a green solid and dashed line, respectively [20]. Assuming the expected signal flux from the NeuCosmA model and taking into account the data taking conditions and the detector response during the GRB episode, the number of expected signal μ_s from GRB 110918A in the ANTARES neutrino telescope was calculated too, through a standard Monte Carlo simulation, obtaining $\mu_s = 1.3 \times 10^{-2}$.

Starting from these results, in this work new estimates of the neutrino expected flux as well as of the number of signal in ANTARES will be provided: both are expected to be more realistic than previous evaluations because of the introduction of multi-zone approach.

6.2 Results in the multi-collision zone model

As introduced in Chapter 4, the NeuCosmA code simulates the evolution of the GRB jet in the internal shock scenario of the fireball model, by keeping track of all relativistic plasma shells that propagate in it, of the collisions between shells, and of the gamma rays, protons and neutrinos emitted at the shocks produced during the collisions. Unlike traditional one-zone model that extrapolates the behavior of the whole burst from a single representative collision, this multi-zone simulation considers many such collisions, each of which is realized under different physical conditions.

6.2.1 Neutrino, gamma-ray and UHECR production[1]

NeuCosmA considers the possibility that GRBs contribute to the UHECR flux observed as dominant sources. Consequently, particle escape from the acceleration site is investigated, providing hints for the way in which this process influeces the production of neutrinos [28]. Indeed, UHECRs are emitted via two mechanisms: either $p\gamma$ interaction transform protons into neutrons which freely escape the merged shell, and later beta-decay back into protons [97], or protons directly leak out of the shell without interacting. The latter situation happens when the proton Larmor radius exceeds the shell width, as it is most likely at the highest energies [28].
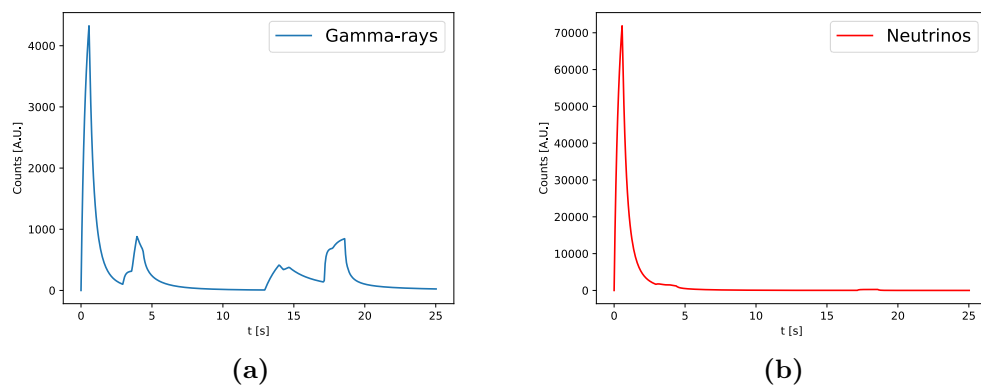
Figure 6.2. Simulated gamma-rays and neutrino light curves, in Figure (a) and Figure (b) respectively, through the NeuCosmA code, within the multi-collision zone model, for the GRB under exam.

A novel aspect of the multi-collision NeuCosmA simulation is the fact that, by recording the production site of gamma rays and neutrinos, it is also possible to derive a light curve for neutrino emissions from the source. Even though the detection of such a light curve is far from the reach of current neutrino telescopes, it appears extremely interesting to investigate its shape, and compare it to the electromagnetic counterpart. In fact, this encloses the information on the source region where neutrinos are produced. In Figure 6.2 the neutrino light curve for collisions beyond the photosphere, compared to the relative gamma-rays light curve, is shown. This light curve shows a smooth trend, which averages out the variability present in the corresponding gamma-ray light curve. Neutrinos are produced mainly in the first burst, within the first ~ 3 s of duration of the GRB. Their production is associated with an optically thick collision (namely the first collision beyond the photosphere), in which the dominant UHECR component is neutron escape (Figure 6.3). The subsequent collisions, in which instead the dominant component is direct proton escape, are characterized by very low values of optical depth $\tau_{p\gamma}$. However, there are too few optically thick collisions, which means that, except for the first seconds, a

---

[1]The plots presented in this Section have been reproduced for the simulated GRB light curve yielding the best χ^2-test result (with respect to the observed light curve) among all the 500 simulations, i.e. $\chi^2/\nu = 660$.
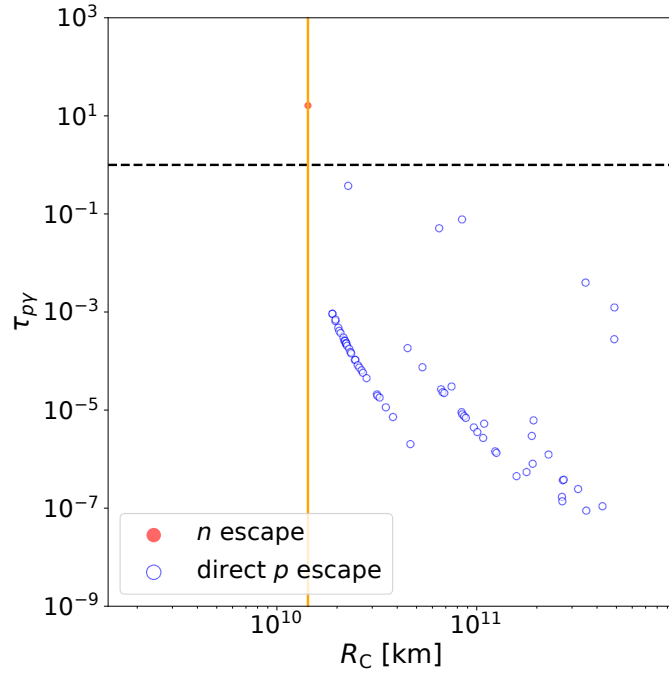
Figure 6.3. Optical depth $\tau_{p\gamma}$ for all collisions, in the GRB simulation as a function of collision radius R_C. The dashed horizontal line corresponds to $\tau_{p\gamma} = 1$. The vertical line indicates the photosheric radius. The red filled dot is a super-photospheric collision where the dominant UHECR component is neutron escape, and blue unfilled dots are super-photospheric collisions where the dominant component is direct proton escape.
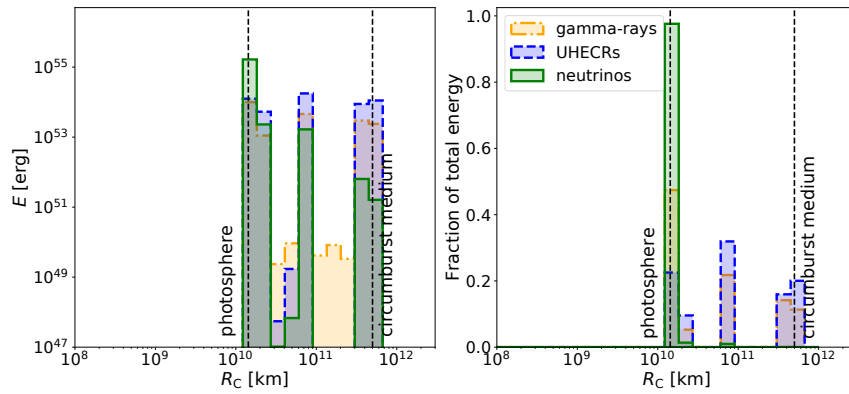
Figure 6.4. Energy E (left) and fraction of the total energy (right) as a function of collision radius R_C in neutrinos (green), UHECR protons with $E_p > 10^{10}$ GeV (blue), and gamma rays (orange). The approximate photospheric and circumburst radius are marked.

very low neutrino flux is expected to be produced. This results is in agreement with previous estimates where the neutrino production associated to neutron escape was found to be higher than that associated to direct proton escape [97]. Furthermore, from Figure 6.4, it is clear that neutrinos predominantly come mainly from regions close to the center while UHECR protons come mainly from intermediate regions [43]. The fraction of the total energy emitted as gamma-rays $E_{\gamma,\text{tot}}^{\text{iso}}$, as protons $E_{\text{p,tot}}^{\text{iso}}$

and as neutrinos $E_{\nu,\mathrm{tot}}^{\mathrm{iso}}$ is the 68%, 22% and 10%, respectively.

6.2.2 Neutrino flux estimation

For the first time, a multi-collision neutrino flux prediction for a real GRB is presented. The neutrino Spectral Energy Density (SED) $E_{\nu_\mu}^2 \phi_{\nu_\mu}$[2] allows to easily appreciate any spectral deviation from the simple power law $E_{\nu_\mu}^{-2}$. The simulated neutrino flux does not contain contributions from sub-photospheric collisions, then it comes from beyond the photosphere, like the observed gamma rays. Such flux is compared, in Figure 6.5, both with the expected $\nu_\mu + \bar{\nu}_\mu$ fluence for GRB 110918A estimated with the one-zone prediction in [20] and with a new one-zone estimate. Indeed, the novel release of NeuCosmA also performs a classical one-zone simulation using as input parameters average values over their interval of variability, as derived through the multi-zone simulation. Results obtained as average over 500 simulations are presented. The expected neutrino fluence is normalized to the known value of the isotropic equivalent $E_{\mathrm{iso}} = (2.1 \pm 0.1) \times 10^{54}$ erg [57] for GRB 110918A, in order to reproduce the correct energetic conditions of this burst. The flux calculated with the multi-zone model appears lower than with the one-zone model, as expected from previous evaluations [57]. This happens because in the one-zone simulation all shells are assumed to have the same collisions radius and averaged values are used, overestimating the flux [43].

6.2.3 Expected neutrino signal in ANTARES

The number of expected muon neutrino signals in the ANTARES neutrino telescope (described in Chapter 3), can be calculated as:

$$\mu_s = \int dE_{\nu_\mu} A_{\mathrm{eff}} \phi_{\nu_\mu}, \tag{6.1}$$

where A_{eff} is the time-averaged effective area for neutrinos of the detector, E_{ν_μ} is the muon neutrino energy and ϕ_{ν_μ} represents the expected $\nu_\mu + \bar{\nu}_\mu$ fluence. The effective area changes with the declination band, since the detection capability of the instruments depends on the position of sources in the sky. For the specific declination area of the GRB 110918A ($\sim$- 27°) [57], the time-averaged effective area of the ANTARES neutrino telescope in the declination band -45° $< \delta <$ 0 ° was considered: it is shown as a function of the neutrino energy E_{ν_μ} in Figure 6.6. The integrand function in Equation 6.1, namely the product among the effective area and the neutrino fluence is the so-called parent energy distribution, and is illustrated as a function of the neutrino energy itself in Figure 6.7. The obtained signal event numbers are collected in Table 6.1, representing an average value calculated after 500 neutrino flux prediction from the NeuCosmA model. With respect to the previous one-zone model predictions ($\mu_s = 1.3 \times 10^{-2}$) [20], a smaller value is derived here: this is connected with the fact that the novel modeling accounts for the whole inner engine behavior, as dictated by the emitted light curve, and simplifies such

---

[2]Neutrino flux calculations are insensitive to the beaming effect caused by a narrow opening angle of the jet as all formulae contain the isotropic luminosity in conjunction with a 4π shell geometry, i.e. effectively use luminosity per steradian.
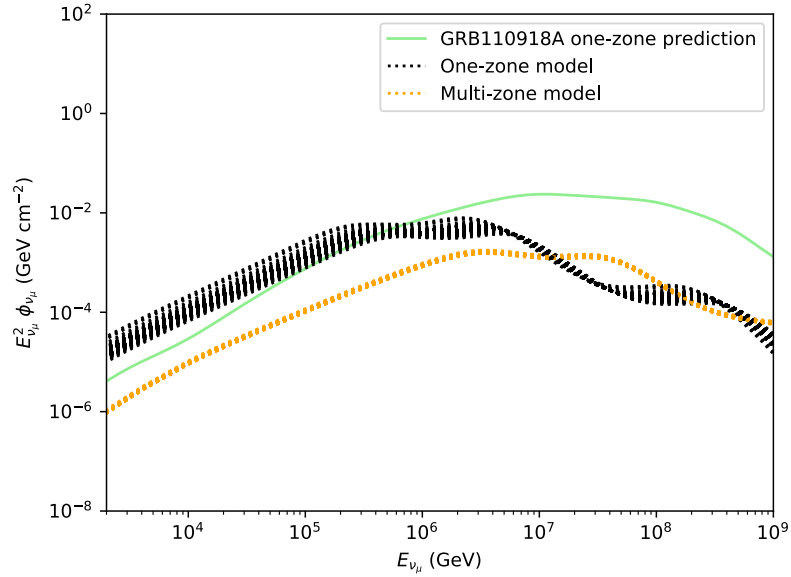
Figure 6.5. Expected $\nu_\mu + \bar{\nu}_\mu$ fluence for the GRB 110918A. Green solid line: former one-zone prediction, extracted from the gamma-ray spectrum [20]. Dashed black lines: one-zone prediction obtained from 500 complete light curve simulations performed using the NeuCosmA code. Dashed orange lines: multi-zone prediction obtained from 500 complete light curve simulations performed using the NeuCosmA code.

a description within a unique collision. The expected number of events is further reduced when accounting for the complete simulation chain of shell collisions: this result is well consistent with former predictions realized in the context of multi-zone collision models [57].
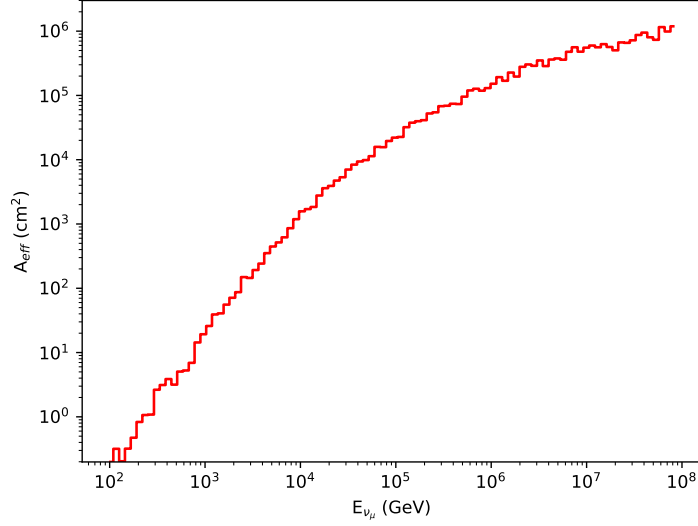
Figure 6.6. Effective area for neutrinos detection in ANTARES neutrino telescope as a function of the neutrino energy for the specific declination band of GRB 110918A, $-45° < \delta < 0$ °, optimized with the analysis cuts of the former analysis [20].
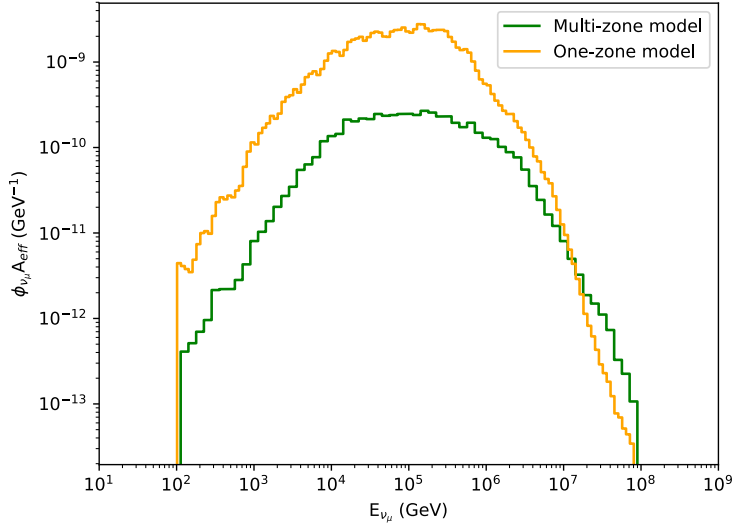
Figure 6.7. Time-averaged effective area A_{eff} multiplied by the expected $\nu_\mu + \bar{\nu}_\mu$ fluence for the GRB 110918A as a function of the neutrino energy E_{ν_μ}. The area under the curve represents the number of neutrinos expected to be detected in the band energy $[10^2\text{-}10^8]$ GeV.

	Multi-zone	One-zone
μ_s	6.1×10^{-4}	2.8×10^{-3}

Table 6.1. Expected number of signal events μ_s in the context of multi- and one-zone collision models, as predicted from the NeuCosmA model, taking into account the effective area of the ANTARES neutrino telescope.

Chapter 7

Summary and Conclusions

This work is focused on Gamma-Ray Bursts (GRBs), the most luminous objects in the Universe representing highly beamed sources of gamma rays and perhaps also of high energy neutrinos and cosmic rays. In the internal shock scenario, blobs of plasma emitted from a central engine are believed to collide within a relativistic jet and form shocks, responsible for the particle acceleration. Among all the possible astrophysical sources, GRBs, being transient and extremely energetic explosions, offer one of the most promising perspectives for the detection of cosmic neutrinos thanks to the almost background free search. Searching a temporal and spatial coincidence among the GRB prompt emission and high-energy neutrinos, using neutrino telescopes, is crucial to provide information about the acceleration mechanism in GRBs. Within relativistic outflows of material expelled from a central engine, electrons are thought to be accelerated in internal shocks, which serves to explain the gamma radiation that is observed at Earth. If protons are simultaneously accelerated in these outflows, their interactions with the local photon field would give rise to a flux of neutrinos that would accompany the electromagnetic signal. However, the detection of neutrino events would allow to identify these sources as hadronic accelerators and as candidates for UHECRs. Over the years, the IceCube and ANTARES Collaborations have been searching for neutrino signals coincident with GRBs in time and direction, which however have not been observed until now. Progressively deeper non-detection upper limits have been placed though current limits do not yet provide significant constraints on the validity of the internal shock model.

In this work the study of GRB 110918A is presented. It is the brightest long GRB detected by Konus-WIND (KW) during its observation years and the most luminous one observed until now: the high energy fluence measured by KW, $F_\gamma = 7.5 \times 10^{-4}$ erg cm^{-2}, implies a huge isotropic equivalent energy released in the source frame, $E_{\mathrm{iso}} = (2.1 \pm 0.1) \times 10^{54}$ erg. By using the NeuCosmA code, which simulates collisions at different radii in a GRB jet considering an evolving system of plasma shells with a distribution of Lorentz factors, masses and widths, a synthetic GRB light curve reproducing that of GRB 110918A has been constructed. After choosing several input parameters, radius and Lorentz factor distributions, 500 simulations have been performed and the averaged light curve has been com-

puted ($\chi^2/\nu \simeq 819$). The variability time $t_{\rm v} = 0.220 \pm 0.008$, the burst duration $T_{90} = 17.136 \pm 0.003$ and the collisions number $N_{\rm coll} = 78 \pm 3$ for the averaged simulated light curve are consistent with the known quantities for the GRB 110918A: $t_{\rm v} = 0.25$, $T_{90} = 19.6 \pm 0.1$ and $N_{\rm coll} \simeq 79$. Through these simulations, the number of observed pulses (which has been shown to be 5) is much smaller than the number of ejected shells (110), hence the inner engine results more variable than the observed light curve. The influence of input parameters on the synthetic light curves has also been investigated. These results could provide help to adjust the input parameters in the NeuCosmA code. They also help understanding how the characteristic parameters of GRBs influence the light curves that are observed and, therefore, how the central engine of these astrophysical objects could work.

Furthermore, an innovative and recent method to study GRB light curves in terms of timing studies, which are considered powerful tools to understand the emission mechanism regulating the prompt emission of the GRB and its variability (given the lack of direct observations of the inner engine), has been investigated: the Hilbert-Huang transformation (HHT). Such method works in temporal space directly rather than in the corresponding frequency space and consists in the signal decomposition within the individual modes embedded in the data (Empirical Mode Decomposition, EMD) and in a following spectral analysis that allows to construct the energy-frequency-time distribution for each recognized mode in the data (Hilbert spectral analysis, HSA). The stability of this method has been investigated: while translation and addition of a constant factor do not influence results, the addition of random fluctuations produces relevant modification to the EMD. The major instabilities appear in correspondence of the dominant peak in the light curve. One can therefore suppose that the EMD can only be applied to signals where the peak heights are not that different as in GRB 110918A. For these reasons, it was not possible to draw conclusions on the central engine behavior of GRB 110918A by comparing the results of HHT obtained on the simulated and observed light curve.

The neutrino, gamma-ray and UHECR production in GRB 110918A is also investigated, through the simulation results of NeuCosmA. The shape of the neutrino light curve shows a smooth trend, which averages out the variability present in the corresponding gamma-ray one. Neutrinos are, in fact, produced mainly in the initial collision, within the first ~ 3 s of duration of the GRB. Therefore, neutrinos appear to predominantly come mainly from regions close to the center, while UHECR protons come mainly from intermediate regions. Finally, in this work the first multi-collision neutrino flux estimate for a real GRB is presented. Assuming the flux evaluated through the simulation reproducing the GRB light curve and taking into account the data taking conditions and the detector response during the GRB episode, the number of expected signal in the ANTARES neutrino telescope from GRB 110918A was calculated: $\mu_s = 6.1 \times 10^{-4}$. This value is smaller than the one previously calculated by the ANTARES Collaboration according to the one-zone approach ($\mu_s = 1.3 \times 10^{-2}$). This is connected with the fact that the novel modeling accounts for the whole inner engine behavior, as dictated by the emitted light curve, while the past calculations simplified such a description within a unique collision. The limited expected event rate justifies the lack of spatial and temporal coincidence

between neutrinos and GRB events until now. Further investigations will be possible with the incoming generation of neutrino detectors, such as KM3NeT-ARCA and IceCube-GEN2. In absence of an emerging signal in the coming years, limits from the current and future neutrino detectors will increasingly constrain the contribution of GRBs to the observed flux of UHECRs.

Appendix A

Non-linearity and non-stationarity study GRB 110918A

A.1   Additional figures

Additional plots about the study of the non-linearity and non-stationarity study of the GRB 110918A are shown. In each of the following plots in the upper left corner the GRB 110918A light curve is shown, in the upper right corner the considered interval of light curve and below the PDF evolution as a function of counts detected by Konus-WIND. The considered time segment is shown in the upper right plot and is indicated by different colors. The interval $\Delta x = [x, x + dx]$, which corresponds to a certain number of bins within count values (x-axis), is also reported in the plot below. The solid line, where present, shows the result of the Gaussian fit. If no line is plotted, the PDF evolution is not fittable with a Gaussian fit, so the data represent physical non-linear process. The way on which this study is done is described in Section 4.2.1.
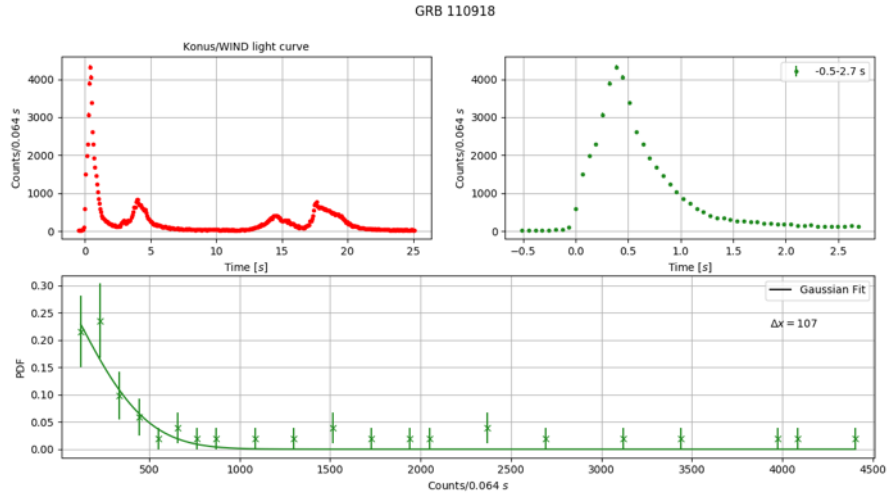
Figure A.1. $\Delta x = 107 \text{ s}^{-1}$, $N_{\text{bins}} = 40$.
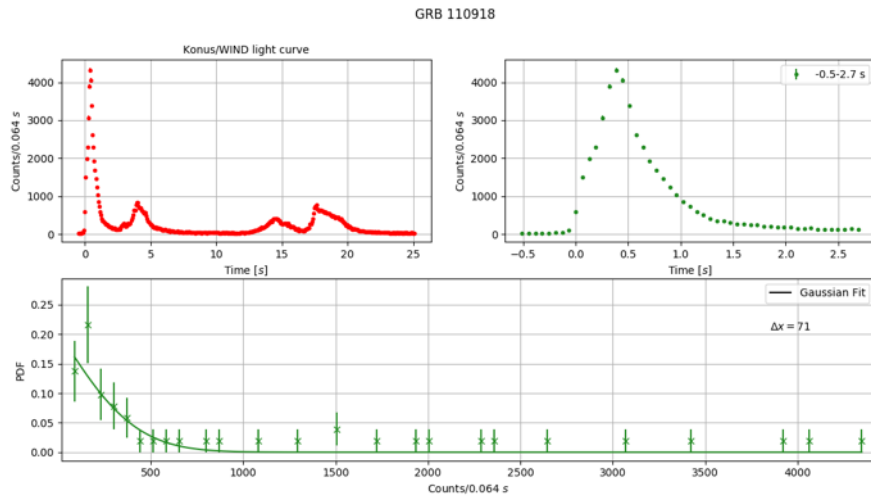
Figure A.2. $\Delta x = 61 \text{ s}^{-1}$, $N_{\text{bins}} = 60$.
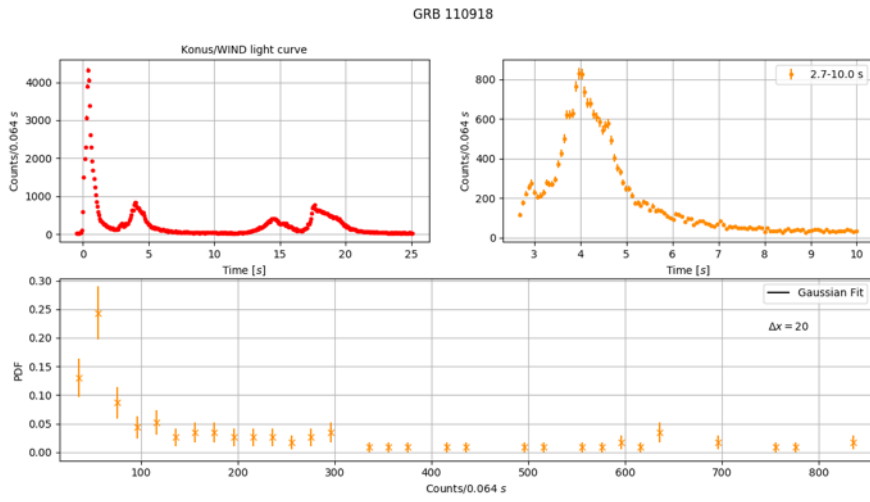
Figure A.3. $\Delta x = 20 \text{ s}^{-1}$, $N_{\text{bins}} = 40$.
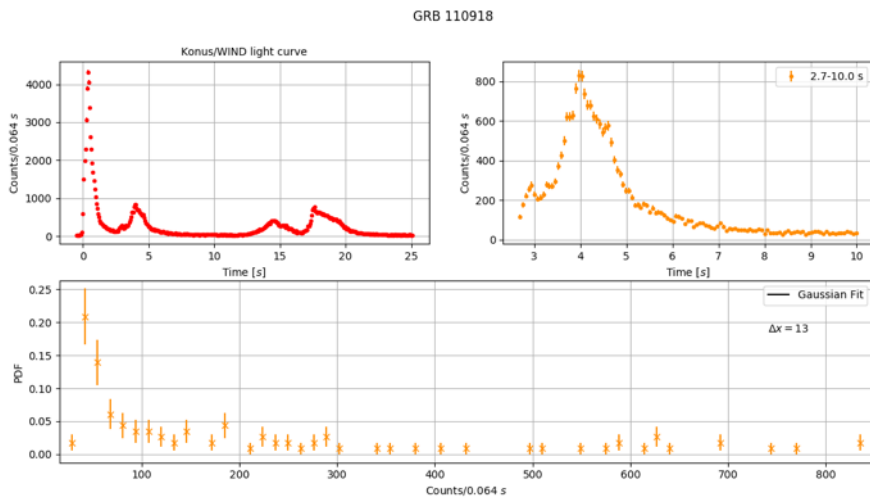
Figure A.4. $\Delta x = 13 \text{ s}^{-1}$, $N_{\text{bins}} = 60$.
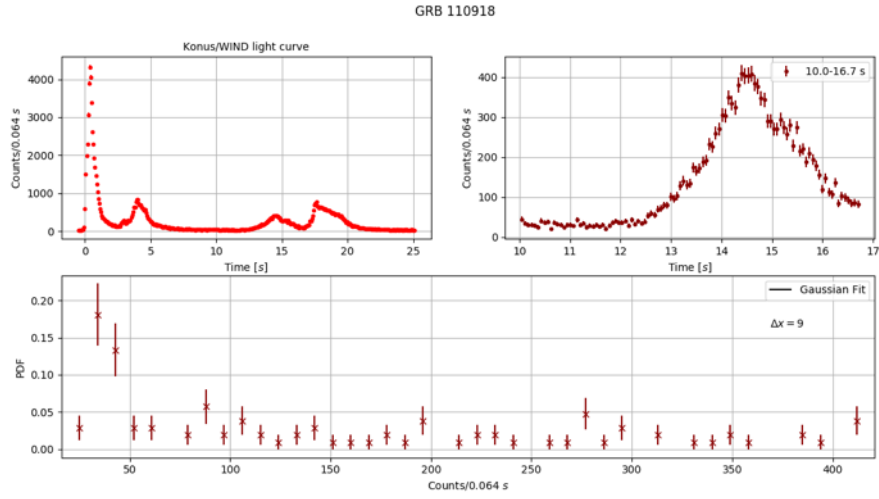
Figure A.5. $\Delta x = 9 \text{ s}^{-1}$, $N_{\text{bins}} = 40$.
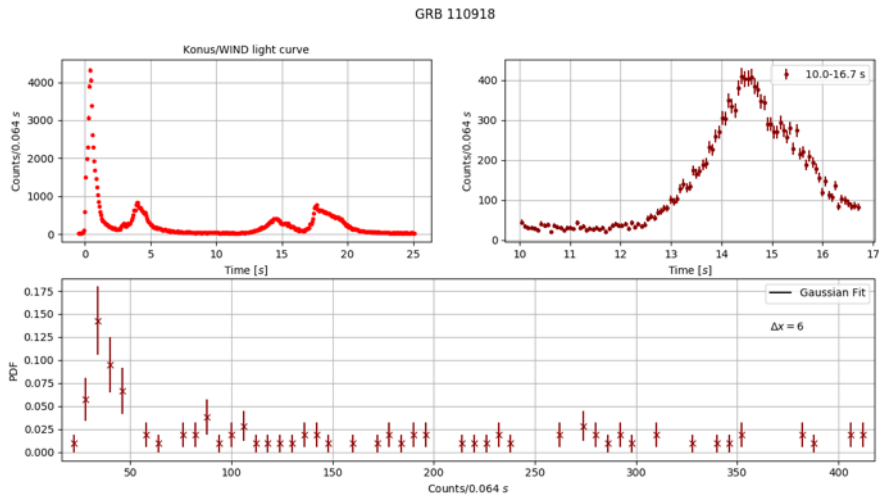
Figure A.6. $\Delta x = 6 \text{ s}^{-1}$, $N_{\text{bins}} = 60$.
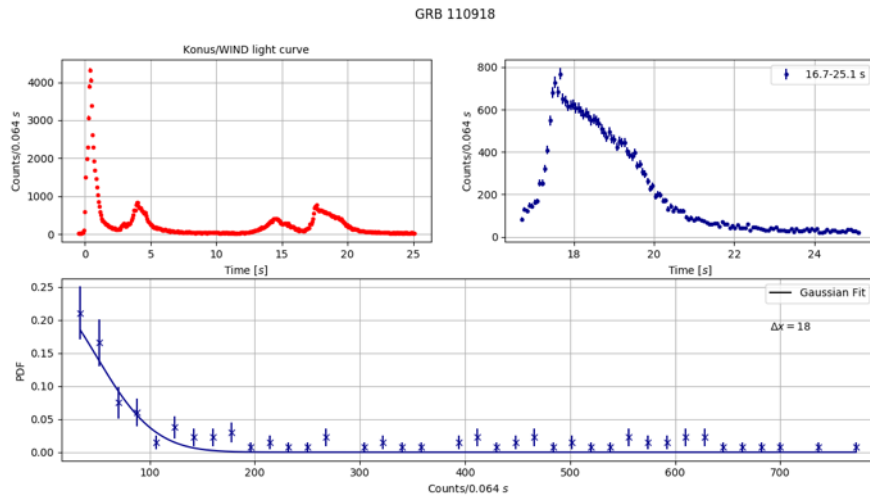
Figure A.7. $\Delta x = 18 \text{ s}^{-1}$, $N_{\text{bins}} = 40$.
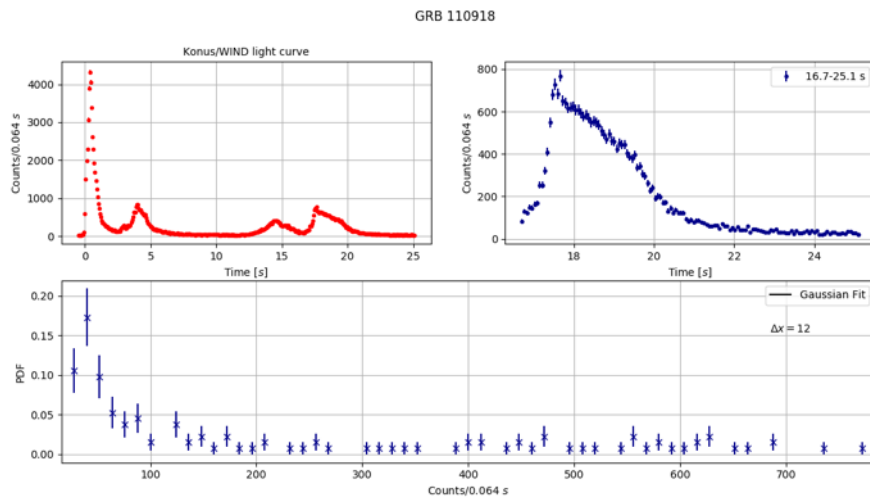
Figure A.8. $\Delta x = 12 \text{ s}^{-1}$, $N_{\text{bins}} = 60$.

Appendix B

Li & Fenimore peak finding algorithm (PFA)

Li & Fenimore [93] proposed the following simple algorithm to analyze the gamma-ray burst temporal structures:

1. Fit the burst background using a linear function $B(t)$ to the pre- and postburst regions;

2. During the burst, every count bin that has more counts than the neighboring bins in both sides is a candidate peak with count C_p at time t_p;

3. Search on both sides of each candidate peak for counts C_1, at t_1, and C_2, at t_2, so that the conditions $C_p - C_{1,2} \geq N_{\mathrm{var}} \sqrt{C_p}$ are satisfied, where N_{var} is the threshold criterion for identifying the peaks ($3 \leq N_{\mathrm{var}} \leq 5$);

4. The search will stop either when both C_1 and C_2 are found, in which case C_p becomes a *true peak*, or when counts higher than C_p (on either side of t_p) are encountered, in which case C_p is not a true peak and is discarded. At this point N_k peaks should have been identified.

5. Locate the minima between two successive peaks as *valleys*.

Application of PFA algorithm to GRB 110918A
The PFA algorithm has been applied on GRB 110918A algorithm writing a new Python code, which simulates the steps just explained, to study distributions of its pulses width δt and intervals between pulses Δt.
The background has been estimated including all Konus-WIND data (from $T_0 - 0.512$ s to $T_0 + 98.752$s) for a precise measurement and gives the following result (shown in Figure B.1):
$$B(t) = (-0.092 \pm 0.007)x + (27.93 \pm 0.44). \tag{B.1}$$

The intercept is very small, so it can be considered a constant background of ~ 28 counts/s.
After that, candidate peaks have been estimated and true peaks selected with the choice of $N_{\mathrm{var}} = 3$. Five true peaks C_p at times t_p have been found (Table B.1). The

minima between two successive C_p have been considered as valleys, similar to what was proposed by Li & Fenimore (see Figure B.2).
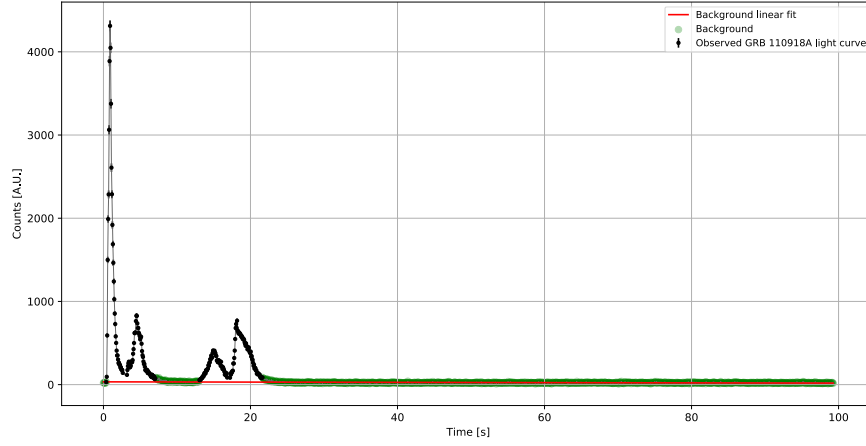
Figure B.1. Background estimation on GRB 110918A. The background (green points) is highlighted on the observed GRB 110918A light curve (black points). The red solid line indicates the background linear fit.
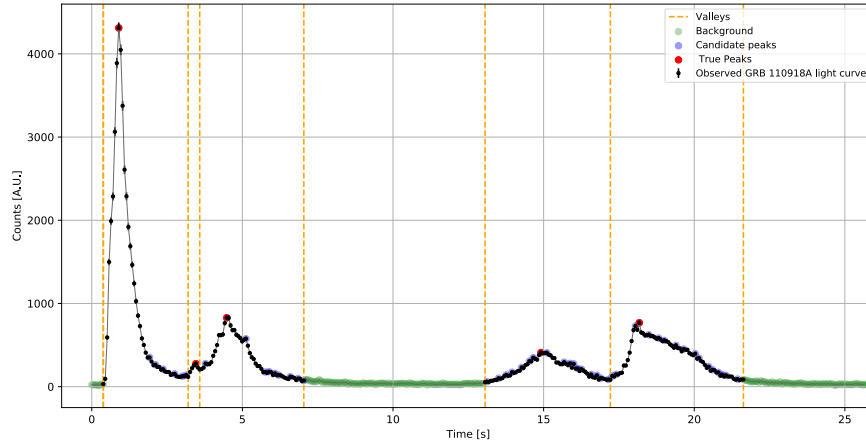
Figure B.2. Identification of valleys and true peaks on GRB 110918A light curve. The background (green points) is highlighted on the observed GRB 110918A light curve (black points). Blue points indicate candidate peaks, and red points the true ones. Dashed vertical lines (in orange) indicate the so-called valleys.

C_p (counts/s)	t_p (s)
4312 ± 65	0.896
276 ± 17	3.456
828 ± 29	4.480
410 ± 20	14.912
768 ± 28	18.176

Table B.1. True peaks of GRB 110918A light curve founded with the PFA algorithm.

Calculation of observed pulses timings and widths

After the true peaks and valleys identification for GRB 110918A light curve, pulses width δt and temporal difference between two close peaks Δt values have been found:

- δt has been estimated through a Gaussian fit of each identified peak (light curve zone with C_p and between two successive valleys) as *Full Width at Half Maximum* (FWHM)[1]. Thus, the following normal distribution has been considered

$$f(x) = Ae^{-\frac{(x-\mu)^2}{2\sigma^2}}, \tag{B.2}$$

  where A is the amplitude, μ is the mean of the distribution, and σ is the standard deviation. From Equation B.2 it is possible to calculate:

$$\delta t = \text{FWHM} = 2\sigma\sqrt{2\ln 2}. \tag{B.3}$$

- Δt is the difference between the temporal values t_p of two close C_p.

The results of Gaussian fits are shown in Figure B.3 and their best value parameters are in Table 4.3. δt and Δt values, from which it has been possible to analyze their distribution and establish how to do the GRB light curve simulation with the NeuCosmA code (see Chapter 4), are in Table 4.7.

---

[1]Parameter given by the distance between points on a curve at which the function reaches half of its maximum value.
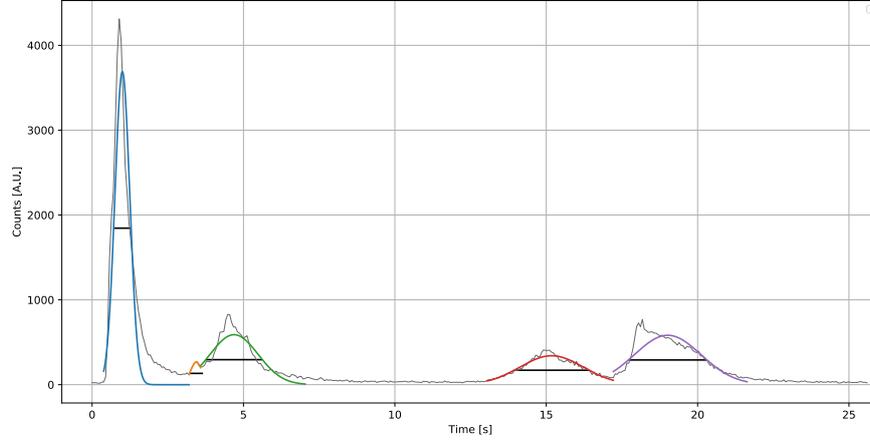
Figure B.3. Gaussian fits on GRB 110918A peaks. The observed light curve is in black, Gaussian fits are indicated with the colored solid line, and the horizontals black lines are the FWHM obtained from Equation B.3.

	A (counts/s)	μ (s)	σ (s)
First peak	3050 ± 257	0.985 ± 0.026	0.347 ± 0.026
Second peak	266 ± 5	3.440 ± 0.006	0.189 ± 0.008
Third peak	558 ± 34	4.686 ± 0.050	0.858 ± 0.050
Fourth peak	341 ± 7	15.178 ± 0.019	1.049 ± 0.019
Fifth peak	583 ± 22	19.012 ± 0.037	1.103 ± 0.035

Table B.2. Best value parameters from Gaussian fits applied on GRB 110918A peaks.

Appendix C

Light curve characterization plot results

C.1 Additional figures

In this Appendix additional plots obtained by a systematic study done on parameters variation (by changing one input value in the NeuCosmA code), beyond those already present in Section 4.3.2, is presented. In these plots, the best fit curve for the data, accounting for their errors too, is indicated by a solid line.

Initial number of shells variation
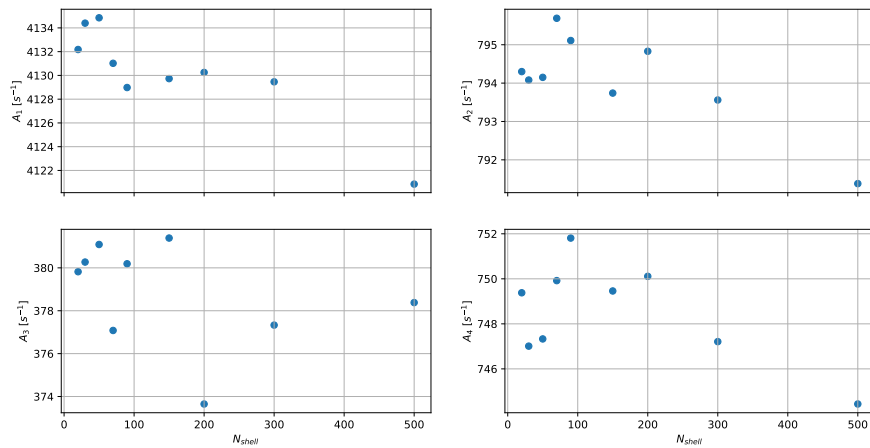
Figure C.1. Height of peaks A_k, with $1 \leq k \leq 4$, as a function of the initial number of shells N_{shell}. These plots are considered without errors to appreciate much better differences between values.
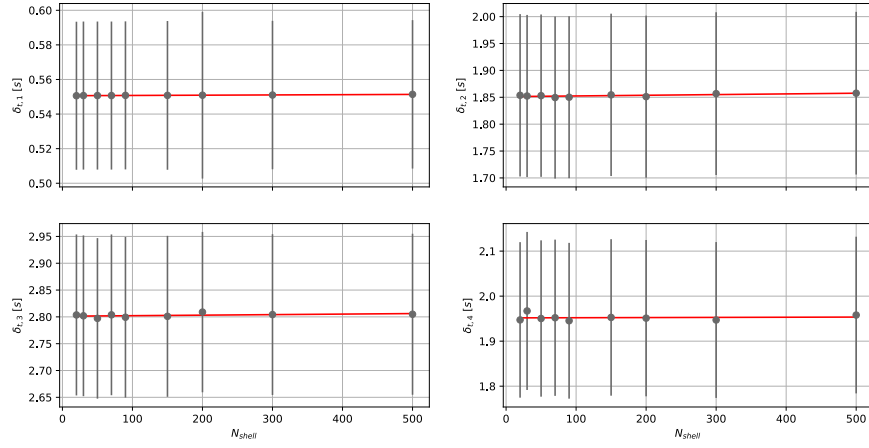
Figure C.2. Pulses width δt_k, with $1 \leq k \leq 4$, as a function of the initial number of shells, N_{shell}.
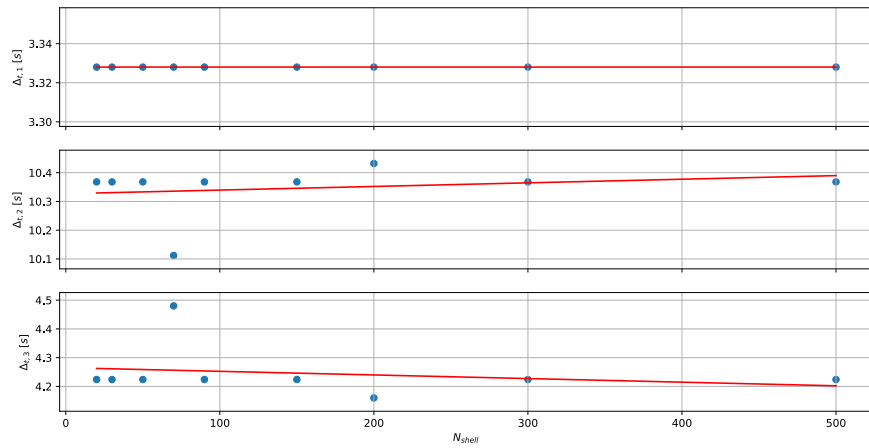
Figure C.3. Intervals between pulses Δt_k, with $1 \leq k \leq 3$, as a function of the initial number of shells, N_{shell}.

Initial shells Lorentz factor variation
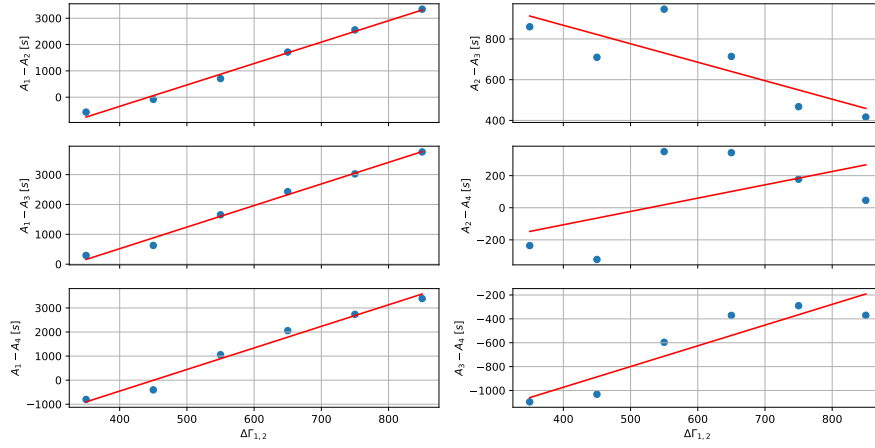
Figure C.4. Difference between height of peaks as a function of the Lorentz factor difference between the first two shells, $\Delta\Gamma_{1,2} = \Gamma_{0,1} - \Gamma_{0,2}$.

Bibliography

[1] A. Aab, et al., JCAP, 1704(04), 38, 2017

[2] A. Aab, et al., Science 357, 1266, 2017

[3] M. G. Aartsen, et al., (IceCube Collaboration), Science, 342, 947, 2013

[4] M.G. Aartsen, et al., (IceCube-Gen2 Collaboration), [arXiv:1412.5106v2 [astro-ph.HE]], 2014

[5] M. G. Aartsen, et al., Astrophys.J. 826 no.2, 220, 2016

[6] M. G. Aartsen, et al., (IceCube Collaboration), [arXiv:1612.05093v2 [astro-ph.IM]], 2017

[7] M. G. Aartsen, et al., (IceCube Collaboration), [arXiv:1702.06868v2 [astro-ph.HE]], 2017

[8] M. G. Aartsen, et al., (IceCube Collaboration), https://10.1126/science.aat2890, 2018

[9] M. G. Aartsen, et al., [arXiv:1807.11492 [astro-ph.HE]], 2018

[10] R. Abbasi, et al., ApJ, 710, 346, 2010

[11] B. P. Abbot, et al., ApJ, 848, L12, 2017

[12] A. A. Abdo, et al., ApJ, 698, 2121, 2009

[13] K. Abe, et al., ApJ, 652, 198, 2006

[14] J. Abraham, et al. (Pierre Auger Collaboration), Astropart. Phys. 29, 188, 2008, [arXiv:0712.2843v2 [astro-ph]], [Erratum ibid. 30, 45, 2008]

[15] S. Adrián-Martínez, et al.., (ANTARES Collaboration), [arXiv:1202.3894 [astro-ph.IM]], 2012

[16] S. Adrián-Martínez, et al., ApJ, 760, 53, 2012

[17] S. Adrián-Martínez, et al. (KM3NeT Collaboration), J. Phys. G: Nucl. Part. Phys., 43, 084001, 2016

[18] M. Ageron, et al., (ANTARES Collaboration), Nucl. Instrum. Meth, A 656, 11, 2011

[19] J. A. Aguilar, et al., (ANTARES Collaboration), Nucl. Instrum. Meth, A 570, 107, 2007

[20] A. Albert, et al., MNRAS, 469, 906, 2017

[21] M. Ambrosio, et al., ApJ 545, 1038, 2001

[22] M. Amenomori, et al., (Tibet AS-gamma Collaboration), ApJ, 836, 153, 2017

[23] C. Amsler, et al., (Particle Data Group), Physics Letters B667, 1, 2008

[24] K. Asano $ S. Terasawa, ApJ, 705, 1714, 2009

[25] W. B. Atwood, et al., (Fermi-LAT Collaboration), ApJ, 697, 1071, 2009

[26] P. Auger, R. Maze & T. Grivet-Meyer, C. R. Acad. Sci. 206, 1721, 1938

[27] P. Baerwald, et al., Nat. Commun., 6, 6783, 2015

[28] P. Baerwald, M. Bustamante & W. Winter, ApJ, 768,186, 2013

[29] D. Band, et al., ApJ, 413, 281, 1993

[30] A. R. Bell, MNRAS, 182, 147, 1978

[31] A. M. Beloborodov, ApJ, 539, L25, 2000

[32] A. M. Beloborodov & P. Mészáros, [arXiv:1701.04523 [astro-ph.HE]], 2017

[33] V. S. Berezinskii, S. I. Grigor'eva, & V. A. Dogiel, Astron. Astrophys., 232, 582, 1990

[34] D. R. Bergman, et al., (HiRes Collaboration), [arXiv: 0807.2814 [astro-ph]], 2008

[35] J. Beringer, et al., (Particle Data Group), and 2013 update for the 2014 edition (http://pdg.lbl.gov), Phys. Rev. D86.010001, 2012

[36] N. Bhatt & S. Bhattacharyya, MNRAS, 420, 1706, 2012

[37] S. Bhattacharyya, Timing studies of gamma-ray burst prompt emission, *APP-COS Advances in Astroparticle Physics and Cosmology, Kolkata (India)*, 2018

[38] J. D. Bjorken, Phys. Rev., 179, 1547, 1969

[39] P. Blasi, Comptes Rendus Physique, 15, 329, 2014

[40] J. Blümer, R. Engel, & J. R. Hörandel, Progress in Particle and Nuclear Physics, 63, 293, 2009

[41] M. S. Briggs, et al., ApJ, 524, 82, 1999

[42] N. Busca, D. Hooper, & E. W. Kolb, Phys. Rev. D 73, 2006

[43] M. Bustamante, et al., Astrophys. J., 837, 33, 2017

[44] M. Cardillo, et al., Astron. Astrophys., 565, A74, 2014

[45] Q. Chen, et al., Adv. Compt. Math., 24, 271, 2006

[46] P. A. Cherenkov, Phys. Rev. 52, 378, 1937

[47] T. Chiarusi & M. Spurio, Eur.Phys.J., C65, 649, 2010

[48] E. Costa, et al., Nature, 387, 783, 1997

[49] A. Cucchiara, et al., ApJ, 736, 7, 2011

[50] A. de Ugarte Postigo, et al., GCN, 12375, 1, 2011

[51] A. D. Erlykin, M. Lipski & A. W. Wolfendale, Astropart. Phys. 8, 283, 1998

[52] E. Fermi, Phys. Rev. 75, 1169, 1949

[53] R. P. Feynman, Phys. Rev. Lett., 23, 1425, 1969

[54] K.A Firoz, D. V. Phani Kumar & K. S. Cho, Astrophys Space Sci 325, 185, 2010

[55] G. J. Fishman, et al., NASA Goddard Space Flight Center 19th Intern. Cosmic Ray Conf., 3, 343, 1985

[56] S. Fotopoulou, PhD thesis, 2012

[57] D. D. Frederiks, et al., ApJ, 779, 151, 2013

[58] T. K. Gaisser, *Cosmic Rays and Particle Physics*, Cambridge University Press, Cambridge, 1990

[59] T. K. Gaisser, F. Halzen, & T. Stanev, [arXiv:hep-ph/9410384v1], 1994

[60] R. Gandhi, et al., Astrop. Phys., 5, 81, 1996

[61] N. Gehrels, et al., ApJ, 611, 1005, 2004

[62] N. Gehrels, et al., Nature, 437, 851, 2005

[63] G. Ghisellini, [arXiv:0111584v1 [astro-ph]], 2001

[64] G. Giacomelli, Journal of Communication and Computers, 2012

[65] M. M. González, et al., Nature, 424, 749, 2003

[66] J. Goodman, ApJ, 308, L47, 1986

[67] J. Goodman, ApJ, 363, L47, 1990

[68] K. Greisen, Phys. Rev. Lett., 16, 748, 1966

[69] D. Guetta, et al., Astropart. Phys., 20, 429, 2004

[70] J. E. Gunn & J. P. Ostriker, Phys. Rev. Lett. 22, 728 -731, 1969

[71] F. Halzen & S. R. Klein, Review of Scientific Instruments, 81, 081101, 2010

[72] D. Harari, S. Mollerach, & E. Roulet, Phys. Rev., D89(12), 123001, 2014

[73] D. Harari, S. Mollerach, & E. Roulet, Phys. Rev., D92(06), 063014, 2015

[74] V. F. Hess., Phys. Z., 13, 1084, 1912

[75] R. C. Hickox & D. M. Alexander, Annu. Rev. Astron. Astrophys., 56, 1, https://doi.org/10.1146/, 2018

[76] N. E. Huang, et al., Proc. R. Soc. Lond. A, 454, 903, 1998

[77] S. Hümmer, et al., ApJ, 721, 630, 2010

[78] K. Ioka, Prog. Theor. Phys., 124, 667, 2010

[79] M. Kachelriess, [arXiv:0801.4376v1 [astro-ph]], 2008

[80] R. W. Klebesadel, I. B. Strong & I. B. Olson, ApJ 182, L85, 1973

[81] K. Kobayakawa, Y. Sato & T. Samura, Phys. Rev. D 66, 083004, 2002

[82] W. Kolhörster - quoted in "Cosmic Rays" by J.G. Wilson, The Wykeham Science Series, London, 1976

[83] K. Kotera & A. V. Olinto, Ann. Rev. Astron. Astrophys., 49, 119, 2011

[84] C. Kouveliotou, et al., ApJ, 413, L101, 1993

[85] H. A. Krimm, V. Mangano & M. H. Siegel, GCN Report, 350, 1, 2011

[86] S. R. Kulkarni, et al., Nature, 398, 389, 1999

[87] P. Kumar & B. Zhang, [arXiv:1410.0679v1 [astro-ph.HE]], 2004

[88] V. A. Kuzmin & G. T. Zatsepin, JETP Lett. 4, 78, 1966

[89] A. L'Abbate, A. Montaruli & I. Sokalski, Astropart. Phys., 23, 57, 2005

[90] P. O. Lagage & C. J. Cesarsky, Astron. Astrophys., 125, 249, 1983

[91] H. Lai, et al., (CTEQ Collaboration), Phys. Rev., D51, 4763, 1995

[92] A. Levan, et al., [arXiv:1611.03091v1 [astro-ph.HE]], 2016

[93] H. Li & E. Fenimore, ApJ, 469, L155, 1996

[94] M. S. Longair, *High Energy Astrophysics*, III edition, 2011

[95] C. A. Meegan, et al., ApJ, 702, 791, 2009 and [arXiv:0908.0450 [astro-ph.IM]]

[96] M. R. Metzger, et al., Nature, 387, 878, 1997

[97] K. Mannheim, et al., Phys. Rev., D, 63, 023003, 2001

[98] M. A. Markov, Proceedings Int. Conf. on High Energy Physics, 183, Univ. of Rochester, 1960

[99] C. A. Meegan, et al., Nature, 355, 143, 1992

[100] E. Nakar & T. Piran, MNRAS, 331, 40, 2002

[101] W. S. Paciesas, et al., ApJ, 199, 18, 2012

[102] B. Paczyński, ApJ, 308, L43, 1986

[103] T. Piran, Physics Reports, 314, 575, 1999

[104] T. Piran, Physics Reports, 333, 529, 2000

[105] T. Piran & E. Nakar, [arXiv:0202403v2 [astro-ph]], 2002

[106] V. S. Ptuskin, et al., Aston. Astroph., 321, 434, 1997

[107] M. J. Rees & P. Mészáros, ApJ, 430, L93, 1994

[108] G. Rilling, P. Flandrin & P. Goncalves, On empirical mode decomposition and its algorithms, *IEEE-EURASIP Workshop on Nonlinear Signal and Image Processing NSIP-03, Grado (Italy)*, 2003

[109] G. I. Rubtsov, et al., Phys. Rev., D73, 2006

[110] F. Ryde, et al., ApJ, 652, 1400, 2006

[111] R. Sari & T. Piran, ApJ, 485, 270, 1997

[112] A. Shemi & T. Piran, ApJ, 365, L55, 1990

[113] K. Shinozaki, et al., (AGASA Collaboration), Nucl. Phys. Proc. Suppl., 151, 2006

[114] C. Shuwang, (ARGO-YBJ Collaboration), Proceedings of the 32nd International Cosmic Ray Conference (ICRC), 2011

[115] T. Stroman & Y. Tameda, PoS, ICRC, 2015:361, 2016

[116] M. Takeda, et al., Phys. Rev. Lett., 81, 1163, 1998

[117] M. Tavani, et al., (AGILE Collaboration) Astrophys. J., 710, L151, 2010

[118] K. Toma, X.F. Wu, & P. Mészáros, [arXiv:1002.2634 [astro-ph.HE]], 2010

[119] P. Trávníček, PhD thesis, 2004

[120] A. Tsvetkova, et al., ApJ, 850, 161, 2017, [arXiv:1710.08746v2 [astro-ph.HE]]

[121] E. Waxman & J. Bahcall, Phys. Rev. Lett., 78, 2292, 1997

[122] H. G. S. Wilkens, PhD thesis, 2003

[123] Q. Wu & S. D. Riemenschneider, Advances in Adaptive Data Analysis. Vol. 2, No. 2, 157, 2010

[124] W-M Yao, et al., (Particle Data Group), J. Phys., G 33, 1, 2006

[125] B. Zhang & H. Yan, ApJ 726, 90, 2011

[126] B. Zhang & P. Kumar, Phys. Rev. Lett., 110, 121101, 2013

[127] B. Zhang & P. Kumar, Pyhs. Rep., 561, 1, 2015

[128] B.-B. Zhang, et al., ApJ 730, 141, 2011

Acknowledgements